CONSTRUCTION OF Z-SCHEME Bi_2WO_6/SnS_2 HETEROJUNCTION PHOTOCATALYST FOR SIMULTANEOUS RHODAMINE B DEGRADATION AND Cr(VI) REDUCTION UNDER SUNLIGHT IRRADIATION

LIAW SI JIAN

UNIVERSITI TUNKU ABDUL RAHMAN

CONSTRUCTION OF Z-SCHEME Bi_2WO_6/SnS_2 HETEROJUNCTION PHOTOCATALYST FOR SIMULTANEOUS RHODAMINE B DEGRADATION AND Cr(VI) REDUCTION UNDER SUNLIGHT IRRADIATION

LIAW SI JIAN

A project report submitted in partial fulfilment of the requirements for the award of Bachelor of Engineering (Hons) Petrochemical Engineering

Faculty of Engineering and Green Technology
Universiti Tunku Abdul Rahman

May 2023

DECLARATION

I hereby declare that this project report is based on my original work except for citations and quotations which have been duly acknowledged. I also declare that it has not been previously and concurrently submitted for any other degree or award at UTAR or other institutions.

Signature :

Name : LIAW SI JIAN

ID No. : 18AGB02567

Date : 29 April 2023

APPROVAL FOR SUBMISSION

I certify that this project report entitled **"CONSTRUCTION OF Z-SCHEME Bi_2WO_6/SnS_2 HETEROJUNCTION PHOTOCATALYST FOR SIMULTANEOUS RHODAMINE B DEGRADATION AND Cr(VI) REDUCTION UNDER SUNLIGHT IRRADIATION"** was prepared by **LIAW SI JIAN** has met the required standard for submission in partial fulfilment of the requirements for the award of Bachelor of Engineering (Hons) Petrochemical Engineering at Universiti Tunku Abdul Rahman.

Approved by,

Signature :

Supervisor : Assoc. Prof. ChM. Ts. Dr. Sin Jin Chung

Date : 29 April 2023

Signature :

Supervisor : Assoc. Prof. ChM. Ts. Dr. Lam Sze Mun

Date : 29 April 2023

The copyright of this report belongs to the author under the terms of the copyright Act 1987 as qualified by Intellectual Property Policy of Universiti Tunku Abdul Rahman. Due acknowledgement shall always be made of the use of any material contained in, or derived from, this report.

© 2023, Liaw Si Jian. All right reserved.

Specially dedicated to

my beloved parents, supervisor, lecturers, seniors and friends.

ACKNOWLEDGEMENTS

I would like to express my gratitude to everyone who helped make this endeavour a success. First and foremost, I would like to express my sincere gratitude to my research supervisor, Assoc. Prof. ChM. Ts. Dr. Sin Jin Chung, for his important advice, professionalism, guidance, and immense patience throughout the project's growth. My greatest gratitude also goes to my co-supervisor, Assoc. Prof. ChM. Ts. Dr. Lam Sze Mun, as well as my moderator, Ir. Ts. Dr. Toh Pey Yi, for their insightful feedbacks.

In addition, I wish to thank all of the helpful and pleasant laboratory officers, particularly Ms. Lim Cheng Yen, Mrs. Ropidah Hamimi binti Mohd Zain and Mr. Yong Tzyy Jeng, for their outstanding support in giving technical assistance during the completion of Final Year Project.

Furthermore, yet importantly, I would like to express my gratitude to my irreplaceable and beloved family members for their unwavering support throughout my university life. Last but not least, my heartfelt appreciation goes to my friends and seniors, Chin Ying Hui and Tan Jing Han, for their help and encouragement during this project.

CONSTRUCTION OF Z-SCHEME Bi_2WO_6/SnS_2 HETEROJUNCTION PHOTOCATALYST FOR SIMULTANEOUS RHODAMINE B DEGRADATION AND Cr(VI) REDUCTION UNDER SUNLIGHT IRRADIATION

ABSTRACT

Industrial sewage often contain metal ions and dyes, which are difficult to be removed efficiently. Solar-light-driven heterogeneous semiconductor photocatalysis is recognized as a potential and efficacious approach for environmental remediation. Specifically, the heterojunction photocatalysts with low band-gaps and recombination rates are highly-valuable for this purpose. In this study, a novel Bi_2WO_6/SnS_2 binary composite material was created via a hydrothermal-deposition method. Different analytical techniques were employed to investigate the photocatalyst's physiochemical and optical properties. It discovered that the composite material had an extended visible light photosensitivity as a result of the reduced band gap of Bi_2WO_6/SnS_2. The photocatalytic performance of Bi_2WO_6/SnS_2 was assessed by using it to degrade RhB and reduce Cr(VI) under sunlight exposure for 180 minutes. Kinetic studies showed that Bi_2WO_6/SnS_2-10 (10 wt% of SnS_2) manifested the best performance, in which 95.5 % RhB (k_{app} = 0.0178 min^{-1}) and 100 % Cr(VI) (k_{app} = 0.0513 min^{-1}) removal efficiencies were achieved separately. Simultaneous removal of both pollutants further explored the ability of Bi_2WO_6/SnS_2-10 to achieve the removal efficiency of 83.19 % for RhB (k_{app} = 0.0082 min^{-1}) and 94.60 % for Cr(VI) (k_{app} = 0.0159 min^{-1}). The phytotoxicity study also revealed that the toxicity of RhB-Cr(VI) mixed solution treated by Bi_2WO_6/SnS_2-10 photocatalyst has been substantially reduced. This present work indicates the potential of Bi_2WO_6/SnS_2 for use in photodegradation of organic pollutants and photoreduction of heavy metals.

TABLE OF CONTENTS

DECLARATION **ii**
APPROVAL FOR SUBMISSION **iii**
ACKNOWLEDGEMENTS **vi**
ABSTRACT **vii**
TABLE OF CONTENTS **viii**
LIST OF TABLES **xi**
LIST OF FIGURES **xii**
LIST OF SYMBOLS / ABBREVIATIONS **xv**

CHAPTER

1 INTRODUCTION **1**
1.1 Background of Study 1
1.2 Problem Statement 5
1.3 Objectives 8
1.4 Scope of Study 8

2 LITERATURE REVIEW **9**
2.1 Water Pollution 9
2.2 Review on Dye and Heavy Metals in Wastewater 11
2.3 Usage and Hazardous Effects of Rhodamine B and Chromium 17
2.4 Heterogeneous Photocatalysis 21
2.5 Bi_2WO_6 as Photocatalyst 23
2.6 Mechanism of Bi_2WO_6 Photocatalysis 29

	2.7	Modification of Bi_2WO_6	32
	2.8	Synthesis of Bi_2WO_6–based Composites via Deposition Method	38
	2.9	Phytotoxicity	40
	2.10	Summary of Literature Review	43
3	**METHODOLOGY**		**44**
	3.1	Overall Experimental Flowchart	44
	3.2	Materials and Chemicals	45
	3.3	Preparation of Photocatalyst	47
	3.4	Characterization	49
		3.4.1 X-ray Diffraction (XRD)	49
		3.4.2 Field Emission Scanning Electron Microscopy (FESEM)	49
		3.4.3 Attenuated Total Reflectance - Fourier Transform Infrared Spectroscopy (ATR-FTIR)	50
		3.4.4 Ultraviolet-visible Diffuse Reflectance Spectroscopy (UV-vis DRS)	50
		3.4.5 Transient Photocurrent Response (TPR), Electrochemical Impedance Spectroscopy (EIS) and Mott-Schottky (M-S)	50
	3.5	Photoactivity Test	51
	3.6	Phytotoxicity Test	53
	3.7	Radical Scavenging Experiment	54
4	**RESULTS AND DISCUSSION**		**55**
	4.1	Characterization	55
		4.1.1 Field Emission Scanning Electron Microscopy (FESEM)	55
		4.1.2 X-ray Diffraction (XRD)	58

	4.1.3	Attenuated Total Reflectance – Fourier Transform Infrared Spectroscopy (ATR-FTIR)	61
	4.1.4	Ultraviolet-visible Diffuse Reflectance Spectroscopy (UV-vis DRS)	63
	4.1.5	Transient Photocurrent Response (TPR), Electrochemical Impedance Spectroscopy (EIS) and Mott-Schottky (M-S)	67
4.2		Solar Light Irradiation Photocatalytic Activities	69
	4.2.1	Photodegradation of Rhodamine B (RhB)	69
	4.2.2	Photoreduction of Cr(VI)	74
	4.2.3	Simultaneously removing of RhB and Cr(VI)	78
4.3		Phytotoxicity Evaluation	83
4.4		Radical Scavenging Experiment	85
5		**CONCLUSION AND RECOMMENDATIONS**	**88**
5.1		Conclusion	88
5.2		Recommendation	89
REFERENCES			**90**

LIST OF TABLES

TABLE	TITLE	PAGE
2.1	Common Metals Found in Different Dye Classes	11
2.2	Distribution of Heavy Metal (ppm Dry Weight) in Peninsular Malaysia Coastal Sediment	14
2.3	Acceptable Conditions for Discharge of Industrial Effluent or Mixed Effluent of Standards A and B	16
2.4	General Properties of Rhodamine B	17
2.5	General Properties of Chromium	19
2.6	Band Structures Data of Bi-Based Photocatalysts	24
2.7	Photocatalytic Activity of Bi_2WO_6 on Various Pollutants	28
2.8	Photocatalytic Activity of Bi_2WO_6-Based Heterojunction Photocatalyst on Various Pollutants	37
3.1	List of Material and Chemical Used	45
4.1	Comparison of Synchronous Photocatalytic RhB Degradation and Cr(VI) Reduction Over Other Photocatalysts	80

LIST OF FIGURES

FIGURE	TITLE	PAGE
2.1	Scores and National Water Security Index	10
2.2	Contribution of Textile Industry to Water Pollution for Different States in Malaysia	12
2.3	The Key Aspects Governing the Photochemical Efficiency of a Semiconductor Photocatalyst	22
2.4	The Perovskite-like Composition and Band Structure of Bi_2WO_6	24
2.5	Photodegradation of Organic Pollutant by Bi_2WO_6	31
2.6	Schematic Illustration of (a) Type-II Heterojunction Photocatalyst and (b) Z-Scheme Junction Photocatalyst	33
2.7	Ground State (2H) Structure of SnS_2	34
3.1	Overall Experiment Flowchart	44
3.2	Synthesis of Bi_2WO_6 Particles	47
3.3	Synthesis of SnS_2 Nanoparticles	48
3.4	Synthesis of Bi_2WO_6/SnS_2 Composites	49
3.5	Experimental Setup for Photodegradation of Rhodamine B	51
3.6	Experimental Setup for Photoreduction of Cr(VI)	52
3.7	Experimental Setup for Simultaneous RhB-Cr(VI) Degradation	52

4.1	XRD Patterns of As-prepared Photocatalysts	59
4.2	XRD Peaks Corresponding to the (1 3 1) Lattice Plane of Pure Bi_2WO_6 and Bi_2WO_6/SnS_2 Composites	60
4.3	ATR-FTIR Spectra of As-prepared Photocatalysts	62
4.4	UV-vis Absorbance Spectra of the As-prepared Photocatalysts	65
4.5	UV-vis Reflectance Spectra of the As-prepared Photocatalysts	65
4.6	Kubelka-Munk Plot of the As-prepared Photocatalysts	66
4.7	(a) Transient Photocurrent Response and (b) EIS Measurements of Pristine Bi_2WO_6 and Bi_2WO_6/SnS_2-10; (c-d) M-S Analysis of Pristine Bi_2WO_6 and SnS_2	68
4.8	Degradation Profiles of Rhodamine B Over Various As-prepared Photocatalysts	72
4.9	Absorption Spectra of Rhodamine B Over Bi_2WO_6/SnS_2-10 Binary Composite With the Decolourization Inset	72
4.10	Kinetic Study for the Photodegradation of Rhodamine B	73
4.11	Apparent Reaction Rate Constant, k_{app} of Various Photocatalysts	73
4.12	Degradation Profiles of Cr(VI) Over Various As-prepared Photocatalysts	76
4.13	Absorption Spectra of Cr(VI) Over Bi_2WO_6/SnS_2-10 Binary Composite With the Decolourization Inset	76
4.14	Kinetic Study for the Photoreduction of Cr(VI)	77
4.15	Apparent Reaction Rate Constant, k_{app} of Various Photocatalysts	77

4.16	(a) Degradation Profiles of Rhodamine B in Binary Pollutant Mixture Over Bi_2WO_6 and Bi_2WO_6/SnS_2-10; (b) Absorption Spectra of Rhodamine B Over Bi_2WO_6/SnS_2-10 Binary Composite With the Decolourization Inset; (c) Kinetic Study for the Photodegradation of Rhodamine B; (d) Apparent Reaction Rate Constant, k_{app} of Bi_2WO_6 and Bi_2WO_6/SnS_2-10	81
4.17	(a) Reduction Profiles of Cr(VI) in Binary Pollutant Mixture Over Bi_2WO_6 and Bi_2WO_6/SnS_2-10; (b) Absorption Spectra of Cr(VI) Over Bi_2WO_6/SnS_2-10 Binary Composite With the Decolourization Inset; (c) Kinetic Study for the Photoreduction of Cr(VI); (d) Apparent Reaction Rate Constant, k_{app} of Bi_2WO_6 and Bi_2WO_6/SnS_2-10	82
4.18	(a) Condition of Mung Beans in Each Sample After 7 days; (b-d) Radicle Length of Mung Beans in Distilled Water, Untreated Solution, and Treated Solution Respectively; (e) Phytotoxicity of RhB-Cr(VI) Mixed Pollutant Solution Before and After Degradation Using Bi_2WO_6/SnS_2-10 Composite	84
4.19	Schematic Illustration of Charge Separation Paths and Photocatalytic Mechanism of Z-Scheme Bi_2WO_6/SnS_2 Heterostructure Under Sunlight Irradiation	86
4.20	Radical Scavenging Experiments Over Bi_2WO_6/SnS_2-10 Composite for (a) Rhodamine B Degradation and (b) Cr(VI) Reduction in the Binary Pollutant Mixture	87

LIST OF SYMBOLS / ABBREVIATIONS

α	Absorption coefficient
θ	Diffraction angle, ^{o}
λ	Wavelength, nm
B	Optical-transition-dependent constant
C_o	Concentration of pollutant at time (t = 0), mg/L
C_t or C	Concentration of pollutant at a given time, mg/L
E^o	Redox potential, V
E_{CB}	Conduction band potential, eV
E_g	Band gap energy, eV
E_{VB}	Valence band potential, eV
h	Planck's constant, J·s
k_{app}	Apparent reaction rate constant, min^{-1}
n	Nature of transmission
t	Reaction time, min
v	Frequency of incident beam, Hz
e^-	Electrons
e_{CB}^-	Conduction band electrons
e_{tr}^-	Trapped electrons
h^+	Holes
h_{VB}^+	Valence band holes
h_{tr}^+	Trapped holes
hv	Photons
H^+	Hydrogen ion
$HO_2\bullet$	Hydroperoxyl radical
$O_2\bullet^-$	Superoxide radical
OH^-	Hydroxyl group

•*OH*	Hydroxyl radical
2D	Two-dimensional
ADMI	American Dye Manufacturer's Institute
AgI	Silver iodide
AGT	Average Germination Time
amu	Atomic mass unit
ANOVA	Analysis of Variance
AOPs	Advanced oxidation processes
As	Arsenic
ATR-FTIR	Attenuated Total Reflectance – Fourier Transform Infrared
Ba	Barium
BC	Biochar
Bi	Bismuth
Bi^{3+}	Bismuth (III) ion
$BiFeO_3$	Bismuth ferrite
$Bi(NO_3)_3$	Bismuth nitrate
$Bi(NO_3)_3{\cdot}5H_2O$	Bismuth nitrate pentahydrate
BiOBr	Bismuth oxybromide
BiOCl	Bismuth oxychloride
BiOF	Bismuth oxyfluoride
BiOI	Bismuth oxyiodide
$BiOIO_3$	Bismuth oxide iodate
$BiPO_4$	Bismuth phosphate
BiSI	Bismuth sulphoiodide
$BiVO_4$	Bismuth vanadate
$BiYO_3$	Bismuth yttrium oxide
Bi_2MoO_6	Bismuth molybdate
Bi_2O_2	Bismuth oxide
$Bi_2O_2CO_3$	Bismuth subcarbonate
Bi_2O_3	Bismuth (III) oxide
Bi_2S_3	Bismuth sulphide
Bi_2WO_6	Bismuth tungstate
$Bi_4Ti_3O_2$	Bismuth titanium oxide

BOD	Biochemical oxygen demand
BQ	Benzoquinone
C	Carbon
Ca	Calcium
CAGR	Compound annual growth rate
CB	Conduction band
CCNF	Cellulose carbon nanofiber
Cd	Cadmium
CdI_2	Cadmium iodide
CH_3COCH_3	Acetone
C_2H_5OH	Ethanol
C_2H_5NS	Thioacetamide
$C_6H_4O_2$	Benzoquinone
$C_{10}H_{16}N_2O_8$	Ethylenediaminetetraacetic acid
$C_{13}H_{14}N_4O$	1,5-Diphenylcarbazide
$C_{28}H_{31}N_2O_3Cl$	Rhodamine B
Cl	Chlorine
CO_2	Carbon dioxide
COD	Chemical oxygen demand
Cr	Chromium
CR	Congo red
Cr(III)	Trivalent chromium
Cr(VI)	Hexavalent chromium
Cu	Copper
$CuAlO_2$	Copper aluminium oxide
$CuInS_2$	Copper indium sulphide
CuS	Copper monosulphide
DI	Deionized
DNA	Deoxyribonucleic acid
DOE	Department of Environment
Dox	Doxycycline
DPC	1,5-Diphenylcarbazide
EDTA	Ethylenediaminetetraacetic acid
EDX	Energy Dispersive X-ray

EIS	Electrochemical Impedance Spectroscopy
ELISA	Enzyme-linked immunosorbent assay
ENR	Enrofloxacin
EQA	Environmental Quality Act
EtOH	Ethanol
Fe	Iron
Fe^{2+}	Iron (II) ion
$FeVO_4$	Iron vanadate
Fe_2O_3	Iron (III) oxide
GC	Gas Chromatography
GDP	Growth Domestic Product
GI	Germination index
GMF	Gemifloxacin
GO	Graphene oxide
GR	Germination Rate
HCA	Hydroxycitric acid
HCl	Hydrochloric acid
Hg	Mercury
HNO_3	Nitric acid
HPLC	High Performance Liquid Chromatography
HRTEM	High Resolution Transmission Electron Microscopy
H_2	Hydrogen
H_2O	Water
H_2O_2	Hydrogen peroxide
H_2SO_4	Sulphuric acid
IPEF	Internal polar electric field
IR	Infrared
IUPAC	International Union of Pure and Applied Chemistry
JCPDS	Joint Committee on Powder Diffraction Standards
KI	Potassium iodide
$K_2Cr_2O_7$	Potassium dichromate
$K_2S_2O_8$	Potassium persulfate
MB	Methylene blue

MIDA	Malaysian Investment Development Authority
MO	Methyl orange
Mo	Molybdenum
MoS_2	Molybdenum disulphide
M-S	Mott-Schottky
$NaHCO_3$	Sodium bicarbonate
NaI	Sodium iodide
NaOCl	Sodium hypochlorite
NaOH	Sodium hydroxide
Na_2SO_4	Sodium sulphate
$Na_2WO_4{\cdot}2H_2O$	Sodium tungstate dehydrate
Nb_2O_5	Niobium pentoxide
NHE	Normal Hydrogen Electrode
Ni	Nickel
NIR	Near-Infrared
NOR	Norfloxacin
O	Elemental oxygen
O_2	Molecular oxygen
O_3	Ozone
Pb	Lead
pH	Potential of Hydrogen
PL	Photoluminescence
POME	Palm oil mill effluent
ppm	Parts per million
RFN	Relative Frond Number
rGO	Reduced graphene oxide
RhB	Rhodamine B
RO	Reverse osmosis
ROS	Reactive oxygen species
S	Sulphur
SEM	Scanning Electron Microscopy
Sn	Tin
$SnCl_4{\cdot}5H_2O$	Tin (IV) chloride pentahydrate
SnS	Tin (II) sulphide

SnS_2	Tin (IV) sulphide
Sr	Strontium
$SrTiO_3$	Strontium titanium oxide
SS	Suspended solids
Ta	Tantalum
TC	Tetracycline
TC•HCl	Tetracycline hydrochloride
Ti	Titanium
TiO_2	Titanium dioxide
TOC	Total organic carbon
TPR	Transient Photocurrent Response
UNICEF	United Nations International Children's Emergency Fund
UiO-66-NH_2	Zirconium-based Metal-Organic Frameworks (MOFs)
UTAR	Universiti Tunku Abdul Rahman
UV	Ultraviolet
UV-vis DRS	Ultraviolet-visible Diffuse Reflectance Spectroscopy
VB	Valence Band
W	Tungsten
WHO	World Health Organization
WO_3	Tungsten (VI) oxide
WO_4	Tungstate (VI) ion
WO_6	Trioxido(oxo)tungsten
WSe_2	Tungsten diselenide
X-3B	Reactive Brilliant Red
Xe	Xenon
XPS	X-ray Photoelectron Spectroscopy
XRD	X-ray Diffraction
Zn	Zinc
$ZnIn_2S_4$	Zinc indium sulphide
ZnO	Zinc oxide

CHAPTER 1

INTRODUCTION

1.1 Background of Study

The survival of all living beings on Earth is dependent on the availability of water. Water resources are plentiful due to its 70 % coverage of Earth's surface. However, the majority of them are saline in nature, with only 2.5 % of them being drinkable fresh water, and even less than 1 % of this 2.5 % being accessible (Stephens, et al., 2020). Despite being a renewable resource, the scarcity of quality water continues to be a significant problem in many regions worldwide. On the other hand, development of the industries and technologies has been ongoing in recent years. Every process step necessitates the use of water, such as feed water for the boiler, cooling water for the heat exchanger, deionised water for chemical dilution, etc. According to Malay Mail (2020), Malaysia's daily water consumption per capita was 219 litres, which was significantly higher than the recommended rate of 160 litres per day. All of these steps will eventually convert fresh water into the wastewater by-product. Wastewater frequently contains pollutants that harm both the environment and human health. It could include heavy metals, organic and inorganic matter, toxic chemicals, toxic gases, microplastics, oil, bacteria and viruses (Abuhasel, et al., 2021). As reported, more than 80 % of the wastewater is discharged untreated into water bodies due to the high cost of treatment (Abuhasel, et al., 2021). According to the United Nations International Children's Emergency Fund (UNICEF) and the World Health Organization (WHO), about one-third of the world's population lacks access to safe drinking water due to water pollution, and the United Nations reports

that the contaminated water causes approximately 1.5 million deaths annually (Islam, 2020). Hence, conservation of water resources is a necessary action for humans in order to avoid water shortages that can threaten human food supply while also preserving the biodiversity of natural ecosystems.

Nowadays, synthetic dye is becoming increasingly important as a result of globalization and rising demand for textile or apparel goods (MIDA, 2019). An example of a synthetic dye is Rhodamine B (RhB). Rhodamine B, an important representative of xanthene dyes, is highly-soluble, basic and is extensively used in the laser dye, colouring paper, and textile industries due to its high stability (Saeed, et al., 2015). According to Manzoor and Sharma (2020), the total global dye production is approximately 800,000 tons per annum. Approximately 80-85 % of dyes are utilized, with 15 % of them being lost during different industry processes and released into the water bodies without further treatment. The colour released into the environment is possibly resulted from an aqueous drying process, where the incomplete exhaustion of dyes onto textile fibre happened. It is noted that the textile industry is responsible for contributing 22 % of the total volume of wastewater generated by various industries in Malaysia (Sundarajoo and Maniyam, 2019). On the other hand, there are numerous industries that generate heavy metal contaminated wastewater, such as pigments manufacturing, glass manufacturing, mining operations, and battery manufacturing processes (Badawi, Abd Elkodous and Ali, 2021). The most common heavy metals detected in industrial effluent include lead, cadmium, chromium, nickel, mercury, arsenic, zinc, and copper, in which the majority of them are located in the Period 4 of the Periodic Table, indicating that they are stable and hard to be removed (Shahbudin and Kamal, 2021). Heavy metals are hazardous because they are non-biodegradable and tend to bio-accumulate, posing a serious threat to biota and ecosystems (Shahbudin and Kamal, 2021). Among them, hexavalent chromium, Cr(VI) is known as an environmental contaminant as well as a human carcinogen. It is primarily used in metallurgical, refractory, and chemical industries (Tchounwou, et al., 2012). Water resources contaminated by industrial dyestuffs and Cr(VI) have become a huge obstacle to overcome. Therefore, it is indispensable to develop an advanced treatment technology to reduce/eliminate those contaminants and alleviate water environment issues.

Indeed, a variety of scientific approaches have been used for the dual function of dye degradation and Cr(VI) reduction in wastewater, including adsorption (Badawi, Abd Elkodous and Ali, 2021), membrane filtration (Coker, et al., 2013), and biological processes (Shim, et al., 2015). However, the above solutions are constrained by high operating costs, stringent working conditions, and the potential formation of secondary pollutants (Wei, et al., 2020). Hence, a more efficient method has been proposed in recent decades. Advanced oxidation processes (AOPs) are gaining popularity as an effective means of degrading organic pollutants and reducing heavy metal levels in wastewater (Deng and Zhao, 2015). AOPs, including photolysis (UV + H_2O_2), photocatalysis (light + catalyst), sonolysis (ultrasounds), ozonolysis (O_3), Fenton (Fe^{2+} + H_2O_2), photo-Fenton (solar light + Fenton), and their appropriate combinations, are chemical oxidation techniques that generate non-selective reactive oxygen species (ROS), primarily hydroxyl radicals (•*OH*) with a high redox potential, E^o of 2.80 eV (Garrido-Cardenas, et al., 2019). Formation of other reactive species such as hydrogen peroxide (H_2O_2) and superoxide anion radicals (O_2•$^-$) also occurs. These ROS are known for their capability in degrading recalcitrant organic pollutants and removing certain inorganic pollutants in wastewater (Deng and Zhao, 2015). Among AOPs, heterogeneous photocatalysis is believed to be the most effective, cost-effective, sustainable and environmentally friendly technology for removing dyes and heavy metals from effluent water. This technology combines the semiconductor catalyst, emitted light (UV or visible), and oxidizing agent. The principal mechanism of photocatalysis involves the generation of photo-induced electron-hole pairs, excitation and separation, followed by the simultaneous oxidation and reduction reactions with the species adsorbed on the active surface (e.g. H_2O, O_2), producing ROS that decompose the pollutants. (Baruah, et al., 2019)

Bismuth tungstate, Bi_2WO_6 is a ternary metal oxide semiconductor with a unique orthorhombic crystal structure and a band gap of 2.6 to 2.9 eV. Induction of internal polar electric field (IPEF) between the $[WO_4]^{2-}$ octahedral layers and $[Bi_2O_2]^{2+}$ slabs able to improve its photocatalytic performance (Orimolade, et al., 2021). Among the Bi-based photocatalysts, Bi_2WO_6 possesses greater visible light

photocatalytic activity. However, its limited visible light responsiveness and rapid recombination of photo-induced carriers restrict its potential environmental applications (Lu, et al., 2018). To address these shortcomings, coupling Bi_2WO_6 with a narrow band gap semiconductor has been proposed as a viable solution capable of inhibiting the recombination of electron-hole pairs and expanding the visible light response range of Bi_2WO_6 (Lu, et al., 2018). As such, tin disulphide, SnS_2 is a promising candidate for metal-sulphide-metal-oxide heterojunction based photocatalyst with narrow band gap (2.2 - 2.4 eV) (Kumar, et al., 2022). SnS_2 has the similar remarkable benefits as Bi_2WO_6, making it to be engrossed much consideration lately as a new type of photocatalyst for absorbing visible light for degrading pollutants. Furthermore, the energy band positions of SnS_2 and Bi_2WO_6 match each other, according to the theory of energy band matching (Xu, et al., 2022).

1.2 Problem Statement

Water pollution caused by organic compounds (e.g. Rhodamine B) and heavy metals (e.g. Cr(VI)) has severely affected aquatic biota and ecological balance. Rhodamine B (RhB), a non-biodegradable xanthene dye that is widely used as a colorant and water tracer, but it has potential toxicity and carcinogenicity which have negative impacts to biological ecosystems and human health (Shen and Gondal, 2017). Similarly, Cr(VI) compounds are toxins and known to be living organism carcinogens. They have the potential to induce severe diarrhoea, lung congestion, and kidney impairment (Yunus, Zuraidah and John, 2020). Breathing high levels of Cr(VI) can cause irritation to the nasal lining, nose ulcers, runny nose, and breathing problems such as asthma, coughing, and shortness of breath (Yunus, Zuraidah and John, 2020). It is therefore critical to degrade RhB, and convert Cr(VI) to Cr(III), which poses a far lower risk.

To meet stricter environmental regulations, several techniques have been employed to remove dyes and heavy metals from wastewater, including physical, chemical, and biological treatments. All of these treatments have their own limitations despite being widespread applied till now. Biological treatment process can be classified into aerobic and anaerobic, which uses the biological matter and bacteria to collapse the waste matter and nutrients. However, the aerobic process generates large amounts of biological sludge, whereas the anaerobic treatment method is insufficient to reduce the pollutant levels to acceptable standards. Besides, biological treatment process requires longer microorganisms' acclimatization duration, higher energy consumption, larger tank and higher maintenance costs. Physical treatment such as sedimentation, aeration, filtration, and stripping are used to transfer the pollutants from water to another phase, but this merely shifts toxic materials from one medium to another, which does not aid long-term waste management or eliminate the environmental impact of hazardous waste. Furthermore, cleaning of physical treatment method is inconvenient, and the temperature changes have a significant impact on the tank. Conventional chemical treatment utilizes various chemicals to treat the wastewater, such as chlorine, ozone, and neutralization. It is not recommended for use because of the high consumption of hazardous

chemical reagents, which may cause other environmental issues. In short, these treatment methods are deemed insufficient for degradation due to low removal efficiency, high post-treatment costs, and the possibility of secondary pollution. (Lam, et al., 2012)

In the last few years, advanced oxidation processes (AOPs) have been discovered to be suitable for the effective treatment of wastewater containing hazardous chemicals. The technologies rely on the in-situ generation of strong oxidants, such as hydroxyl radicals and sulphate radicals, to oxidize organic pollutants. Among AOPs, heterogeneous photocatalysis driven by light has garnered a lot of attention because of its exceptional performance in eliminating pollutants via the generation of photoexcited reactive radicals (Lam, et al., 2012). As compared with biological treatment, photocatalysis is more environmentally friendly as it does not lead to secondary environmental pollution and allows for the rapid and complete mineralization of organic dyes (Pang and Abdullah, 2013). Moreover, the photocatalysis process uses the free and inexhaustible solar light of 5 % UV and 42 % visible light, which is economical and advantageous, particularly in Malaysia where there is an abundance of sunlight. (Lam, et al., 2012) Semiconductor-based photocatalytic reactions are typically heterogeneous in nature, meaning that the photocatalyst and targeted molecules are in different phases (Baruah, et al., 2019). Semiconductor catalysts are typically oxides (e.g. titanium dioxide, TiO_2) that are more desirable than the conventional chemical oxidation techniques due to their low cost, non-toxicity, and capacity to be used for prolonged periods without a significant reduction in photocatalytic activity (Lam, et al., 2012). Overall, heterogeneous photocatalyst is preferable than homogenous photocatalyst because of its chemical stability in aqueous solution and ease of recovery after application (Baruah, et al., 2019).

Recently, bismuth tungstate, Bi_2WO_6 has emerged as a viable non-TiO_2 semiconductor photocatalyst due to its distinct band structure, low cost, and a number of remarkable chemical and physical properties. Bi_2WO_6 is a ternary metal oxide semiconductor with unique orthorhombic crystal structure and internal electric field (Orimolade, et al., 2021). It is considered as an ideal candidate for visible-light

responsive photocatalysis among the Bi-based photocatalysts because of its relatively small band gap of 2.6 to 2.9 eV (Lu, et al., 2018). However, despite having some response to visible light, its visible light responsiveness is still considered poor, with the electrons and holes generated by illumination having a high probability of direct recombination, resulting in low photon quantum efficiency (Xu, et al., 2022). In addition, single Bi_2WO_6 has weak reduction ability because of its relatively positive conduction band (Zhang, et al., 2019). In light of these issues, it is critical to implement some effective modifications to Bi_2WO_6 in order to improve its properties and practical application.

Various approaches have been employed to improve the visible light photocatalytic performance of Bi_2WO_6, including metal or non-metal doping, mesoporous structure construction, surface coupling hybridization, and the coupling of two semiconductor photocatalysts (Lu, et al., 2018). In this context, constructing a Bi_2WO_6-based heterojunction photocatalyst incorporated with other semiconductors with narrow band gaps and matched band potentials has the potential to provide synergistic effects such as the extended visible light absorption and the effective electron-hole pair separation. According to Kumar, et al. (2022), tin disulphide, SnS_2, a small band gap material (2.2 - 2.4 eV), can be a potential candidate for a metal-sulphide-metal-oxide heterojunction-based photocatalyst due to its efficient visible light adsorption. SnS_2 has a large surface area, is low in cost, is less toxic, and has good chemical and thermal stability. The energy band positions of SnS_2 and Bi_2WO_6 are matched according to energy band matching theory, and the combination of SnS_2 and Bi_2WO_6 can effectively reduce the recombination of photogenerated electron-hole pairs, thereby enhancing the photocatalytic efficiency (Xu, et al., 2022). As a result, Bi_2WO_6/SnS_2 nanocomposite is used in this study to determine its efficiency in Rhodamine B degradation and Cr(VI) reduction under sunlight irradiation.

1.3 Objectives

This research project encompasses three major objectives, which are:

i) To synthesize solar light-induced Bi_2WO_6/SnS_2 heterojunction photocatalyst via a hydrothermal-deposition method.

ii) To characterize the physical, chemical, optical and electronic properties of synthesized Bi_2WO_6/SnS_2 photocatalyst.

iii) To investigate the effectiveness of as-fabricated Bi_2WO_6/SnS_2 photocatalyst on degradation of Rhodamine B and reduction of chromium (VI) ions under sunlight irradiation.

1.4 Scope of Study

Bi_2WO_6/SnS_2 heterojunction photocatalyst was produced using a hydrothermal-deposition method with various SnS_2 loading amounts. Following that, the as-synthesized powdered photocatalysts underwent a range of characterization techniques such as X-ray Diffraction (XRD), Attenuated Total Reflectance – Fourier Transform Infrared Spectroscopy (ATR-FTIR), Ultraviolet-visible Diffuse Reflectance Spectroscopy (UV-vis DRS), Transient Photocurrent Response (TPR), Electrochemical Impedance Spectroscopy (EIS) and Mott-Schottky (M-S) analysis. The photocatalytic efficiency of the synthesized in degrading Rhodamine B and reducing the chromium (VI) ions under sunlight exposure was then investigated. The treated effluent will then be used again for the phytotoxicity test. Lastly, radical scavenging experiments were conducted for the purpose to identify the active species present during photocatalytic activity.

.

CHAPTER 2

LITERATURE REVIEW

2.1 Water Pollution

Water pollution refers to the accumulation of toxic chemical and biological agents in the water bodies, including groundwater, rivers, lakes, and oceans (Environmental Pollution Centres, 2017). There are two primary sources of water pollution: point sources and non-point sources. Point sources are discharged from a single location, such as manufacturing-based industries, animal farms, and sewage treatment facilities, through pipelines and emissaries. This source is simple to identify, control and monitor. Non-point source pollution, on the other hand, is the pollution from diffused sources, such as surface runoffs and agricultural activities, which are difficult to monitor and control. This is common along the river which is close to a number of factories. (Afroz and Rahman, 2022)

Over the last century, industrialization has grown at a rapid pace, resulting in an increase in the demand for the exploitation of natural resources, which has in turn worsened environmental problems, including water pollution. It has had a significant impact on freshwater supply from the total water resources, with the water quality becoming a major concern of government and non-government authorities. Industrial effluent, which is one of the major sources of wastewater, might contain heavy metals, organic and inorganic matter, oil, bacteria and viruses. Rhodamine B and Cr(VI) are present. Untreated wastewater has the potential to contaminate drinking water sources and spread infectious diseases like cholera and typhoid fever.

Exposure to contaminated water has also been linked to health complications like poor blood circulation, vomiting, and nervous system damage.

Water pollution is a major concern in Malaysia, posing significant threats to the sustainability of water resources, public health, and the economy. There is an abundance of water and water resources, but the supply is inadequate due to pollution, either natural or man-made. Typically, urbanization alters runoff quality, resulting in a decrease in the quality of receiving waters. Accumulated pollutants on the ground surface are washed into rainwater systems by rainfall. Also, wastewater from different zones, including residential, commercial and industrial areas, contributes to the contamination of rivers and rainwater facilities, often resulting in an unpleasant smell. To address this issue, Malaysia has developed several water resource policies, including the National Policy and the Environmental Quality Act 1974 (EQA). Nevertheless, individual awareness is critical in preserving the quality of water sources and preventing further pollution. (Afroz and Rahman, 2022)

Figure 2.1 depicts Asia's national water security index. Although Malaysia meets the moderate water quality standard set by National Water Security, with an index of 3 indicating "capable", there is still room for development in water and wastewater treatment to improve water quality and help in solving the problems faced by some other Asian countries.

Economy	KD1	KD2	KD3	KD4	KD5	NWSI Score	NWSI
Scale	1–20	1–20	1–20	1–20	1–20	1–100	1–5
Japan	19.0	14.3	18.5	16.5	19.6	87.9	4
Kazakhstan	16.0	16.1	15.9	9.4	16.3	73.7	3
Kiribati	7.0	11.3	5.9	16.2	7.9	48.2	2
Korea, Republic of	20.0	15.6	18.2	10.4	19.7	84.0	4
Kyrgyz Republic	13.0	10.8	16.2	15.0	17.6	72.6	3
Lao People's Democratic Republic	7.0	9.2	15.9	13.0	10.1	55.2	2
Malaysia	14.0	15.5	11.5	15.4	18.2	74.7	3
Maldives	20.0	10.7	9.7	7.6	14.8	62.8	3
Marshall Islands	9.0	7.0	9.1	15.1	8.6	48.9	2

Figure 2.1: Scores and National Water Security Index (Asian Development Bank, 2020).

2.2 Review on Dye and Heavy Metals in Wastewater

According to Farhana, Mahamude and Mica (2022), Malaysia has experienced significant industrial growth and export development in the past decade, with well-established infrastructure for commercial clothing trading and manufacturing industries and services. The textile and apparel industry, in particular, has contributed 1.70 % to the rise of the manufacturing sector's Gross Domestic Product (GDP) in 2012, and it has an anticipated annual growth rate 7.80 % (Farhana, Mahamude and Mica, 2022). Additionally, the Malaysian Investment Development Authority (MIDA) reported in 2019 that the textile and apparels industry was worth approximately US$ 920 million in 2018 and is expected to grow at a CAGR of around 4.4 % to reach US$ 1.2 billion by 2024 (MIDA, 2019). The rapid growth and production are primarily driven by rising global market demand and rising purchasing power in major importing countries.

However, textile industry consumes a substantial amount water, and the extensive production and prevalent use of organic dyes, particularly during the dyeing and finishing process, have led to a high discharge rate of textile waste containing numerous pollutants, such as colour, suspended solids (SS), total organic carbon (TOC), and toxic metals (Pang and Abdullah, 2013). Dyes without proper treatment also contains significant amounts of polyphenylene ring substituents, which exhibit biotoxicity and chromaticity (Chen, et al., 2021). Regarding the heavy metal content, it appears as impurities or as part of the dye molecule. These metals are crucial components of the dye that affect colourfastness (Verma, 2008). However, heavy metals in the wastewater can cause harmful impacts on both the environment and human health. Table 2.1 summarizes the common metals found in various dye classes.

Table 2.1: Common Metals Found in Different Dye Classes (Verma, 2008).

Dye class	Metals in dyes
Acid dyes	Copper, lead, zinc, chrome, cobalt
Basic dyes	Copper, zinc, lead, chromium
Direct dyes	Copper, lead, zinc, chromium

Mordant dyes	Chrome
Pre-metallized	Cobalt, chrome, copper
Reactive dyes	Copper, chromium, lead
Vat dyes	None
Disperse dyes	None

According to Pang and Abdullah (2013), the textile industry has been reported to consume a substantial amount of water, with a maximum daily consumption reaching 3000 m^3, which corresponds to 22 % of the total industrial wastewater produced in Malaysia. In Figure 2.2, the textile industry's contribution to water pollution in various Malaysian states is illustrated. The figure shows that Peninsular Malaysia is where the discharges of textile wastewater are mostly concentrated. Johor, Pulau Pinang, and Selangor have the highest number of water pollution sources (28.6 %, 28.2 %, and 15.6 %, respectively), which is in accordance to the number of textile finishing factories situated in these states.

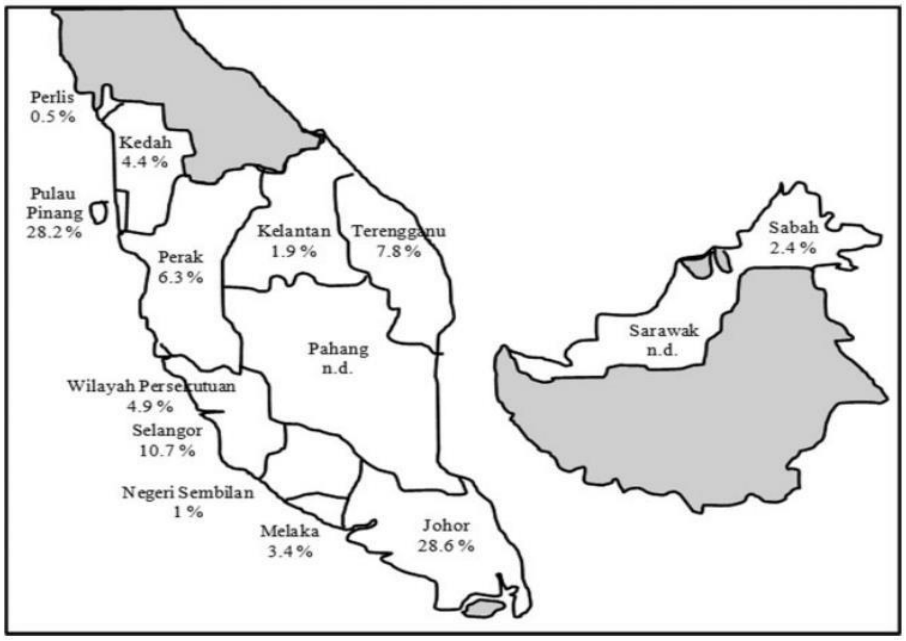

Figure 2.2: Contribution of Textile Industry to Water Pollution for Different States in Malaysia (Pang and Abdullah, 2013).

On the other hand, rapid industrialization results in excessive heavy metal emission into the surrounding environment, which has been a matter of global concern due to their chronic toxicity. Heavy metals are primarily produced by mining, pigment manufacturing, electrical power plants, electroplating, metal manufacturing, and petroleum refining (Badawi, Abd Elkodous and Ali, 2021). Heavy metals are inorganic substances with atomic weights of 63.5 – 200.6 amu and at least 5 times the density of water (Tchounwou, et al., 2012). Environmental exposure to high concentrations of heavy metals can cause a variety of illnesses, including cancer and kidney damage, because heavy metals are non-biodegradable and will accumulate in living organisms, unlike organic matter (Tchounwou, et al., 2012). The most common heavy metals include zinc (Zn), copper (Cu), chromium (Cr), cadmium (Cd), nickel (Ni), mercury (Hg), lead (Pb), and arsenic (As). According to Yunus, Zuraidah and John (2020), sediments play an important role in assessing heavy metal contamination as they are a vital sink for diverse pollutants in the aquatic systems, including heavy metals. Table 2.2 summarizes the distribution of the aforementioned heavy metal trace elements in coastal sediments of Peninsular Malaysia. The highest concentration of chromium was found in Port Klang, a heavy industrial area on Malaysia's western coast, at 388.84 ppm dry weight.

Following that, Table 2.3 lists the standard to be followed by industrial effluent before discharge established by government of Department of Environment. Standard A pertains to effluent discharge into any inland waters within the catchment region defined in the Environmental Quality Act's Six Schedule, whereas Standard B pertains to effluent discharge into any other inland waters or Malaysian waters (Department of Environment, 2009). Based on the requirement, the intensity of dyes in the coloured effluents should not exceed 100 ADMI for both standards A and B, and the Cr(VI) concentration in the effluent should not exceed 0.05 mg/L for both standards A and B.

Table 2.2: Distribution of Heavy Metal (ppm Dry Weight) in Peninsular Malaysia Coastal Sediment (Yunus, Zuraidah and John, 2020).

Heavy Metal Location	Pb	Hg	Cd	As	Cu	Zn	Cr	Ni
Peninsular Malaysia								
Malaysia Coast	8.67	-	4.35	-	18.42	196.07	-	4.99
Peninsular Malaysia	12.21	-	0.16	6.13	9.59	49.82	41.48	23.86
Mangrove Peninsular	98.97	2.90	1.56	41.43	17.15	100.96	40.92	-
Water in Malaysia	-	22.84	-	-	-	-	-	-
South Coast								
South China Coastal	33.70	-	-	-	24.21	-	-	-
Strait of Johor	52.52	-	0.30	27.30	57.84	210.45	55.50	18.31
South West Malaysia	0.07	4.64	-	18.00	25.60	-	-	-
North Coast								
Juru River	-	-	-	-	2.87	34.41	-	7.8
Northern Peninsular	-	-	1.64	-	-	258.50	-	40.00
Kilim River	6.38	-	7.49	-	-	67.35	-	-
Bayan Lepas, Penang	35.45	-	1.70	-	56.03	-	37.96	51.50

Table 2.2 (cont.): Distribution of Heavy Metal (ppm Dry Weight) in Peninsular Malaysia Coastal Sediment (Yunus, Zuraidah and John, 2020).

Heavy Metal Location	Pb	Hg	Cd	As	Cu	Zn	Cr	Ni
Western Coast								
Sepang Besar River	16.00	-	0.28	-	23.00	55.00	-	-
Offshore West Coast	-	-	0.76	-	-	41.53	-	-
Intertidal West Coast	-	-	1.01	-	-	154.66	-	-
Western (marine)	64.92	-	-	-	67.96	286.40	-	-
Western (freshwater)	38.71	-	-	-	18.85	175.50	-	-
Port Klang	128.98	-	0.810	475.26	118.34	492.39	388.84	74.56
West Coast	0.56	-	-	-	0.18	0.37	1.30	0.21
Langat River	30.44	-	-	16.19	5.72	35.87	15.88	4.47
Sungai Puloh	78.84	-	0.94	-	46.89	1023.68	-	35.54
Bernam River	-	-	0.62	-	-	-	14.90	5.30
East Coast								
East Coast Peninsular	37.40	0.10	0.25	14.90	9.30	44.30	46.40	20.10
Terengganu River	32.70	0.18	0.99	11.98	-	-	-	-
Kuantan River	0.01	0.04	-	42.30	42.03	9.08	3.35	-
Balok River	29.30	-	0.50	-	24.30	159.40	42.90	16.00

Table 2.3: Acceptable Conditions for Discharge of Industrial Effluent or Mixed Effluent of Standards A and B (Department of Environment, 2009).

Parameter	Unit	Standard A	Standard B
(i) Temperature	℃	40	40
(ii) pH value	-	6.0-9.0	5.5-9.0
(iii) BOD_5 at 20℃	mg/L	20	50
(iv) Suspended Solids	mg/L	50	100
(v) Mercury	mg/L	0.005	0.05
(vi) Cadmium	mg/L	0.01	0.02
(vii) Chromium, Hexavalent	mg/L	0.05	0.05
(viii) Chromium, Trivalent	mg/L	0.20	1.0
(ix) Arsenic	mg/L	0.05	0.10
(x) Cyanide	mg/L	0.05	0.10
(xi) Lead	mg/L	0.10	0.5
(xii) Copper	mg/L	0.20	1.0
(xiii) Manganese	mg/L	0.20	1.0
(xiv) Nickel	mg/L	0.20	1.0
(xv) Tin	mg/L	0.20	1.0
(xvi) Zinc	mg/L	2.0	2.0
(xvii) Boron	mg/L	1.0	4.0
(xviii) Iron (Fe)	mg/L	1.0	5.0
(xix) Silver	mg/L	0.1	1.0
(xx) Aluminium	mg/L	10	15
(xxi) Barium	mg/L	1.0	2.0
(xxii) Fluoride	mg/L	2.0	5.0
(xxiii) Formaldehyde	mg/L	1.0	2.0
(xxiv) Phenol	mg/L	0.001	1.0
(xxv) Free Chlorine	mg/L	1.0	2.0
(xxvi) Sulphide	mg/L	0.50	0.50
(xxvii) Oil and Grease	mg/L	1.0	10
(xxviii) Ammoniacal Nitrogen	mg/L	10	20
(xxix) Colour	ADMI*	100	200

*ADMI – American Dye Manufacturers Institute

2.3 Usage and Hazardous Effects of Rhodamine B and Chromium

Table 2.4: General Properties of Rhodamine B (Saeed, et al., 2015; Al-Hamdani, 2017).

Molecular structure	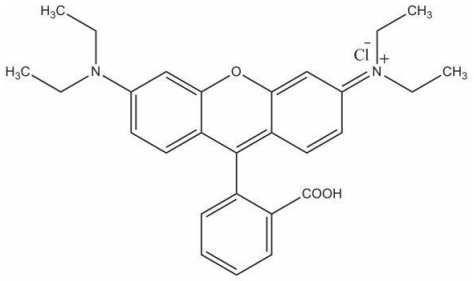
Molecular formula	$C_{28}H_{31}N_2O_3Cl$
IUPAC name	9-(2-Carboxyphenyl)-6-(diethylamino)-N,N-diethyl-3H-xanthen-3-iminium chloride
Colour Index number	45170:1
Appearance	Greenish powder
Molecular weight	479.02 g/mol
Density	0.79 g/mL
Melting point	210-211 ℃
Solubility	Soluble in some solvents such as ethanol and water

Rhodamine B (RhB) is an organic chloride salt and a basic red dye in xanthene class. It is primarily used as colourant in textiles, paper printing, plastic, wool, silk, and leather (Raziq Rahimi Kooh, Khairud Dahri and Lim, 2016). Rhodamine dyes tend to self-associate in various liquid crystal host materials, such as ethanol, which is crucial in display and electronic technologies. It is frequently used as a fluorescent dye for quantifying fluid mixing in aqueous solution, as well as a tracer dye for determining the direction and rate of flow and transport in water. As a result, it is widely utilized in biotechnology applications like enzyme-linked immunosorbent assay (ELISA), flow cytometry, fluorescence microscopy, and fluorescence correlation spectroscopy. (Al-Kadhemy, Alsharuee and Al-Zuky, 2011) RhB fluorescence is negligibly pressure sensitive and pH independent, allowing it to be used as a mitochondrial probe and optical thermometer in cells (Moreau, et al., 2015).

In addition, RhB, which is tuneable around 610 nm, serves as the medium of tuneable visible-light laser radiation (Al-Kadhemy, Alsharuee and Al-Zuky, 2011). Moreover, RhB was previously widely used as a food colorant in paprika- or chili-containing foods, but it has recently been banned as a food contamination that requires routine monitoring and strictly regulation (Wang, et al., 2018).

Experimental evidence has confirmed the harmful effects of RhB dye towards human and animals, which includes carcinogenicity, neurotoxicity, reproductive and developmental toxicity, as well as chronic toxicity (Jain, et al., 2007; Shen and Gondal, 2017). Rhodamine B is hazardous to one's health because it contains heavy metals and chlorine (Cl) compounds. The radical activity of chlorine compounds can damage macromolecules such as carbohydrates, proteins, nucleic acids, and fats, as well as induce toxic cancer triggers in humans (Rohmawati, et al., 2021). If consumed by humans or animals, RhB can irritate the eyes, skin, and respiratory tract. According to Rohmawati, et al. (2021), exposure to RhB can slow down the oestrus cycle length and cause folliculogenesis, which stops the development of follicles. Nonetheless, this prohibited colorant is still found in some food products, with one example being the inclusion of RhB as an unauthorized food additive in candies and chilli sauce in many developing countries (Du, et al., 2022). RhB has also been linked to DNA damage in certain cell lines (Honeychurch, 2022). Drinking water tainted with RhB dyes is medically proven that it can lead to the high-carcinogenic subcutaneous tissue borne sarcoma (Shen and Gondal, 2017). Furthermore, one study has shown that exposure to RhB can lead to decreased reproductive ability, growth retardation, behavioural effects, and tumour development in rats (Honeychurch, 2022). Aside from that, dyes in water tends to obstruct direct sunlight, resulting in a reduction in the photosynthesis rate of aquatic flora and the amount of oxygen available to aquatic living organisms (Wierzbicka, et al., 2022). As a result, water quality parameters such as COD, BOD, and pH will be altered, affecting the ecological balance in water and threatening the aquatic life ecosystem. Ingestion of a low concentration of RhB by aquatic organisms can result in respiratory and reproductive system damage, tissue necrosis, and even cancer (Du, et al., 2022). Therefore, because of the hazardous nature and harmful effects of Rhodamine B, it is thought worthwhile to remove it from wastewater.

Table 2.5: General Properties of Chromium (Helmenstine, 2019).

Symbol	Cr
Atomic Weight	51.9961
Density (g/cc)	7.18
Boiling Point & Melting Point (K)	2945; 2130
Electron Configuration	[Ar] $4s^1$ $3d^5$
Oxidation States	6, 3, 2, 0

On the other hand, chromium (Cr) is a naturally occurring element in the earth's crust and is utilized extensively in a variety of industries, including metallurgical, chemicals, and refractory (Tchounwou, et al., 2012). These industries utilize chromium in processes such as metal processing, ferrochrome production, stainless steel welding, leather tanning, and wood preservation. There are two oxidation states of chromium ion: trivalent chromium Cr(III) and hexavalent chromium Cr(VI). Cr(III) is stable and naturally occurs in ores (e.g. ferrochromite), while Cr(VI) is less stable (Tchounwou, et al., 2012). At low doses, Cr(III) is less toxic than Cr(VI) (Coker, et al., 2013). There have been no reports of significant toxic effects of Cr(III). It has been identified as an essential micronutrient in humans and animals, potentiating the insulin action and providing nutritional enhancement to energy, glucose, lipid, and protein metabolism (Tchounwou, et al., 2012; Swaroop, et al., 2019). Several dietary benefits are portrayed as appetite regulation, sugar craving reduction, and increased lean body mass (Swaroop, et al. 2013).

Chromium is commonly utilized in various industrial procedures, but it has been designated as a human carcinogen by several regulatory and non-regulatory agencies due to its contamination in many environmental systems (Tchounwou, et al., 2012). It is typically discharged into the environment as Cr(VI), as a result of human activity. According to research findings, Cr(VI) is easily absorbed by the human body, is highly soluble, and is 100-fold more toxic and mobile than Cr(III) (Chromium Toxicity, 2008; Shim, et al., 2015). Coker, et al. (2013) also stated that Cr(VI) is carcinogenic, teratogenic, and mutagenic. Population exposure to chromium can be classified into non-occupational (ingestion of chromium-laden

water and food, direct skin contact) and occupational (skin contact and inhalation). Workers in chromium-related industries are exposed to the levels of chromium at a magnitude of two orders greater than those of the general population. It has been reported that long-term environmental and occupational exposure to Cr(VI)-containing compounds has been associated with multi-organ toxicity, including respiratory tract cancer, renal damage, skin irritation, asthma, and allergy. Cr(VI) cytotoxicity has the capacity to induce DNA damage, such as DNA fragmentation, chromosomal aberrations, and DNA strand breaks. Next, animals that consume Cr(VI) compounds frequently exhibit respiratory problems, ulcers, infertility, birth defects, and tumour formation. (Tchounwou, et al., 2012) Aside from that, Cr(VI) is toxic to agricultural plants at concentrations of 5 – 100 mg/g in soil and 0.5 – 5.0 mg/mL in nutrient solution (Stambulska, Bayliak and Lushchak, 2018). The enhanced production of reactive oxygen species (ROS), such as hydroxyl radical (•*OH*), is one of the most critical hallmarks of Cr(VI) toxicity. If the plant's defensive mechanism capacity is insufficient, the ROS will considerably alter the biomolecules, resulting in oxidative stress and unfavourable effects on the plant, such as inhibited growth of root and aboveground parts (Stambulska, Bayliak and Lushchak, 2018). Overall, the detoxification of Cr(VI) to Cr(III) is required to mitigate its toxic impact on the living organisms and environment.

2.4 Heterogeneous Photocatalysis

The demand for environmentally friendly, renewable and sustainable energy, as well as remediation of the environment, has sparked a surge in photocatalysis research (Tan, Abdi and Ng, 2019). Photocatalysis is the acceleration of a chemical reaction under ambient settings by a photocatalyst under the influence of a light source (either solar or artificial). The photocatalytic process is consistent with the Sustainable Development Goals of United Nation, particularly the "Clean Water and Sanitation" of Goal 6 (Nunes et al., 2021). Hence, it is used in a variety of fields, including the reduction of H_2 through water splitting, reduction of CO_2 into organic fuels, and organic degradation to reduce environmental pollution (Tan, Abdi and Ng, 2019). Heterogeneous catalysis arises from different phases, such as the solid-liquid interface, with multiple active sites such as faces, edges, and defects, which work concurrently (Thongam and Chaturvedi, 2021). In the field of heterogeneous photocatalysis, semiconductor-based materials have sparked tremendous research for the photo-oxidation of organic and inorganic contaminants. A semiconductor, either organic or inorganic, is used to achieve the desired photochemical reaction (Tan, Abdi and Ng, 2019). It possesses an explicit energy band structure consisting of a high energy conduction band (CB) and a low energy valence band (VB), enabling it to act as sensitizer of light-induced oxidation processes (Zhang et al., 2019). Semiconductors are resistant to photo-corrosion, chemically inert, cost-effective, and environmentally benign, and can harvest the green, abundant, and sustainable sunlight as a primary energy source (Tan, Abdi and Ng, 2019). One example is TiO_2, the most popular photocatalyst due to the previously mentioned characteristics, as well as its high efficiency and versatility in different reaction media.

In essence, there are three distinct intrinsic properties that dictate the overall efficiency of a semiconductor photocatalyst: (i) the band gap (E_g), which refers to the energetic gap between the valence band maximum (E_{VB}) and the conduction band minimum (E_{CB}); (ii) the absolute potentials of the E_{CB} and E_{VB} (e.g. band position); and (iii) the behaviours of charge carriers within the semiconductor, encompassing diffusion length, lifetime, mobility, surface charge recombination rate, and interfacial charge transfer. As depicted in Figure 2.3, the band gap (E_g) of a semiconductor photocatalyst determines its ability to absorb light and, hence, its efficiency in solar

conversion. As a general rule, a semiconductor with E_g greater than 3.0 eV is restricted to UV light absorption, indicating a large band gap, whereas a semiconductor with a smaller band gap can harvest solar energy more efficiently. The E_{CB} and E_{VB} potentials determine the electrons' reductive power and the holes' oxidative power following photoexcitation. Specifically, the E_{CB} must be more negative (higher) than the reduction potential to drive the reduction of the electron acceptor ($A + e^- \rightarrow A^-$), whereas the E_{VB} has to be more positive (lower) than the oxidation potential to facilitate the oxidation of the electron donor ($D + h^+ \rightarrow D^+$). The number and efficiency of active charge carriers that continue to participate in the interfacial processes at the semiconductor/solution phase boundary while competing with charge recombination depend on how the photoinduced electrons and holes behave. (Tan, Abdi and Ng, 2019)

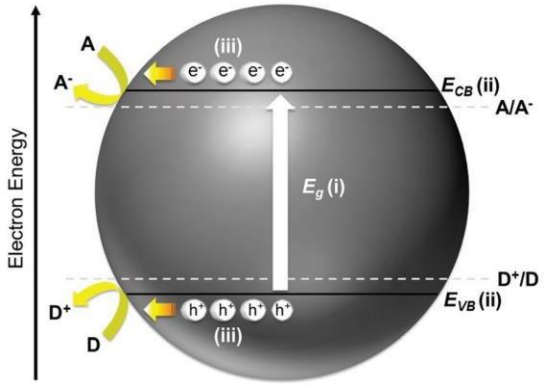

Figure 2.3: The Key Aspects Governing the Photochemical Efficiency of a Semiconductor Photocatalyst (Tan, Abdi and Ng, 2019).

2.5 Bi_2WO_6 as Photocatalyst

Bismuth tungstate, Bi_2WO_6 belongs to the family of layered perovskites called Aurivillius oxides, which are ternary metal oxide and n-type semiconductors. The general formula is $Bi_2A_{n-1}B_nO_{3n+3}$, where A is a large 12-coordinate cation (such as Ca, Ba, Pb) and B is a smaller 6-coordinate cation (Ti, Mo, Fe). Bi_2WO_6 is the most basic member of this group, and it is one of the intermediate oxides found in the pseudo-binary phase system of Bi_2O_3-WO_3, along with Bi_4WO_9, $Bi_2W_2O_9$, $Bi_{14}WO_{24}$ and Bi_6WO_{12}. However, Bi_2WO_6 exhibits greater visible light photocatalytic activity than either Bi_2O_3 or WO_3. Bi_2WO_6 has a narrow band gap of 2.6 to 2.9 eV, which is advantageous for the photocatalytic wastewater contaminant removal. Unlike TiO_2 or ZnO, which have larger band gaps (3.0 to 3.4 eV) that restrict the semiconductor to absorb in ultraviolet region, Bi_2WO_6 is able to harvest energy in the visible light spectrum with around 470 nm of visible light absorption edge. UV absorption is undesirable because it only accounts for about 5% of the solar spectrum (Li, Li and Zhou, 2020). The weak photosensitivity of TiO_2 under visible/solar irradiation is the greatest barrier, therefore Bi_2WO_6 was chosen over TiO_2. Bi_2WO_6 demonstrates the best photocatalytic activity under visible light among other bismuth based oxides. Other advantages of Bi_2WO_6 include relatively non-toxic, catalytic behaviour, has good electrical and photostability. (Orimolade, et al., 2021)

The exceptional visible light irradiation performance of Bi_2WO_6 can be ascribed to its distinct structure. Bi_2WO_6 is characterized by an orthorhombic configuration at room temperature and more than 900 ℃ of Curie temperature (Orimolade, et al., 2021). When subjected to temperatures of 600 – 700 ℃, a phase transformation occurs, leading to alterations in the lattice parameters of Bi_2WO_6 (Orimolade, et al., 2021). The orthorhombic crystal structure of Bi_2WO_6 is shown in Figure 2.4, where the perovskite-like tungsten oxide $[WO_4]^{2-}$ octahedral layers are sandwiched between the bismuth oxide $[Bi_2O_2]^{2+}$ slabs by the van der Waals interaction (Orimolade, et al., 2021). $[WO_4]^{2-}$ layers have a structure similar to that of WO_3, which is well-known for the charge carrier storage and release (Yang, et al., 2021). This layered structure is advantageous for the swift and effective photogenerated charge carriers separation and the generation of internal electric fields, known as internal polar electric field (IPEF) (Guo, et al., 2021), between the

layers, resulting in improved photocatalytic performance. Thus, Bi_2WO_6 has garnered significant interest owing to its exceptional properties, particularly for photocatalytic O_2 evolution, degradation of organic compounds, and molecular oxygen activation (Ye, et al., 2019). Following that, the conduction band of Bi_2WO_6 comprises W 5d and Bi 6p orbitals, while the valence band is composed of O 2p and Bi 6p orbitals with a minor contribution from Bi 6s hybrid orbitals (Orimolade, et al., 2021). The hybridization of O 2p and Bi 6s can facilitate the mobility of photogenerated holes in the widely dispersed valence band, leading to improved photocatalytic performance and high oxidation capability (Orimolade, et al., 2021).

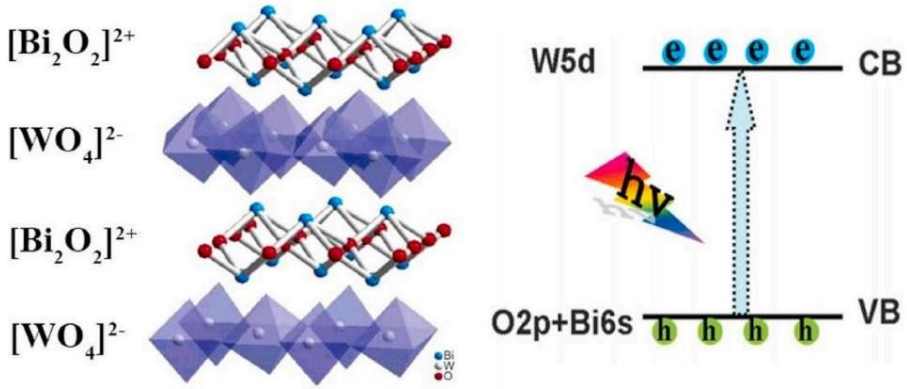

Figure 2.4: The Perovskite-like Composition and Band Structure of Bi_2WO_6 (Orimolade, et al., 2021).

The unique crystal and electronic structures of bismuth-based semiconductors make them a promising type of photocatalyst (Guo, et al., 2021). They have recently piqued the interest of many scholars due to their proper band gap and outstanding photocatalytic ability (Sin, et al., 2022). Bismuth-based semiconductors exhibit high oxidation capability in general, and have a narrow band gap of less than 3.0 eV, leading to enhanced absorption of visible light. This assertion is supported by Table 2.6, which shows that the majority of Bi-based photocatalysts have typical band gaps of less than 3.0 eV.

Table 2.6: Band Structures Data of Bi-Based Photocatalysts (Ye, et al., 2019).

Photocatalyst	E_g (eV)	E_{CB} (eV)	E_{VB} (eV)
BiOF	3.60	0.60	4.32

BiOCl	3.30	0.26	3.56
BiOBr	2.75	0.36	3.11
BiOI	1.94	0.47	2.41
Bi_3O_4Cl	2.83	0.16	2.99
$Bi_{12}O_{15}Cl_6$	2.98	0.16	3.14
$Bi_{12}O_{17}Cl_2$	2.60	0.20	2.80
$Bi_{24}O_{31}Cl_{10}$	2.90	0.17	3.07
Bi_3O_4Br	2.76	0.13	2.89
$Bi_4O_5Br_2$	2.82	0.15	2.97
$Bi_{12}O_{17}Br_2$	2.59	0.48	3.07
$Bi_{24}O_{31}Br_{10}$	2.79	0.14	2.93
$Bi_4O_5I_2$	2.08	0.39	2.47
Bi_5O_7I	2.61	0.12	2.73
$Bi_7O_9I_3$	2.25	0.30	2.55
Bi_2MoO_6	2.58	-0.31	1.87
Bi_2WO_6	2.90	-0.38	2.52
$BiPO_4$	4.31	-0.16	4.15
$BiVO_4$	2.30	0.39	2.69
$BiYO_3$	2.36	0.09	2.45
$BiFeO_3$	2.07	0.21	2.28
$Bi_2O_2CO_3$	2.90	0.41	3.31
$BiOIO_3$	3.13	0.97	4.10
Bi_2S_3	1.28	0.13	1.41
Bi_2O_3	2.71	0.13	2.84

Over the years, various synthesis methods have been used to fabricate Bi_2WO_6 with diverse microstructures and nanostructures such as nanoplates, nanorods, nanosheets, nanocuboids and nanoflowers. Hydro/solvothermal, calcination, electro-deposition, and the sol-gel process are some of the preparation methods that have been used. The synthesis technique has a large influence on the morphology of Bi_2WO_6, and varying photocatalytic capabilities are exhibited by different morphologies (Orimolade, et al., 2021). The appropriate synthesis pathway must be chosen when studying Bi_2WO_6 photocatalysis. Hence, hydro/solvothermal

method is widely adopted for Bi_2WO_6 synthesis due to its ability to control morphology during synthesis with ease (Orimolade, et al., 2021).

As previously mentioned, Bi_2WO_6 crystals are formed by the alternation of perovskite-like units $[WO_4]^{2-}$ and layers of $[Bi_2O_2]^{2+}$ (Orimolade, et al., 2021). During the hydrothermal reaction, the Bi^{3+} ion reacts with OH^- and H_2O to form the $[Bi_2O_2]^{2+}$ group, which then combines with the $[WO_4]^{2-}$ ion group to form Bi_2WO_6 nuclei. These nuclei act as seeds for the development of Bi_2WO_6 nanostructures, which occur in fluid regions that are supersaturated and are primarily governed by the mechanism of Ostwald ripening dissolution–crystallization (Cui, et al., 2016). Here are the relevant chemical reactions involved in the Bi_2WO_6 crystallization.

$$2Bi^{3+} + 4OH^- \rightarrow Bi_2O_2^{2+} + 2H_2O \quad (2.1)$$

$$2Bi^{3+} + 2H_2O \rightarrow Bi_2O_2^{2+} + 4H^+ \quad (2.2)$$

$$Bi_2O_2^{2+} + [WO_4]^{2-} \rightarrow Bi_2WO_6 \quad (2.3)$$

Table 2.7 provides a summary of the photocatalytic activity of Bi_2WO_6 on a variety of pollutants. For instance, Huang, et al. (2019) investigated the photocatalytic activities of the as-prepared Bi_2WO_6 samples and P25-TiO_2 under visible light irradiation by the degradation of norfloxacin (NOR) and enrofloxacin (ENR) at room temperature. All prepared Bi_2WO_6 samples demonstrated higher activity than P25-TiO_2. Under ideal conditions, the removal ratios of NOR and EOR by Bi_2WO_6 could reach 92.95 % and 94.58 %, respectively, in 75 min. This suggests that Bi_2WO_6 is a more efficient photocatalyst than P25-TiO_2, which only has a degradation efficiency of 20-30 %. A stability test on Bi_2WO_6 was also carried out, and the degradation efficiencies of NOR were determined to be 92.95 %, 84.74 %, 78.43 % and 80.71 %, respectively, for four successive cycles. Bi_2WO_6 photocatalyst with excellent reusability and stability can be effectively applied in practical settings. On the other hand, Li, et al. (2017) investigated the photocatalytic activities of Bi_2WO_6 by the photoreduction of Cr(VI) at room temperature under visible light irradiation. Different reaction conditions were compared, and the results showed a 41.9 % Cr(VI) reduction rate can be achieved after 100 min of irradiation with the addition of suitable amount of HCA and $NaHCO_3$. In essence, the higher separation

and transfer efficiency of photogenerated charge carries resulted in the high photoreduction efficiency of Bi_2WO_6.

Next, Gao, et al. (2011) investigated the photocatalytic oxidative desulfurization using Bi_2WO_6, a model compound (octane with dissolved thiophene), and an oxidant (H_2O_2). With a 2.5 g/L of catalyst dosage and a 10 % volume fraction of oxidant, the desulfurization rate of model compound reached 74.5 % after 2 hours of visible light illumination. The reaction was achieved by the simultaneous action of photochemical oxidation and photocatalytic oxidation. Hydroxyl free radicals are important in the free radical chain oxidation. Last but not least, several studies found that Bi_2WO_6 effectively degraded several organic dyes under simulated light, including 98.9 % of Rhodamine B (RhB) (Cui, et al., 2016), 99.2 % of methylene blue (MB) (Zhang, et al., 2018) and 92.6 % of methyl orange (MO) (Zhang, 2017). Stability tests were performed, which indicated good stability and reusability. More surface active sites for the photocatalysis reaction could be provided by the hierarchical nanosheet-built flower-like Bi_2WO_6 microspheres. It has a distinct structure, a suitable band gap and band position, and the generation of oxygen vacancy defects, which causes charge carriers to transfer quickly and retard their recombination.

Table 2.7: Photocatalytic Activity of Bi_2WO_6 on Various Pollutants.

Pollutant	Synthesis method	Light source	Reaction condition		Degradation efficiency (%)	Reference
			Catalyst loading (g/L)	Initial concentration of pollutant		
Norfloxacin	Solvothermal	300 W Xenon arc lamp	0.5	10 mg/L	92.95 (75 min)	(Huang, et al., 2019)
Enrofloxacin					94.58 (75 min)	
Chromium (VI)	Hydrothermal	200 W Xe lamp	1.0	50 mg/L	41.9 (100 min)	(Li, e al., 2017)
Rhodamine B	Hydrothermal	200 W Xe lamp	1.0	2 mg/L	98.9 (120 min)	(Cui, et al., 2016)
Sulphur	Hydrothermal	400 W halide lamp	2.5	100 %	74.5 (120 min)	(Gao, et al., 2011)
Methylene blue	Hydrothermal	300 W Xe lamp	1.0	5 mg/L	99.2 (150 min)	(Zhang, et al., 2018)
Methyl orange	Hydrothermal	Simulated light	1.0	10 mg/L	92.6 (150 min)	(Zhang, 2017)

2.6 Mechanism of Bi_2WO_6 Photocatalysis

To explain the phenomenon of heterogeneous photocatalysis, it is generally accepted that semiconductors can create charge carriers under light exposure, which can generate free radicals and initiate reactions leading to the production of CO_2 and H_2O (Ahmed and Haider, 2018). In general, four primary processes are involved during Bi_2WO_6 photocatalysis: charge carrier generation, trapping, recombination, and transfer.

Charge carrier generation

When Bi_2WO_6 is subjected to solar irradiation with photons (hv) that are equivalent to or greater than its band gap energy (E_g), excitation occurs. This leads to the promotion of electrons (e^-) in the filled valence band (VB) to a vacant conduction band (CB), leaving holes in the unfilled VB, and ultimately producing photo-induced electron-hole pairs (e_{CB}^- and h_{VB}^+) (Nunes, et al., 2021). Eq. (2.4) depicts the reaction.

$$Bi_2WO_6 + hv \rightarrow e_{CB}^- + h_{VB}^+ \tag{2.4}$$

where

h = Planck's constant

v = frequency of incident light

Charge carrier trapping

The photo-generated electron-hole pairs can be trapped in bulk or on the surface for further redox reactions. The carriers are attracted to the trapping sites by a weak van der Waal force (Thongam and Chaturvedi, 2021). Generally, surface trapping is preferred at either the subsurface or the surface region in semiconductor. During the trapping stage, the primary states for charge carriers are the temporal species such as trapped holes, trapped electrons, and free electrons. The trapped carriers tend to accumulate at the surface of particle, while free electrons are dispersed throughout the bulk. When compared to the charge carrier generation process, charge trapping is a slow step. (Qian, et al., 2018)

$$e_{CB}^- \rightarrow e_{tr}^- \tag{2.5}$$

$$h_{VB}^{+} \rightarrow h_{tr}^{+} \quad (2.6)$$

Charge carrier recombination

According to Qian, et al. (2018), spontaneous recombination of a considerable amount of the photo-induced e^{-}/h^{+} pairs can occur directly or at the trapping sites positioned on the surface of Bi_2WO_6 or in the bulk, with energy released in the form of light or heat, as shown in Eq. (2.7). This occurs most commonly at defect sites such as interstitial atoms, vacancies, and grain boundaries. Recombination can be slowed down via trapping of charge carriers when the trap depth is not too deep. Furthermore, eliminating crystal defects is thought to be effective in hindering charge recombination and improving photocatalytic activity.

$$e^{-} + h^{+} \rightarrow heat \; / \; hv \quad (2.7)$$

Interfacial charge transfer

After charge carrier separation without combining, the valence band holes and conduction band electrons can proceed to initiate the redox reaction. Only the surface of Bi_2WO_6 is involved in the photocatalytic reaction, which consists of two halves: (1) an electron-induced reduction reaction and (2) a hole-induced oxidation reaction. In the half reaction (2), the positive holes in VB react with adsorbed water (H_2O) or hydroxide ions (OH^{-}) to form powerful hydroxyl radicals ($\bullet OH$) via oxidation reaction (Eqs. (2.8) and (2.9)). Meanwhile, in the half reaction (1), the electrons in CB reduce the dissolved oxygen species to superoxide radicals ($O_2\bullet^{-}$). Protonation and reduction of $O_2\bullet^{-}$ radicals in acidic medium will produce hydroperoxyl radicals ($HO_2\bullet$) and subsequent hydrogen peroxide (H_2O_2) (Eqs. (2.10) to (2.13)). The H_2O_2 will undergo a series of reactions with e^{-} and $O_2\bullet^{-}$ radicals to produce hydroxyl radicals, which mineralize the adsorbed pollutants on the surface of Bi_2WO_6 into green chemicals such as CO_2, H_2O, and mineral acids (Eqs. (2.14) to (2.17)). No secondary pollution exists. (Qian, et al., 2018; Nunes, et al., 2021; Thongam and Chaturvedi, 2021)

$$H_2O + h^{+} \rightarrow H^{+} + \bullet OH \quad (2.8)$$

$$OH^{-} + h^{+} \rightarrow \bullet OH \quad (2.9)$$

$$O_2 + e^{-} \rightarrow O_2\bullet^{-} \quad (2.10)$$

$$O_2\bullet^- + H^+ \rightarrow HO_2\bullet \quad (2.11)$$

$$O_2\bullet^- + e^- + 2H^+ \rightarrow H_2O_2 \quad (2.12)$$

$$HO_2\bullet + HO_2\bullet \rightarrow H_2O_2 + O_2 \quad (2.13)$$

$$H_2O_2 + e^- \rightarrow \bullet OH + OH^- \quad (2.14)$$

$$H_2O_2 + O_2\bullet^- \rightarrow \bullet OH + OH^- + O_2 \quad (2.15)$$

$$H_2O_2 + hv \rightarrow 2\bullet OH \quad (2.16)$$

$$Organic\ pollutant + \bullet OH / O_2\bullet^- / OH^- / HO_2\bullet / H_2O_2 \rightarrow CO_2 + H_2O \quad (2.17)$$

Ahmed and Haider (2018) provided a summary of the overall process of heterogeneous photocatalysis which involves the following steps:

1. Transfer of organic pollutants or bacteria from the bulk liquid phase to the surface of the photocatalyst.
2. Photon-activated activation of pollutant adsorption on the photocatalyst surface.
3. Generation of radicals leading to the chemical degradation of contaminants.
4. Desorption of intermediate or final products from the photocatalyst surface.
5. Transfer of intermediate or final products back into the bulk liquid phase.

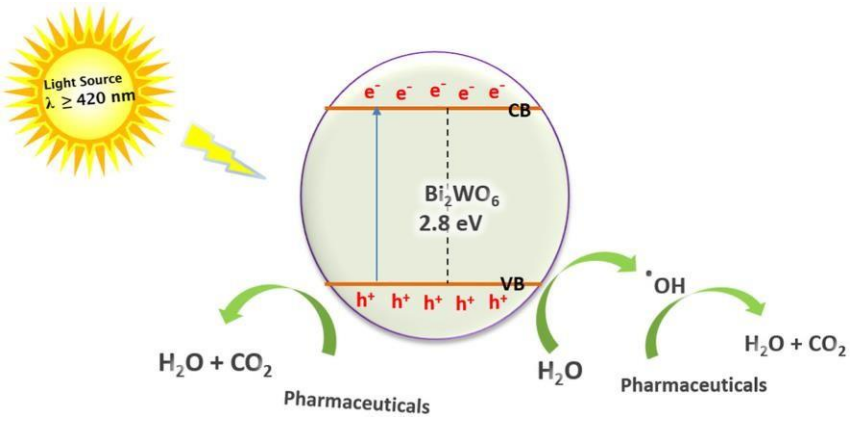

Figure 2.5: Photodegradation of Organic Pollutant by Bi_2WO_6 (Orimolade, et al., 2021).

2.7 Modification of Bi_2WO_6

Despite the fact that Bi_2WO_6 is a low-cost and environmentally friendly photocatalyst with potentially high photocatalytic properties, it has a few limitations that prevent it from performing efficiently. Bi_2WO_6 is a semiconductor with direct band gap that exhibits a certain response under visible light, but there is high probability for the photogenerated electrons and holes to recombine in the bulk phase owing to its small specific surface area, resulting in low photon quantum efficiency (Xu, et al., 2022). Furthermore, despite having high VB which enables its strong photo-oxidation performance in decomposing organic contaminants, Bi_2WO_6's relatively positive CB has resulted in its poor reduction ability (Zhang, et al., 2019). Recent emphasis has been placed on optimizing solar energy conversion efficiency through a variety of strategies to overcome those limitations (Tan, Abdi and Ng, 2019). This includes modifying the semiconductor through techniques such as doping, composite structure, metal/co-catalyst loading, and morphological control (Tan, Abdi and Ng, 2019). Among them, implementing narrow band-gap semiconductor coupling with Bi_2WO_6 to fabricate heterojunction interfaces has proven to be a relatively effective approach in the field of photocatalysis.

Heterojunctions are classified into two types: traditional (type-I and type-II) and Z-scheme. According to Guo, et al. (2021), traditional heterojunctions face a challenge of maintaining the efficient charge separation and strong redox capacities simultaneously because of the migration of electrons and holes towards more positive (lower) conduction band and more negative (higher) valence band potentials. Therefore, Z-scheme construction is introduced to address these issues. In a Z-scheme photocatalysis, the photogenerated electrons in one photocatalyst's less negative CB recombine with photogenerated holes in another photocatalyst's less positive VB (Sin, et al., 2021). This recombination results in the efficient separation of high-reductive photogenerated electrons and high-oxidative photogenerated holes for the subsequent photocatalytic reaction (Zhang, Zeng and Zhang, 2020). This special vector electron transfer ensures efficient charge separation and prudent use of redox capability by preserving the strong potential bands (Guo, et al., 2021). As a result, building a Z-scheme heterojunction can significantly improve the photocatalytic activity of Bi_2WO_6.

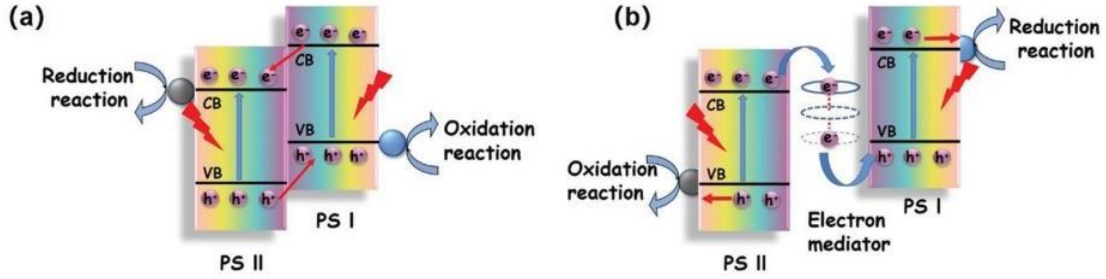

Figure 2.6: Schematic Illustration of (a) Type-II Heterojunction Photocatalyst and (b) Z-Scheme Junction Photocatalyst (Guo, et al., 2021).

Tin (IV) sulphide (SnS_2) is a small band-gap material (2.2 - 2.4 eV) that absorbs visible light efficiently and could be a promising candidate for metal-sulphide-metal-oxide heterojunction based photocatalysts (Kumar, et al., 2022). It is a member of the transition metal dichalcogenides family. The structure of SnS_2 is CdI_2-type layered, with the chalcogenide anions hexagonally packed between octahedrally coordinated Sn cations (Burton, et al., 2016). The VB primarily comprises S 3p and Sn 5S orbitals, while its CB is made up of Sn 5s and 5p orbitals (Burton, et al., 2016). These ultra-thin structures have a large surface area serving as the main driving force behind the increased activity (Burton, et al., 2016). Charges do not need to migrate to a surface in the 2D system before being available to the exterior medium, thus further enhancing their photocatalytic properties (Burton, et al., 2016). SnS_2 is abundant on Earth, low-cost, and less toxic. It has high electrical conductivity, good chemical and thermal stability, as well as the resistance to oxidation in both acidic and neutral solutions, making it being engrossed much consideration lately as a new type of photocatalyst for absorbing visible light for degrading pollutants (Xu, et al., 2022). Moreover, tailoring of morphologies such as nanoflowers, nanoplates, nanosheets, and nanotubes, can improve the characteristics of SnS_2 and enhance its photocatalytic properties (Kumar, et al., 2022).

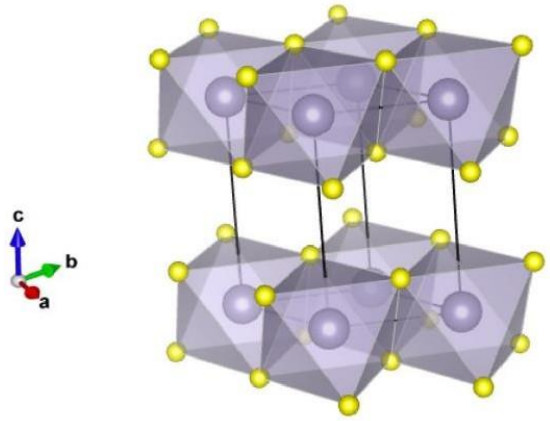

Figure 2.7: Ground State (2H) Structure of SnS_2 (Burton, et al., 2016).

The combination of SnS_2 and Bi_2WO_6 can enhance photocatalytic efficiency by effectively reducing the charge carrier recombination due to the matching energy band positions of the two materials, as per the theory of energy band matching (Xu, et al., 2022). Despite the fact that there have only been a few reports on coupling Bi_2WO_6 with SnS_2 to fabricate a visible light driven Z-scheme heterojunction photocatalyst, the statement above can be supported by the successful combination of SnS_2 with other bismuth-based semiconductors such as Bi_2S_3 (Gao, et al., 2016), $Bi_4Ti_3O_2$ (Das, et al., 2020), and BiOBr (Qiu, et al., 2017). According to their PL emission spectra, the emission peak drops significantly, indicating that the interfacial charge transfer between SnS_2 and the bismuth-based material significantly inhibits electron-hole recombination.

Table 2.8 displays the results of the photocatalytic activity of various Bi_2WO_6-based heterojunction photocatalysts on different types of pollutants. In a recent study, Bi, et al. (2021) synthesized a Z-scheme structured $Bi_2WO_6/ZnIn_2S_4$ composite via impregnation method, which demonstrated improved photocatalytic performance. In comparison to the pure Bi_2WO_6 and $ZnIn_2S_4$, which had the methyl orange (MO) degradation efficiencies of 8 % and 48.4 %, respectively, $Bi_2WO_6/ZnIn_2S_4$-2 exhibited a 97.5 % degradation efficiency within 60 min. The efficiency remained over 90 % after five reuses. The high photocatalytic activity was owing to the rapid transfer of carriers, which prevented the recombination of charge carriers. According to the photoluminescence (PL) emission spectra result, the lowest

photoluminescence intensity was observed in $Bi_2WO_6/ZnIn_2S_4$-2, demonstrating that the formation of heterojunction greatly promoted carrier separation and thus prolonged carrier lives. Meanwhile, the intensity of the strong photocurrent response of $Bi_2WO_6/ZnIn_2S_4$-2 was 11.7 times and 2.5 times that of pure Bi_2WO_6 and $ZnIn_2S_4$, respectively. On the other hand, a SnS/Bi_2WO_6 heterostructure was fabricated by Li, Meng and Zhang (2019) to degrade RhB. The photocatalytic degradation activity of SnS/Bi_2WO_6 composites containing 0.5 wt% SnS was found to be approximately 5.8 times greater than that of pure Bi_2WO_6. According to their findings, SnS was an excellent modifier with indirect band-gap transitions that, when combined with direct band-gap Bi_2WO_6, enhance the photocatalytic activity. The formation of a heterostructure between the surfaces of Bi_2WO_6 and SnS has a positive synergetic effect, which could facilitate the migration and separation of photogenerated charge carriers. Besides, high stability and reusability of SnS/Bi_2WO_6 composites were validated through the negligible difference between five RhB concentration profiles.

Zhang, et al. (2021) studied the photodegradation of RhB and *Pseudomonas aeruginosa* (*P.aeruginosa*) by a new MoS_2/Bi_2WO_6 (MB) Z-scheme heterostructure. As MoS_2 loading increased, tighter nanosheet accumulation was observed, resulting in the gradual evolution of flower-like microspheres with a higher surface area and nanosheets being more perpendicular at the concave's centre. The MB-9 composite exhibited excellent photocatalytic degradation efficiency, with complete RhB degradation achieved in 90 min, and almost all *P.aeruginosa* decomposed in 60 min, which the results were far superior to pure MoS_2 and pure Bi_2WO_6. During *P.aeruginosa* degradation, the active species continued to oxidize the cell fragments and leaked intracellular components into CO_2 and H_2O, presenting MB-9 composites as an eco-friendly photocatalyst for disinfection purposes. In short, the formation of heterostructures between MoS_2 and Bi_2WO_6, along with the synergistic effects of photoabsorption and photocatalysis, greatly enhanced the photocatalytic performances of MoS_2/Bi_2WO_6 heterojunctions.

Zhang, Zeng and Zhang (2020) found that the best photocatalytic performance for tetracycline was achieved using Bi_2WO_6/BiSI (170 ℃). Within 30 minutes, 93.01 % of the tetracycline can be degraded. This was attributed to the flake structure of the as-prepared catalyst at 170 ℃, which had a smaller and more uniform

size, resulting in a larger surface area. The heterojunction of Bi_2WO_6/BiSI (170 ℃) displayed better photocatalytic properties when compared to the monomer, mainly due to its unique heterostructure, which prevented electron and hole recombination. The cyclic tests demonstrated that the Bi_2WO_6/BiSI hybrid materials maintained stable degradation ability. On the other hand, Lu, et al. (2018) constructed a $CuInS_2/Bi_2WO_6$ composite to degrade the tetracycline hydrochloride (TC•HCl). The optimal Z-scheme 15 % $CuInS_2/Bi_2WO_6$ exhibited more than three times the photocatalytic activity of pure $CuInS_2$ and 17 % of Bi_2WO_6. The researchers attributed this to the intimate contact of interface, which ensured promising abilities of the interfacial charge transfer. According to the results, the PL intensity of 15 % $CuInS_2/Bi_2WO_6$ was the lowest of all samples, indicating that the addition of proper $CuInS_2$ was beneficial in slowing the charge carrier recombination. Furthermore, the researchers evaluated the effectiveness of 15 % $CuInS_2/Bi_2WO_6$ for removing COD in real pharmaceutical wastewater. Surprisingly, photocatalysis of a $CuInS_2/Bi_2WO_6$ heterojunction, aided by Fenton reaction, can remove 90.5 % of COD in wastewater efficiently.

Last but not least, Zhang and colleagues (2019) revealed that the 10 % bi-functional $AgIn_5S_8/Bi_2WO_6$ Z-scheme heterojunctions exhibited a reduction efficiency for Cr(VI) that was more than twice as much as that of pure Bi_2WO_6. Aside from the obvious reduction in band gaps with increasing $AgIn_5S_8$ content, the high charge separation and transfer efficiency of $AgIn_5S_8/Bi_2WO_6$ heterojunctions also contributed to the enhanced reduction efficiency. However, the result was lower than that of pure $AgIn_5S_8$, which could be attributed to carrier transfer path in the heterojunctions and the inverse oxidation of Cr(III) to Cr(VI) by hydroxyl radicals. In addition, $AgIn_5S_8/Bi_2WO_6$ was able to remove COD up to 77 %, indicating its great practical potential.

Table 2.8: Photocatalytic Activity of Bi_2WO_6-Based Heterojunction Photocatalyst on Various Pollutants.

Photocatalyst	Pollutant	Synthesis method	Light source	Reaction condition		Degradation efficiency (%)	Reference
				Catalyst loading (g/L)	Initial concentration of pollutant		
$Bi_2WO_6/ZnIn_2S_4$	Methyl Orange	Impregnation	300 W visible light	0.2	10 mg/L	97.5 (60 min)	(Bi, et al., 2021)
SnS/Bi_2WO_6	Rhodamine B	Bath sonication	300 W halogen tungsten lamp	1	10 mg/L	100 (60 min)	(Li, Meng and Zhang, 2019)
MoS_2/Bi_2WO_6	Rhodamine B	Hydrothermal	500 W Xe lamp	1	10^{-5} M	100 (90 min)	(Zhang, et al., 2021)
	Pseudomonas aeruginosa			1	2.0 x 10^8 cfu/mL	99.99 (60 min)	
Bi_2WO_6/BiSI	Tetracycline	Hydrothermal	High pressure mercury lamp	0.4	20 mg/L	93.01 (30 min)	(Zhang, Zeng and Zhang, 2020)
$CuInS_2/Bi_2WO_6$	Tetracycline hydrochloride	Hydrothermal	300 W Xe lamp	0.3	10 mg/L	92.4 (120 min)	(Lu, et al., 2018)
$AgIn_5S_8/Bi_2WO_6$	Chromium (VI)	Solvothermal	PLS-SXE300 Xe lamp	0.3	100 %	64 (120 min)	(Zhang, et al., 2019)

2.8 Synthesis of Bi_2WO_6–based Composites via Deposition Method

Combining an n-type Bi_2WO_6 semiconductor with a p-type semiconductor is considered a viable solution for improving the potential photocatalytic applications of Bi_2WO_6. In order to obtain materials with the desired physical and chemical properties, the fabrication process of Bi_2WO_6-based composites has become an important step in research and development activities. Currently, various coupling methods for Bi_2WO_6-based composites have been reported, such as ion exchange (Xu, et al., 2019), deposition-precipitation (Phuruangrat, et al., 2018), sol-gel (Guo, Zhang and Gan, 2012), hydrothermal (Arya, et al., 2020), electro-spinning (Zhao, et al., 2013), and so on. Among these, deposition method is preferred due to its numerous advantages: (1) mild reaction conditions, (2) technical simplicity with no post-treatment required, and (3) stable, cost-effective, and low environmental pollution.

For instance, Li, Cui and Hong (2013) used a room temperature deposition approach to create a BiOI/Bi_2WO_6 heterostructure. Typically, a clear solution A was first produced by dissolving different stoichiometric quantities of $Bi(NO_3)_3 \cdot 5H_2O$ and 30 mg KI in 20 mL ethylene glycol. Then, a homogeneous mixture B was produced by dispersing 1 g of the as-prepared hydrothermal-synthesized Bi_2WO_6 in deionized water. which was then mix with solution A while being vigorously swirled. After an additional 5 h of agitation at room temperature, the products were centrifuged, rinsed with absolute ethanol and deionized water, and dried at 80 ℃ in air. The successful synthesis of the heterostructure was confirmed by HRTEM analysis, with the clear fringe indexed to the lattice plane of tetragonal BiOI agreeing with that of orthohombic Bi_2WO_6. When compared to pure Bi_2WO_6, the heterostructure demonstrated excellent photocatalytic performance in the aqueous degradation of Reactive Brilliant Red (X-3B). Sensitization of BiOI in the Bi_2WO_6 increased photogenerated charge carrier separation, according to the PL emission spectra results, which prolonged carrier lifetime and improved the interfacial charge transfer effectiveness to the adsorbed substrates, hence boosting photocatalytic activity.

On the other hand, Phuruangrat, et al. (2018) successfully fabricated an efficient heterostructure AgI/Bi_2WO_6 nanocomposite using a simple precipitation-deposition process. With 24-h stirring, 0–10 wt% $AgNO_3$ and NaI, as well as 1 g of the as-prepared hydrothermal-synthesized Bi_2WO_6, were dissolved in 100 mL RO water. The products were separated, rinsed with water and ethanol, and dried for 24 h at 80 °C. The SEM image of AgI/Bi_2WO_6 nanocomposite indicated that the composite was successfully prepared because the nanocomposite remained as nanoplates of Bi_2WO_6 with numerous little broken parts. The nanospheres of AgI were supported at random on Bi_2WO_6 nanoplates. Then, the suppressed efficiency of photogenerated carrier recombination in AgI/Bi_2WO_6 nanocomposite was significantly higher than that of pristine Bi_2WO_6. Hence, their composite demonstrated significant catalytic activity for RhB photodegradation. As reported, nearly 100 % of RhB was degraded by the hybrid materials within 80 min, which was approximately 1.53 times that of pure Bi_2WO_6.

Last but not least, Qu, et al. (2020) reported an intimate Fe_2O_3/Bi_2WO_6 heterojunction formed by mechanical mixing the as-prepared hydrothermally synthesized Bi_2WO_6 with an amount of Fe_2O_3. Efficient separation of charge carriers and significant enhancement in the visible-light photocatalytic performance can be assured by the intimate interface contact. More agreement could be obtained from their doxycycline (Dox) degradation results. Bi_2WO_6-Fe_2O_3/H_2O_2 exhibited higher photocatalytic productivity to degrade Dox than Bi_2WO_6/H_2O_2. H_2O_2 reacted with photogenerated electrons to produce •*OH*. The heterogeneous Fenton reaction between Fe_2O_3 and H_2O_2 on its surface, as well as the coupling effect occuring at the composite's interfaces, may be responsible for the quantity of •*OH* produced. As a result, higher •*OH* production was in Fe_2O_3/Bi_2WO_6 as compared to pure Bi_2WO_6.

2.9 Phytotoxicity

Phytotoxicity assessments have been widely used to verify the toxicity of various substances and compounds in the environment. This process involves measuring the impact of specific substances on plant growth, seed germination, or any negative influences on plants (Pérez-Portuondo, et al., 2021). The analysis is performed prior to the emission of toxic compounds in order to purify and eliminate any negative environmental impacts, and is followed by reused applications such as irrigation. The phytotoxicity test is simple to perform and cost-effective, and the toxicological assays are precise with sensitive and reliable results (Mendes, et al., 2021). Despite the inability to identify the elements that confer the specific toxic properties, the phytotoxicity test allows for a comparison of toxicity levels between studied compounds (Mendes, et al., 2021). It identifies any substance that causes temporary or permanent stress on seed germination, dry matter evolution, and root growth (Pérez-Portuondo, et al., 2021). The test is typically performed based on germination rate, root elongation, biomass weight, and other factors. As the primary part of a plant is affected by toxicant accumulation, a decrease in root length may indicate the presence of toxicants in the water bodies or soil (Kee et al., 2021).

Chin, et al. (2018) performed the phytotoxicity measurements of palm oil mill effluent (POME) photocatalytically treated with ZnO/Nb_2O_5-3 composites using the *Vigna radiata*. The radicle length of the seeds was used to compute the reduction in phytotoxicity, which was based on Eq. (2.18):

$$\%\ phytotoxicity = \left(\frac{radicle\ length\ of\ control - radicle\ length\ of\ sample}{radicle\ length\ of\ control}\right) x\ 100 \quad (2.18)$$

Results showed that the phytotoxicity of POME, which was initially 84.7 %, was reduced to 58.6 %. Meanwhile, the average radicle lengths of *Vigna radiata* seeds cultured in POME samples before and after photocatalytic treatment were 2.1 and 5.6 cm, respectively. Hence, the radicle growth from seed germination revealed the photocatalytic efficiency of ZnO/Nb_2O_5-3 in promoting the reusability of treated water.

Rouibah, et al. (2021) used the germination of Cresson seeds to assess the toxicity of TiO_2/cellulose and ZnO/polystyrene treated samples in the presence of oxidants (H_2O_2 and $K_2S_2O_8$). The results of germination index (GI), shoot length, and number of seeds were measured after 4 days. GI value was calculated according to the following relations:

$$GI(\%) = \frac{Seed\ germination\ (\%)\ x\ root\ length\ of\ treatment}{Seed\ germination\ (\%)\ x\ root\ length\ of\ control}\ x\ 100 \qquad (2.19)$$

There are three categories of toxicity based on GI value:

- GI < 50 % indicates high phytotoxicity
- 50 % < GI < 80 % represents moderate phytotoxicity
- GI > 80 % implies an absence of phytotoxicity

According to the findings, the untreated sample has a lower percentage of seed germination (43 %). For TiO_2/cellulose, photocatalytic treatments with the catalyst in the presence of H_2O_2 (GI = 80.1 %) and $K_2S_2O_8$ (GI = 91.1 %) resulted in non-toxic degradation by-products. Meanwhile, treatment with ZnO/polystyrene in the presence of $K_2S_2O_8$ resulted in moderate toxicity with a GI value of 68.1 %. Despite being more than 93 % effective, only moderate phytotoxicity was achieved, most likely due to photodissolution of Zn during treatment, which increased toxicity. Thus, it was proposed that pollutant metabolites produced during photocatalytic treatments in the presence of TiO_2-$K_2S_2O_8$/cellulose and TiO_2-H_2O_2/cellulose are not toxic to seeds. This indicated that the treated water could be reused and these treatments could be used to reduce the phytotoxicity of drug solutions.

Gordillo-Delgado, Zuluaga-Acosta and Restrepo-Guerrero (2020) conducted the phytotoxicity assessment on the titanium dioxide (TiO_2) using spinach seeds named *Spinacia oleracea*. Two simple parameters for easy observation, Average Germination Time (AGT) and Germination Rate (GR), were evaluated. The results were analysed using multifactorial Analysis of Variance (ANOVA). The respective equations were as follows:

$$AGT = \frac{\sum FX}{\sum F} \qquad (2.20)$$

$$GR = \left(\frac{a}{1}\right) + \left(\frac{b-a}{2}\right) + \left(\frac{c-b}{3}\right) + \cdots + \left(n - \left(\frac{n-1}{n}\right)\right) \quad (2.21)$$

where

F = number of seeds germinated at time X in days since inoculation

a, b, c, …, n = number of seeds that germinated after 1, 2, 3, …, N days from the beginning of inoculation

Based on the P-values obtained from ANOVA, 95 % confidence level was achieved. The findings indicated that particle size and concentration had a direct effect on seed germination, with smaller TiO_2 particle sizes and lower concentrations resulting in a decrease in AGT and an increase in GR. Conversely, larger particle sizes and higher concentrations led to an increase in AGT and a decrease in GR. Treatment with nanometric size TiO_2 improved the seeds' resistance to stress and facilitated water and oxygen absorption, which accelerated germination. This was attributed to the generation of ROS.

Golami, et al. (2019) investigated the toxicity of gemifloxacin (GMF) treated with zinc oxide-biochar (ZnO-BC) composite using *Lemna minor*. GMF solution, treated GMF solution, and water were selected as testing solutions. The Relative Frond Number (RFN) was computed using Eq. (2.22).

$$RFN = \frac{(Frond\ N_{10} - Frond\ N_0)}{Frond\ N_0} \quad (2.22)$$

where

N_0 = frond number at the beginning day

N_{10} = frond number after 10 days

The greater the toxicity, the lower the pigment contents due to plant death. Results showed that the RFNs for water, treated GMF solution, and untreated GMF solution were 1.44, 1.24, and 0.16, respectively. The untreated GMF solution was the most toxic of all the samples, as evidenced by its lowest pigment contents. After treatment with ZnO-BC, the GMF was degraded and the pigment contents increased

significantly. Therefore, ZnO-BC demonstrated its ability to produce low toxic by-products and products.

2.10 Summary of Literature Review

Water pollution is a critical environmental problem in Malaysia. Contaminants such as organic pollutants (RhB) and heavy metals (Cr(VI)) should be removed from the water bodies to avoid their harmful effect on living organisms. Recent approach is on the heterogeneous photocatalysis employing semiconductor because it is a clean environmental remediation method for removing contaminants from water. Coupling Bi_2WO_6 with another semiconductor to form a Z-scheme heterostructure not only improves the physical and chemical properties of single material, but also enhances its photocatalytic activity. Despite the fact that Bi_2WO_6-based photocatalysis has been extensively studied for pollutant degradation and heavy metal reduction, only few studies have attempted to construct heterojunction composites by coupling Bi_2WO_6 with SnS_2. In this regard, the coupling technique via a hydrothermal-deposition method has been evaluated to determine its feasibility. In previous literature, UV and Xenon lamps were used as light sources for photocatalysis of environmental contaminants. However, only a small amount of research has been done on Bi_2WO_6-based photocatalysis under solar light irradiation for the simultaneous organic pollutants degradation and heavy metals reduction. In fact, sunlight-assisted photocatalysis is desirable in terms of practical application due to Malaysia's strategic location near the equator, which receives daylight all year.

CHAPTER 3

METHODOLOGY

3.1 Overall Experimental Flowchart

Figure 3.1 depicts the overall research study flowchart.

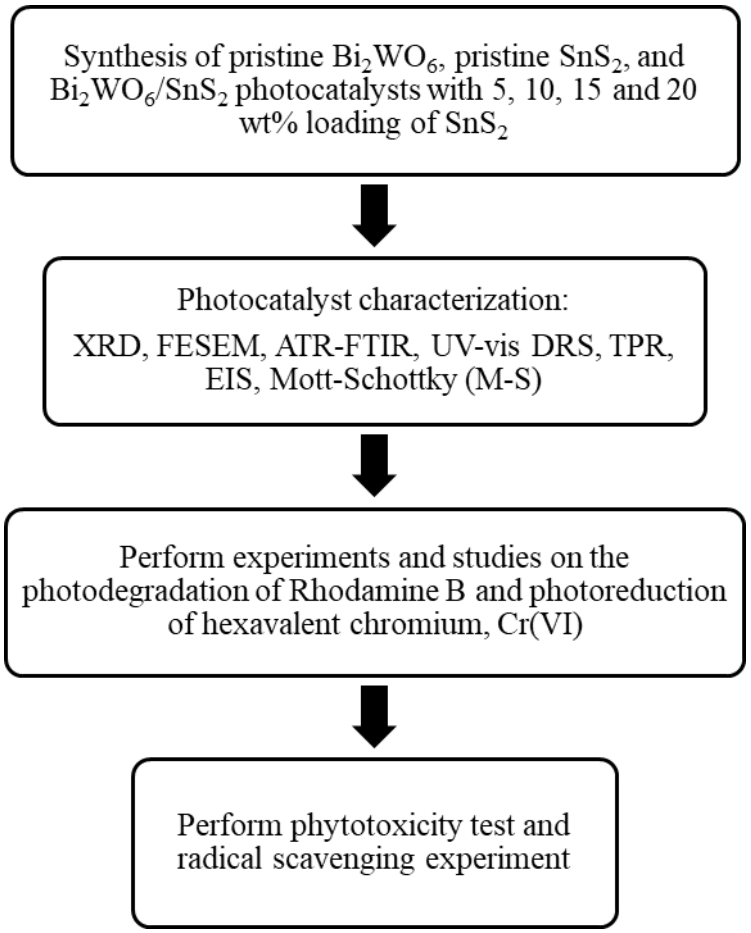

Figure 3.1: Overall Experiment Flowchart.

3.2 Materials and Chemicals

Table 3.1 presents the materials and chemicals employed in the present study.

Table 3.1: List of Material and Chemical Used.

Material/Chemical	Purity (%)	Supplier/Source	Application
Bismuth nitrate pentahydrate [$Bi(NO_3)_3 \cdot 5H_2O$]	98.0	R&M Chemicals	Bismuth precursor
Sodium tungstate dihydrate [$Na_2WO_4 \cdot 2H_2O$]	98.0	R&M Chemicals	Tungsten precursor
Tin(IV) chloride pentahydrate [$SnCl_4 \cdot 5H_2O$]	98.0	HiMedia Laboratories	Tin precursor
Thioacetamide [C_2H_5NS]	99.0	Shanghai Zhanyun Chemical	Sulphur precursor
Nitric acid [HNO_3]	65.0	R&M Chemicals	Solvent used in fabrication of photocatalyst; pH adjustor
Rhodamine B [$C_{28}H_{31}ClN_2O_3$]	90.0	Merck Millipore	Model pollutant for photodegradation of organic pollutant
Potassium dichromate [$K_2Cr_2O_7$]	99.9	R&M Chemicals	Model pollutant for photoreduction of heavy metal

Sulphuric acid [H_2SO_4]	98.0	QRec	Photocatalytic activity test for Cr^{6+} ions
1,5-diphenylcarbazide [$C_{13}H_{14}N_4O$]	98.0	R&M Chemicals	Photocatalytic activity test for Cr^{6+} ions
Acetone [CH_3COCH_3]	99.0	Bendosen	Photocatalytic activity test for Cr^{6+} ions
Ethanol [C_2H_5OH]	99.8	ChemSoln	Solvent used in fabrication of photocatalys; radical scavenger
Distilled water [H_2O]	-	Gainson Advanced Technology	Solvent used in fabrication of photocatalyst
Sodium hypochlorite [NaOCl]	11 % Cl	Progressive Scientific	Solvent used to sterilize green bean for phytotoxicity test
Sodium sulphate [Na_2SO_4]	99.8	Bendosen	Radical scavenger; Medium for photoelectrochemical test
Ethylenediaminetetraacetic acid [$C_{10}H_{16}N_2O_8$]	99.0	Systerm Chemicals	Radical scavenger
Benzoquinone [$C_6H_4O_2$]	98.0	Acros Organics	Radical scavenger

3.3 Preparation of Photocatalyst

To synthesize pristine Bi_2WO_6, 1.9403 g of $Bi(NO_3)_3 \cdot 5H_2O$ (0.004 mol) was dissolved into 120 mL 0.4 M HNO_3 to form solution A, which was then ultrasonicated for 10 min until dissolved completely. Meanwhile, 0.6597 g of $Na_2WO_4 \cdot 2H_2O$ (0.002 mol) was fully dissolved into 40 mL distilled water to form solution B. The solution B was slowly added drop wise into the solution A under continuous stirring at 500 rpm for 1 h, producing a white suspension. The mixture was transferred into a 200 mL Teflon-lined stainless steel autoclave and subjected to heat at 175 ℃ for 16 h. Subsequently, the autoclave was allowed to cool to room temperature. The pale yellow precipitates were filtered, washed with distilled water and ethanol for several times, and dried in an oven at 60 ℃ overnight before finely ground. The preparation process of Bi_2WO_6 is illustrated in Figure 3.2.

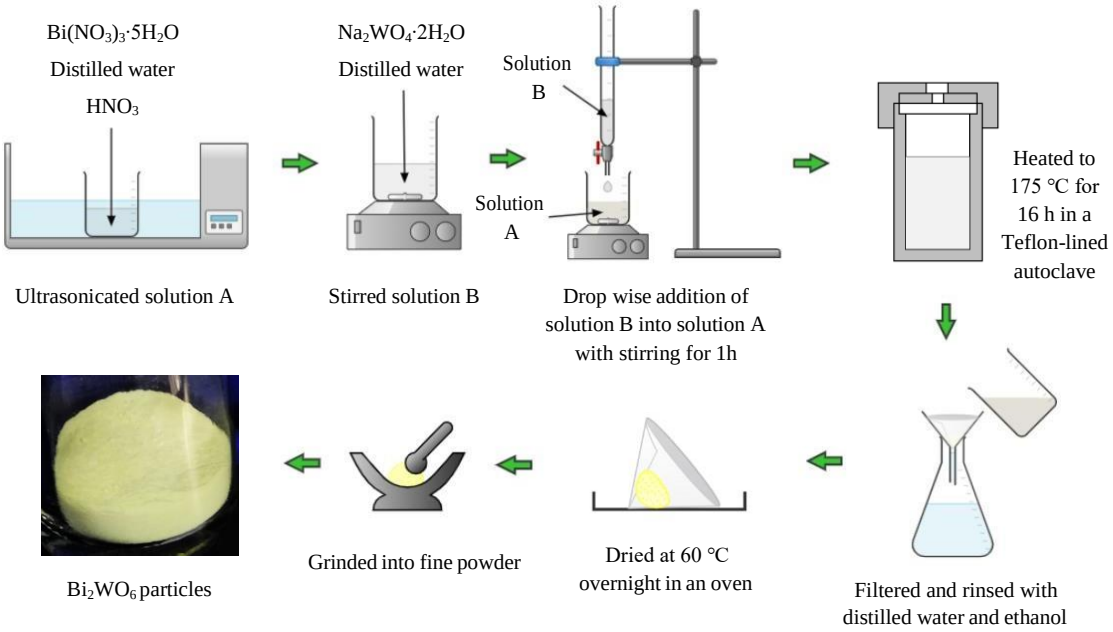

Figure 3.2: Synthesis of Bi_2WO_6 Particles.

To prepare pristine SnS_2, 4.0073 g of $SnCl_4 \cdot 5H_2O$ (11.43 mmol) was dissolved into 160 mL distilled water. Subsequently, 2.5763 g of C_2H_5NS (34.29 mmol) was slowly added into the solution, followed by continuous stirring for 1 h until dissolved. The resulting mixture was transferred into a 200 mL Teflon-lined

stainless-steel autoclave and subjected to heat at 180 ℃ for 10 h. After that, the autoclave was slowly brought to room temperature. The brown precipitates were filtered and washed several times with distilled water and ethanol. Finally, the collected sample was dried in an oven at 60 ℃ overnight, and finely ground. The preparation process of SnS_2 is illustrated in Figure 3.3.

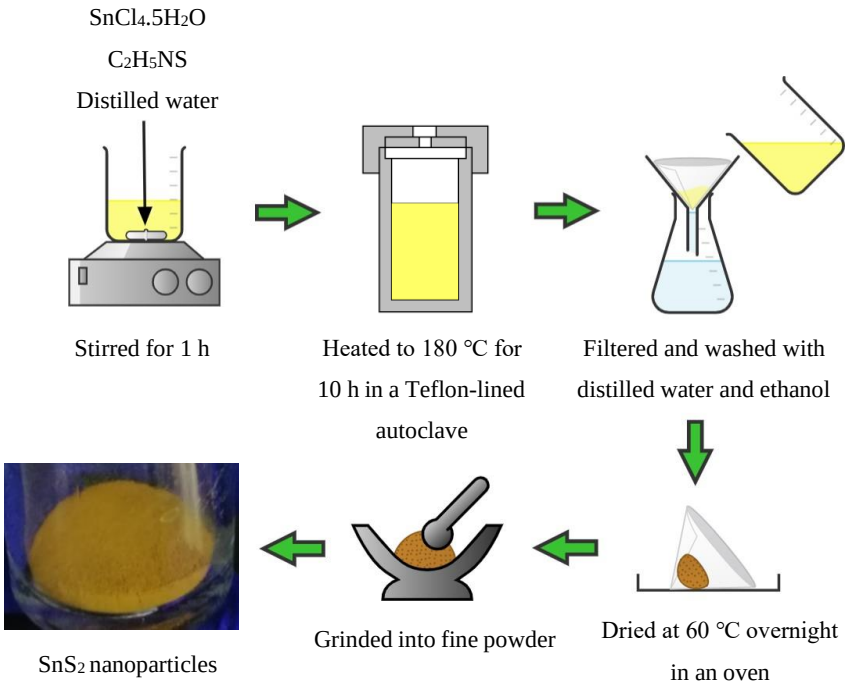

Figure 3.3: Synthesis of SnS_2 Nanoparticles.

To synthesize Bi_2WO_6/SnS_2 composites, 0.5 g of Bi_2WO_6 and 0.02632 g of SnS_2 were added into 50 mL distilled water. The mixture was magnetically stirred overnight to ensure homogeneity. The as-formed precipitates were filtered and washed with distilled water. The collected sample was dried in an oven at 60 ℃ overnight, and grinded into fine powder. This composite was designated as Bi_2WO_6/SnS_2-5. Overall, the loading of SnS_2 was varied to prepare Bi_2WO_6/SnS_2-x, in which x represents the weight percentage of SnS_2 (x = 5, 10, 15 and 20 wt%). The fabrication of Bi_2WO_6/SnS_2 is illustrated schematically in Figure 3.4.

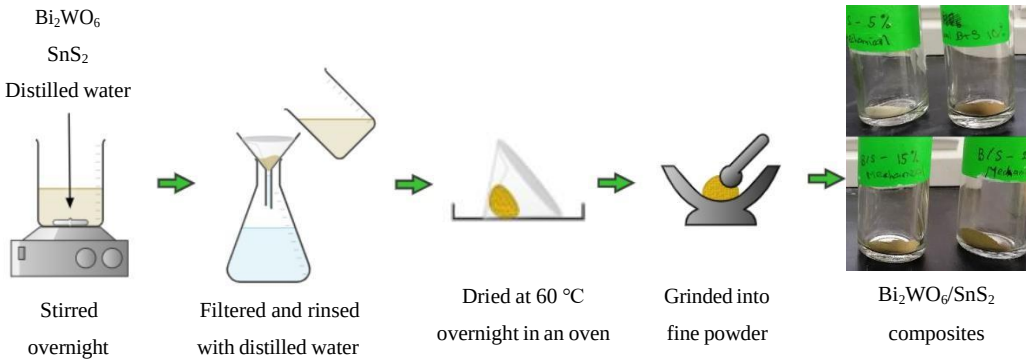

Figure 3.4: Synthesis of Bi_2WO_6/SnS_2 Composites.

3.4 Characterization

3.4.1 X-ray Diffraction (XRD)

The crystallographic structure of Bi_2WO_6/SnS_2 was investigated using a Smimadzu XRD-6000 machine at Faculty of Science, UTAR Kampar. The characteristic X-ray spectra was produced when the electrons have sufficient energy to displace inner shell electrons of the sample. A detector detected the X-ray signal and formed peaks of varying intensities at different positions. The XRD data were scanned over 2θ ranging from 10º to 90º.

3.4.2 Attenuated Total Reflectance - Fourier Transform Infrared Spectroscopy (ATR-FTIR)

Attenuated Total Reflectance – Fourier Transform Infrared Spectroscopy (ATR-FTIR) was used to determine the functional groups in Bi_2WO_6/SnS_2 samples. The analysis was carried out using the Perkin Elmer Spectrum Two Universal ATR at Faculty of Science, UTAR Kampar. The ATR-FTIR data were scanned over the infrared wavelengths ranging from 4000 cm^{-1} to 400 cm^{-1}, and the amount of beam and frequencies at which the sample absorbed the infrared radiation were measured.

3.4.3 Ultraviolet-visible Diffuse Reflectance Spectroscopy (UV-vis DRS)

The Ultraviolet-visible Diffuse Reflectance Spectroscopy (UV-vis DRS) analysis was conducted to determine the optical properties of the as-synthesized photocatalyst samples and to evaluate their band gap energy. This analysis involved the use of JASCO V-730 UV-vis spectrophotometer available at Faculty of Engineering and Green Technology, UTAR Kampar.

3.4.4 Transient Photocurrent Response (TPR), Electrochemical Impedance Spectroscopy (EIS) and Mott-Schottky (M-S)

The photoelectrochemical properties of the Bi_2WO_6/SnS_2 photocatalysts were measured via a Gamry Interface 1000 electrochemical workstation available at Faculty of Science, UTAR Kampar. Transient photocurrent response analysis was used to assess the ability of a photocatalyst to suppress the recombination of charge carriers. Meanwhile, an EIS investigation was performed to support the transient photocurrent response measurements, which examined the charge carrier separation and interfacial charge transfer. Whereas the Mott-Schottky (M-S) plot examined the band alignment of the samples.

3.5 Photoactivity Test

The photocatalytic performances of Bi_2WO_6/SnS_2 samples were evaluated by the photodegradation of Rhodamine B and photoreduction of Cr(VI). To photodegrade the Rhodamine B, the suspension was put in the dark under constant magnetic stirring for 1 h with the initial volume of 200 mL and initial concentration of 10 mg/L, in which the dosage of photocatalyst was 0.2 g. The concentration of RhB after equilibration was analysed using JASCO V-730 UV-vis spectrophotometer at the wavelength of 553.5 nm and recorded as the initial concentration (C_o). After reaching the adsorption-desorption equilibrium, the suspension was subjected to constant stirring under sunlight irradiation for 3 h to examine the photocatalytic activity, as depicted in Figure 3.5. Throughout the experiment, 4 mL suspension was collected at every 20 min to measure the RhB concentration at the particular time (C_t).

Figure 3.5: Experimental Setup for Photodegradation of Rhodamine B.

On the other hand, the photocatalytic reduction of Cr(VI) was carried out by suspending 0.2 g of as-prepared photocatalyst in 200 mL $K_2Cr_2O_7$ aqueous solution with initial concentration of 10 mg/L. The suspension was put in the dark with constant stirring for 1 h to achieved adsorption-desorption equilibrium. Then, the experiment was conducted under sunlight irradiation for 3 h, as depicted in Figure 3.6. At every 20 min interval, about 4 mL of the aliquots was extracted for further analysis. The concentration of Cr(VI) was quantified via a diphenylcarbazide method using a JASCO V-730 UV-vis spectrophotometer at the wavelength of 542.5 nm. This specific test was conducted by mixing 1 mL of the collected suspension with 9

mL of 0.2 M H_2SO_4 and 0.2 mL of 2.5 g/L 1,5-diphenylcarbazide solution. The mixture was shake for 15 to 30 s and 4 mL solution was withdrawn for absorbance test.

Figure 3.6: Experimental Setup for Photoreduction of Cr(VI).

Simultaneous decomposition of RhB and Cr(VI) was conducted to further test the photocatalytic potential of as-fabricated samples. Typically, 0.2 g of sample was dispersed into 200 mL mixture solution composed of 10 mg/L RhB and 10 mg/L $K_2Cr_2O_7$. The pH for the reaction mixture was adjusted to the required level using 0.1 M HCl or NaOH solution if necessary. The mixture was stirred in dark for 1 h to reach adsorption-desorption equilibrium. Subsequently, photocatalytic test was conducted under sunlight irradiation for 3 h, which is as depicted in Figure 3.7. During the test, 4 mL suspension was withdrawn from the photoreaction solution at every 20 min interval. The concentrations of RhB and Cr(VI) in the solution were determined in the same way as that when they were decomposed individually.

Figure 3.7: Experimental Setup for Simultaneous RhB-Cr(VI) Degradation.

For the experiments, the photocatalytic efficiency was determined based on Eq. 3.1. The experimental data was fitted to a Langmuir Hinshelwood kinetic model, as shown in Eq. 3.2, and the apparent reaction rate constant, k_{app}, was computed from the gradient of the graph.

$$Photocatalytic\ efficiency\ (\%) = \frac{C_o - C_t}{C_o} \times 100\% \tag{3.1}$$

where

C_o = concentration of pollutant at time, t = 0 (mg/L)

C_t = concentration of pollutant at a given time, t (mg/L)

$$\ln\left(\frac{C_o}{C_t}\right) = k_{app}t \tag{3.2}$$

where

C_o = concentration of pollutant at time, t = 0 (mg/L)

C_t = concentration of pollutant at a given time, t (mg/L)

k_{app} = apparent reaction rate constant (min^{-1})

t = reaction time (min)

3.6 Phytotoxicity Test

Phytotoxicity assessment was conducted for the photocatalytically treated RhB-Cr(VI) mixture using commercially available mung bean seeds as a phytotoxicity assessment indicator. Initially, the surface of mung bean seeds was sterilized with 0.5% sodium hypochlorite and rinsed several times with distilled water. The sterilized seeds were then placed in three plastic containers with cotton wool that had been wet with distilled water (control) and RhB-Cr(VI) solution (untreated and treated). The seed growth was subsequently monitored for 7 consecutive days. After a duration of 7 days, the sprouted seeds were taken out from their containers and the

lengths of the radicles were measured. The phytotoxicity of each sample was calculated according to Eq. (3.3).

$$\%\ phytotoxicity = \left(\frac{radicle\ length\ of\ control - radicle\ length\ of\ sample}{radicle\ length\ of\ control}\right) x\ 100 \quad (3.3)$$

3.7 Radical Scavenging Experiment

The radical scavenging experiment was carried out to demonstrate the importance and function of active species in the photodegradation of RhB and photoreduction of Cr(VI) over a Bi_2WO_6/SnS_2 photocatalyst under sunlight irradiation. A more considerable loss in the photocatalytic efficiency after the addition of the scavenger indicated a more important role for the respective active species in photocatalysis. The test was carried out identically following the procedures for simultaneous photocatalytic activity experiment, except that 3 mM of various scavengers were added to the RhB-Cr(VI) mixture solution before the addition of the photocatalyst. The scavengers used in the experiment were ethanol (EtOH), ethylenediaminetetraacetic acid (EDTA), benzoquinone (BQ), and sodium sulphate (Na_2SO_4). The EtOH was used to scavenge hydroxyl radical ($\bullet OH$), BQ was utilized to identify superoxide radical ($O_2\bullet^-$), EDTA was applied to detect the photogenerated hole (h_{VB}^+), and Na_2SO_4 was used to scavenge photogenerated electron (e_{CB}^-) (Schneider, et al., 2020; Susanti, Afifah and Saleh, 2017).

CHAPTER 4

RESULTS AND DISCUSSION

4.1 Characterization

Catalyst characterization was crucial to determine the physical, chemical, optical, and electronic properties of the as-synthesized photocatalysts. Thereby, a series of analytical technique was employed for the characterization, including X-ray Diffraction (XRD), Attenuated Total Reflectance – Fourier Transform Infrared Spectroscopy (ATR-FTIR), Ultraviolet-Visible Diffuse Reflectance Spectroscopy (UV-vis DRS), Transient Photocurrent Response (TPR), Electrochemcial Impedance Spectroscopy (EIS) and Mott-Schottky (M-S) analysis.

4.1.1 X-ray Diffraction (XRD)

The crystallographic structure of the as-prepared photocatalysts was analysed by XRD. All of the diffraction peaks were detected and indexed using the data from the Joint Committee on Powder Diffraction Standards (JCPDS). Based on Figure 4.2, the diffraction peaks found in the XRD of Bi_2WO_6 photocatalyst can be indexed to the orthorhombic structure of Bi_2WO_6 (JCPDS No. 39-0256). The diffraction peaks at 2θ = 28.36º, 32.91º, 47.18º, 55.95º and 58.60º were highly connected with the planes (131), (200), (202), (062), (331), and (262), respectively (Kumar and Kumar Dutta, 2022). The sharp and intense diffraction peaks indicated the high crystallinity of Bi_2WO_6 photocatalyst. The diffraction peaks of pure SnS_2 photocatalyst, on the other hand, at 2θ = 15.04º, 28.69º, 32.24º, 44.93º, 50.10º and 52.59º were ascribed to (001), (100), (011), (012), (110), and (111) planes, respectively, demonstrating its hexagonal structure (JCPDS Card No. 83-1705) (Kumar and Kumar Dutta, 2022; Xu, et al., 2022).

All characteristic peaks of Bi_2WO_6 and SnS_2 can be clearly noticed in the composites. The strongest peak found in the XRD of pure Bi_2WO_6 sample was (131), suggesting that crystalline anisotropic growth of Bi_2WO_6 occurred mostly along the (131) plane. Hardly no XRD peaks of SnS_2 were detected for Bi_2WO_6/SnS_2 composite, presumably due to its low concentration. However, upon closer inspection of the enlarged view in Figure 4.3, it was noticeable that the peaks at roughly 2θ of 28.3º, which correspond to the (1 3 1) lattice plane, had slightly shifted towards higher degrees. This observation indicates a strong interaction and close contact between Bi_2WO_6 and SnS_2 (Kumar and Kumar Dutta, 2022).

Furthermore, the absence of any impurity peak in the Bi_2WO_6/SnS_2 composites indicated two phase composition of Bi_2WO_6 and SnS_2. Since there were several overlapping peaks, the diffraction peaks of SnS_2 were easily obscured by Bi_2WO_6 when the two were combined. Meanwhile, a more noticeable change was at 2θ = 15.04º where the peak intensity gradually rose with SnS_2 loading in the binary photocatalyst. Overall, these outcomes demonstrated that the two-phase Bi_2WO_6/SnS_2 composites were successfully fabricated.

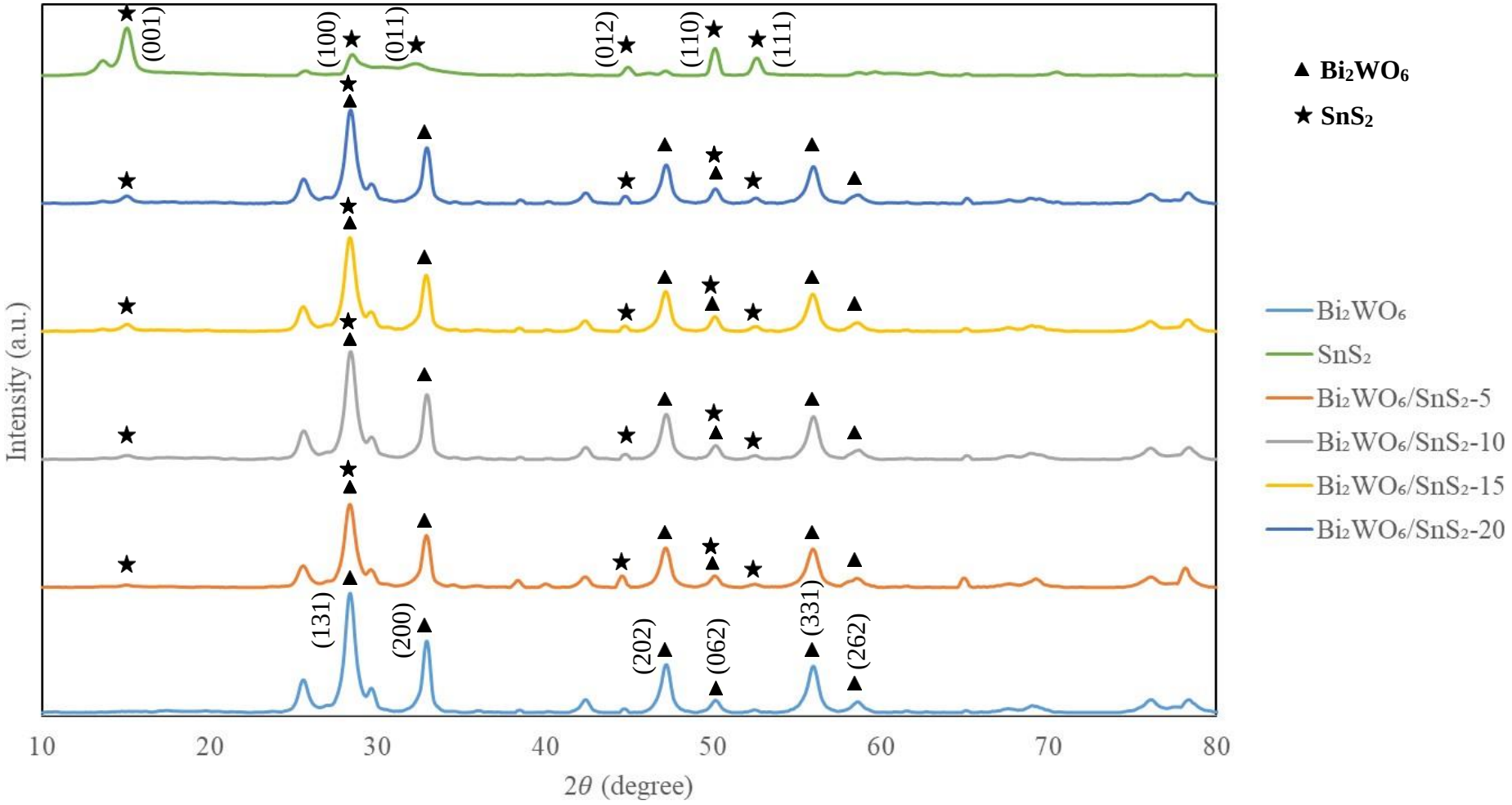

Figure 4.2: XRD Patterns of As-prepared Photocatalysts.

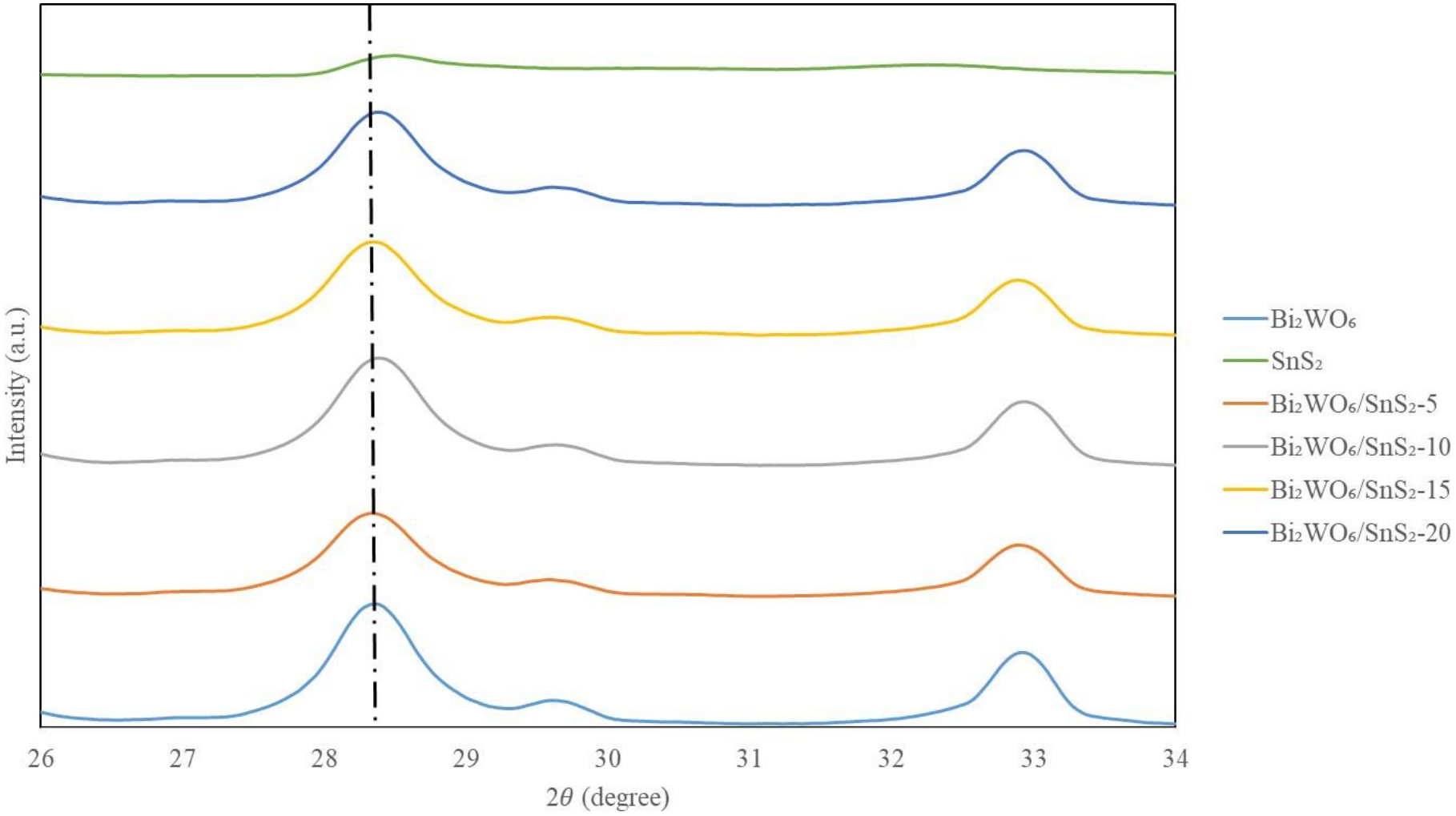

Figure 4.3: XRD Peaks Corresponding to the (1 3 1) Lattice Plane of Pure Bi_2WO_6 and Bi_2WO_6/SnS_2 Composites.

4.1.2 Attenuated Total Reflectance – Fourier Transform Infrared Spectroscopy (ATR-FTIR)

The FTIR spectra of as-synthesized photocatalysts were depicted in Figure 4.4. In general, the Bi_2WO_6 had the absorption bands ranged from 400-1700 cm^{-1}. The peak at 437 cm^{-1} was ascribed to the WO_6 octahedral antisymmetric modes (Mao, et al., 2020). The Bi-O-Bi asymmetric stretch was located at 568 cm^{-1}, while W-O was stretched at 694 cm^{-1} and 1019 cm^{-1}, and the band at 806 cm^{-1} corresponded to the Bi-O bond, which was consistent with the findings by Huang, et al. (2019). The existence of W-O and Bi-O bonds confirmed the formation of Bi_2WO_6. Meanwhile, the absorption bands at 1624 cm^{-1} could be attributed to the O-H stretching and bending vibration of absorbed H_2O molecules on the sample surface (Huang, et al., 2019). Emergence of peaks at 1316 cm^{-1} and 1624 cm^{-1} also verified the presence of C-H bending vibrations and C=C bond, respectively (Arya, et al., 2020). SnS_2, on the other hand, showed numerous peaks at 1428 cm^{-1}, 1612 cm^{-1}, 2919 cm^{-1}, and 3401 cm^{-1}, corresponding to S=O, C=O, –CH, and –OH, respectively. The presence of functional groups such as –OH and S=O may contribute to making SnS_2 anionic or negatively charged, which enables it to be an excellent material for the removal of cationic organic pollutants in an aqueous solution, such as Rhodamine B. Additionally, the interaction between the negatively charged SnS_2 with the selectively positive charged dyes may be primarily caused by electrostatic absorption. (Srivastava, et al., 2021)

Overall, all of the as-prepared binary photocatalysts displayed the vibration bands of both Bi_2WO_6 and SnS_2. It was observed that as SnS_2 content increased, the intensity at roughly 700 cm^{-1} reduced gradually, probably due to a decrease in the per unit volume of the functional group associated with the W-O bond (Khanam and Rout, 2022). SnS_2 deposition on Bi_2WO_6 inhibited the IR radiation from reaching the molecule, hence reducing light absorption by W-O bond (Khanam and Rout, 2022). Next, the peaks at roughly 1630 cm^{-1} and 3400 cm^{-1} grew more visible and stronger. Furthermore, the peak at roughly 1320 cm^{-1} was missing for the composites with high SnS_2 loading (> 10 wt%). For the remaining peaks, the loading of SnS_2 had no discernible effect due to the low content and peak overlapping.

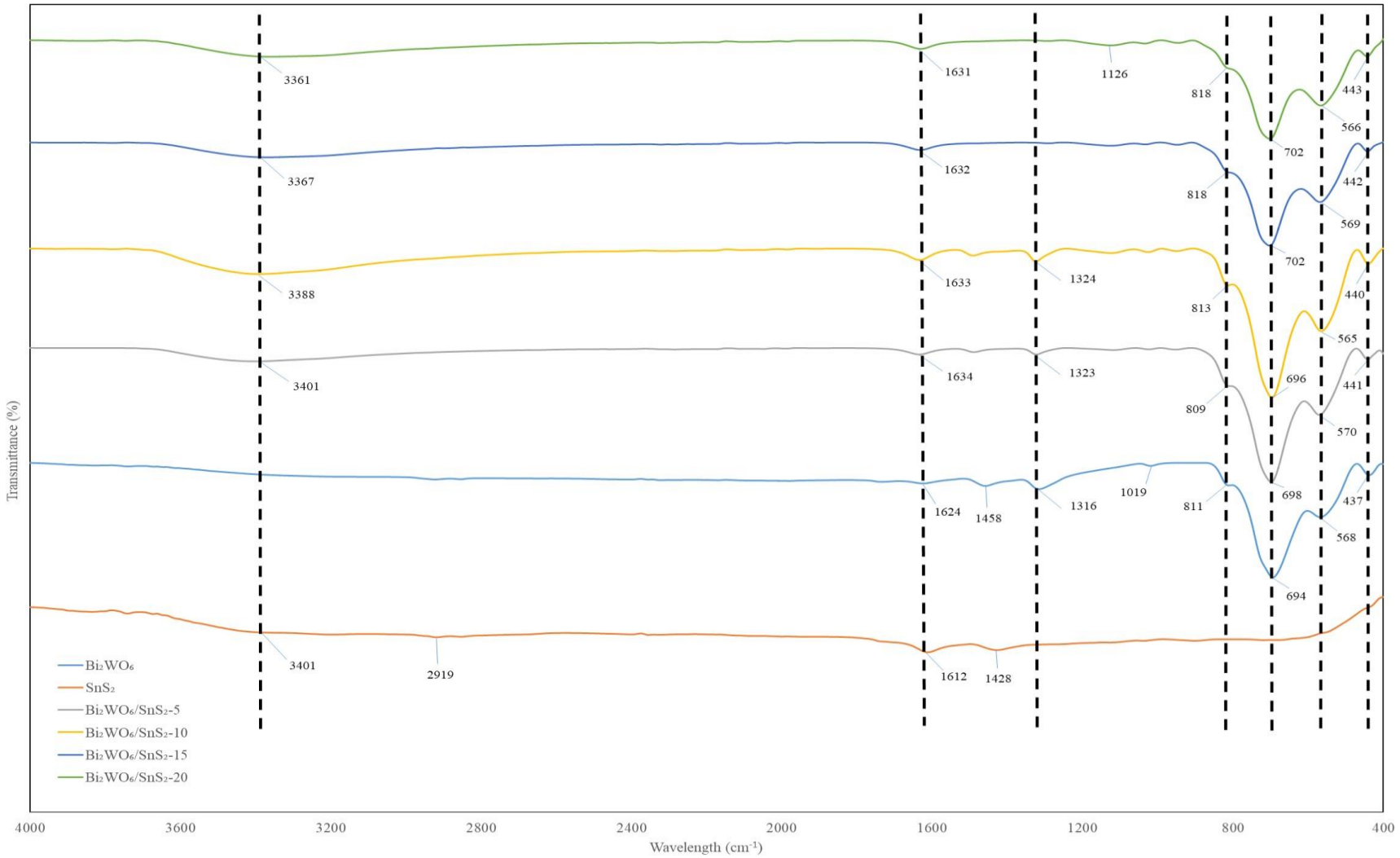

Figure 4.4: ATR-FTIR Spectra of As-prepared Photocatalysts.

4.1.3 Ultraviolet-visible Diffuse Reflectance Spectroscopy (UV-vis DRS)

The optical properties and energy structure of the as-prepared photocatalysts were examined by UV-vis DRS. Based on Figure 4.5, the optical absorption band edges of pristine Bi_2WO_6 and SnS_2 were located at 410 nm and 515 nm, respectively. These findings concluded that Bi_2WO_6 exhibited strong photoresponse properties from the UV light region to the low visible light frequency region owing to its intrinsic band gap transition, whereas SnS_2 exhibited high photon absorption in the visible light region. Notably, after coupling with SnS_2, the light absorption of Bi_2WO_6/SnS_2-10 photocatalyst slightly shifted to longer wavelength (465 nm) in comparison with the pristine Bi_2WO_6. The enhanced visible light absorption could be attributed to the heterojunction development and photosensitization of SnS_2, allowing Bi_2WO_6/SnS_2-10 photocatalyst to have a considerable tendency to capture a broader sunlight spectrum and generate more photoinduced charge carriers for higher photoactivities.

Moreover, the plot of band gap emissions of several as-prepared photocatalysts was showed in Figure 4.7, which was originated from Kubelka-Munk approach. The equation being used for relation was as follows (Srivastava, et al., 2021):

$$(\alpha hv)^{1/n} = B(hv - E_g) \tag{4.1}$$

where

E_g = optical energy band gap, eV

B = optical-transition-dependent constant

v = frequency of the incident beam, Hz

n = nature of transition (n = 2 for allowed transition and n = 3 for forbidden transition)

h = Planck's constant, J·s

Kubelka-Munk function was used to calculate the absorption coefficient (α) and estimate the absorption edge energy. Following that, the curves of $[F(R)hv]^{1/2}$ vs (hv) for the photocatalysts were plotted. Overall, the estimated band gap values of Bi_2WO_6, SnS_2 and Bi_2WO_6/SnS_2-10 photocatalysts were 2.95 eV, 2.3 eV and 2.55

eV, respectively. As compared to the pristine Bi_2WO_6, the binary composite had a lower band gap value, plausibly due to the incorporation of SnS_2 with narrow band gap. This integration facilitated more stimulation of photogenerated electron-hole pairs, improving the light utilization efficiency and resulting in escalated photocatalytic activity.

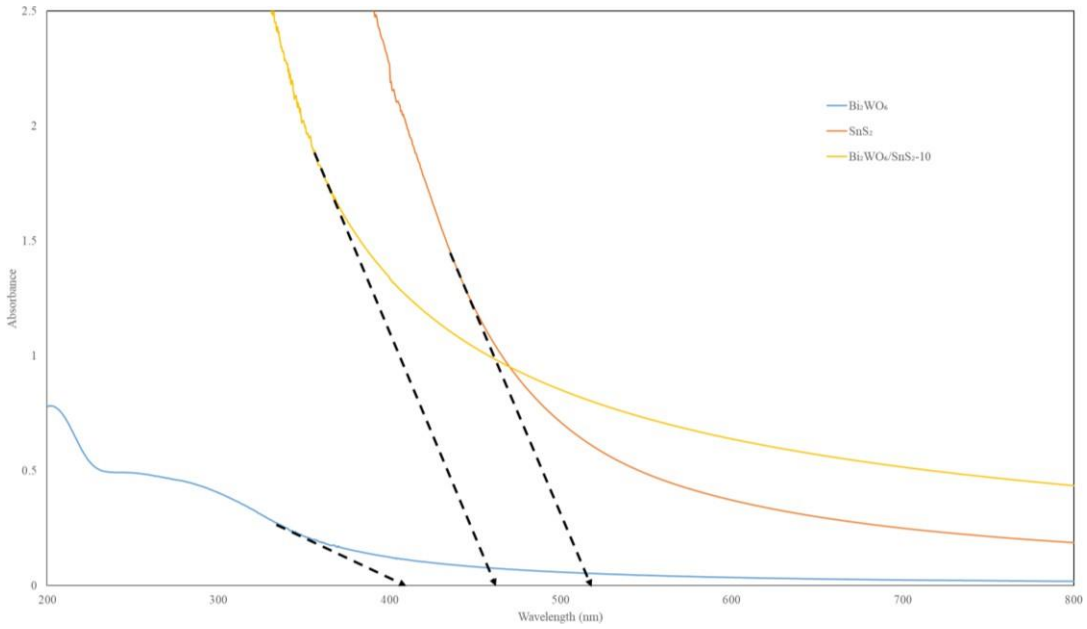

Figure 4.5: UV-vis Absorbance Spectra of the As-prepared Photocatalysts.

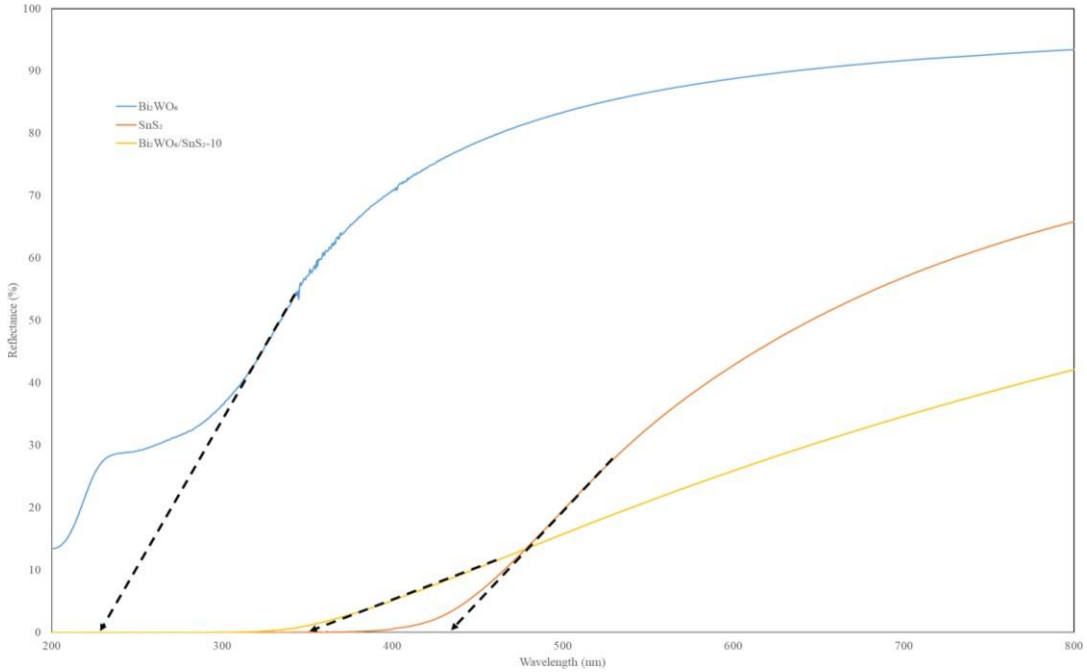

Figure 4.6: UV-vis Reflectance Spectra of the As-prepared Photocatalysts.

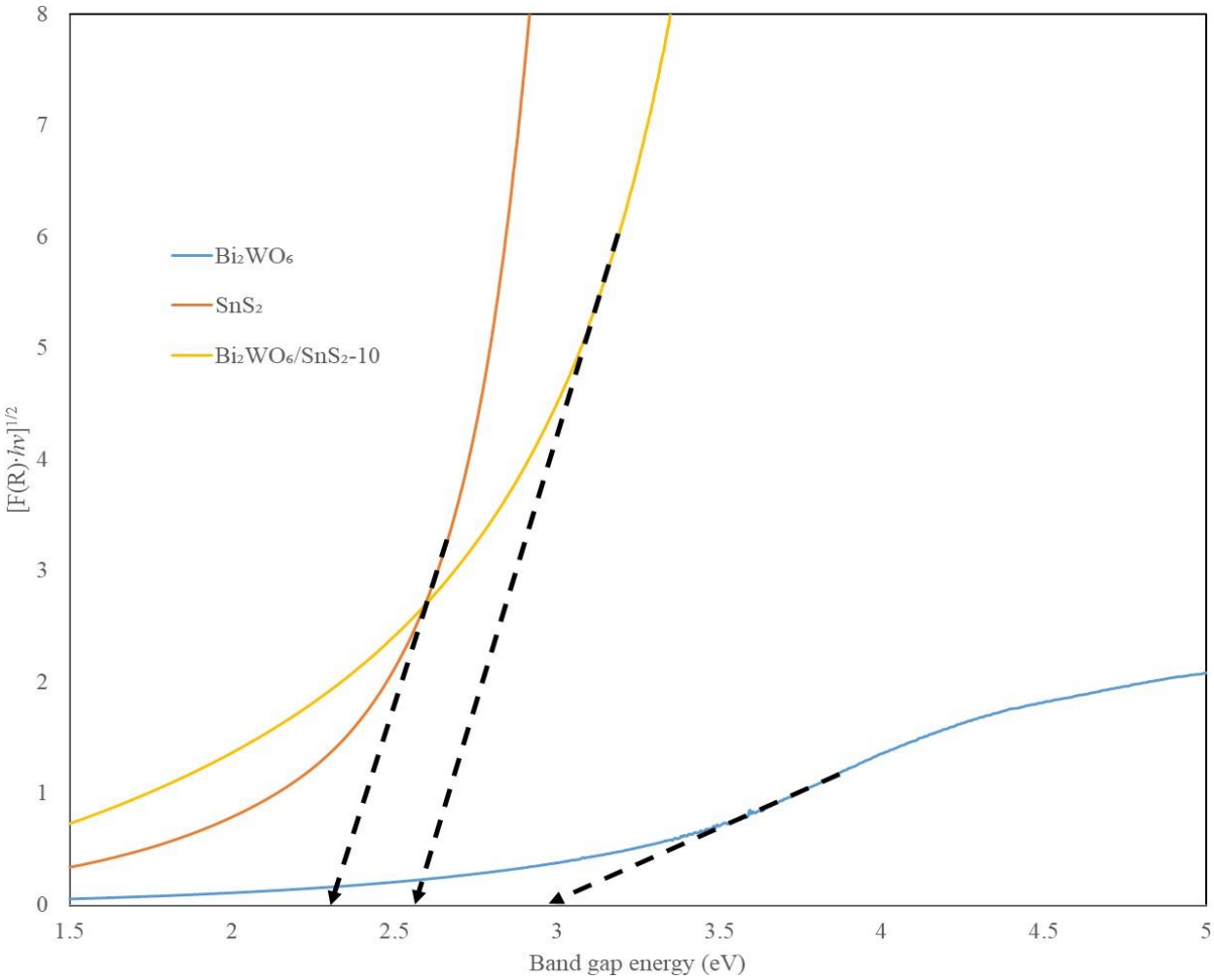

Figure 4.7: Kubelka-Munk Plot of the As-prepared Photocatalysts.

4.1.4 Transient Photocurrent Response (TPR), Electrochemical Impedance Spectroscopy (EIS) and Mott-Schottky (M-S)

TPR analysis was used to evaluate the capability of a photocatalyst to suppress the recombination of charge carriers. As shown in Figure 4.8 (a), the photocurrent density of pristine Bi_2WO_6 for three on-off cycles was very low when compared to Bi_2WO_6/SnS_2-10 due to its quick recombination of charge carriers. When exposed to light, the photocurrent density of both photocatalysts increased rapidly to a maximum value when the light was turned on, then progressively reduced to achieve a steady state value before dropping abruptly when the light was turned off. This result demonstrated that the separation and migration of photogenerated charge carriers were considerably better in the fabricated composite than in the single-phase component sample. To support the aforesaid TPR measurements, EIS investigation was carried out as shown in Figure 4.8 (b). Generally, a smaller arc radius in the Nyquist plot represented a greater charge carrier separation and a faster interfacial charge transfer. As expected, the arc radius in the EIS spectrum followed the order of Bi_2WO_6 > Bi_2WO_6/SnS_2-10, verifying that as-fabricated composite had the weakest resistance of charge separation and migration. To summarise, the results of TPR and EIS validated that constructing Bi_2WO_6/SnS_2 heterojunction accelerated the charge carrier separation and migration, which can improve the photocatalytic performance.

Furthermore, the band alignment of the semiconductors was examined using Mott-Schottky (M-S) analysis, as illustrated in Figure 4.8 (c-d). Bi_2WO_6 was an n-type semiconductor with a positive slope of the curve in M-S plot, which was in contrast to SnS_2. From the experiment, the conduction band (CB) potentials were determined to be 0.31 eV for Bi_2WO_6 and 0.085 eV for SnS_2. Particularly, their valence band (VB) potentials can be determined by summing the values of E_g and E_{CB}. By referring to the Kubelka-Munk analysis depicted in Figure 4.6, the band gap (E_g) of pristine Bi_2WO_6 and SnS_2 was 2.95 eV and 2.3 eV, respectively. Accordingly, the computed E_{VB} of Bi_2WO_6 and SnS_2 was 3.26 eV and 2.39 eV, respectively. Therefore, the staggered band alignment feature in the Bi_2WO_6/SnS_2 composites matched the criterion for the construction of a Z-scheme heterojunction, which enabled effective separation of interfacial charge carriers and strong redox abilities.

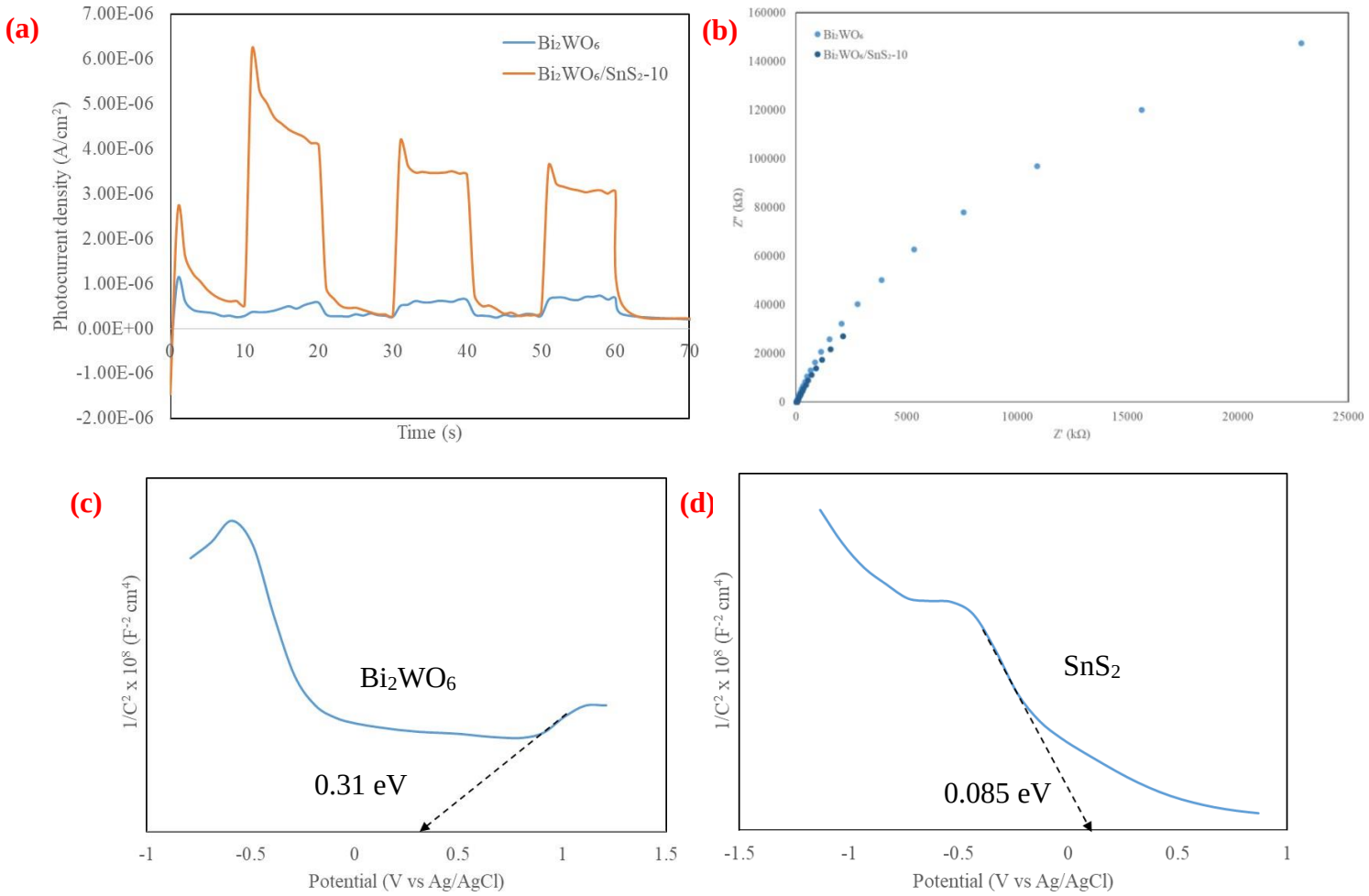

Figure 4.8: (a) Transient Photocurrent Response and (b) EIS Measurements of Pristine Bi_2WO_6 and Bi_2WO_6/SnS_2-10; (c-d) M-S Analysis of Pristine Bi_2WO_6 and SnS_2.

4.2 Solar Light Irradiation Photocatalytic Activities

4.2.1 Photodegradation of Rhodamine B (RhB)

Figure 4.9 displayed the degradation profiles of Rhodamine B over various as-prepared photocatalysts. Based on the blank test result, it showed that the self-degradation of RhB dye was negligible, hence it was very stable under solar light irradiation without any photocatalyst. In addition, RhB did not substantially degrade in the presence of photocatalyst under dark conditions, implying that RhB degradation was primary induced by the photocatalytic activity of excited semiconductors. As expected, RhB dye was degraded gradually by all the as-prepared photocatalysts as reaction time increased. Pure Bi_2WO_6 had degraded 88.91 % of RhB dye, whereas the Bi_2WO_6/SnS_2-10 binary photocatalyst demonstrated the highest photocatalytic activity with RhB dye degradation efficiency of 95.50 % in 180 minutes. The incorporation of SnS_2 successfully improved the photocatalytic performance of Bi_2WO_6. The SnS_2 nanoparticles were well-interspersed on the Bi_2WO_6 surface, promoting the development of heterojunction through the interfaces and facilitating the charge separation and transfer (Xu, et al., 2022).

Figure 4.10 showed that the absorption peak of RhB gradually weakened and shifted to shorter wavelength step by step over extended period of time in the presence of Bi_2WO_6/SnS_2-10 binary composite, with an absorption band centred at 553.5 nm. RhB degradation in the presence of photocatalyst under visible irradiation underwent the *N*-deethylation process, which involved a subsequent detachment of ethyl groups from the amino nitrogen atoms, leading in a hypsochromic shift of absorption and emission maxima (Jakimińska, Pawlicki and Macyk, 2022). The formation of *N*-de-ethylated intermediates occurred stepwise, that was, from *N,N,N',N'*-tetraethylated rhodamine to rhodamine (Li, Liu and Huang, 2008). In addition, the inset of Figure 4.10 showed the decolourization of RhB dye within 180 minutes of reaction time. The colour of the dye solution changed from pink to colourless, which could be seen with the naked eye.

Subsequently, the collected degradation data was quantitatively analysed by fitting to a Langmuir Hinshelwood kinetic model to evaluate the photocatalytic efficiency of the samples. Figure 4.11 demonstrated a linear relationship between –ln (C/C_o) and irradiation time (t) for all the as-prepared photocatalysts, implying that the photodegradation reaction obeyed the pseudo-first-order-kinetic. As shown in Figure 4.12, the Bi_2WO_6/SnS_2-10 had the largest apparent reaction rate constant, k_{app} (0.0178 min^{-1}), which was approximately 1.5-fold higher than the pristine Bi_2WO_6 (0.0119 min^{-1}). Particularly, the k_{app} value of the as-prepared photocatalysts decreased in the order of Bi_2WO_6/SnS_2-10 > Bi_2WO_6/SnS_2-20 > Bi_2WO_6/SnS_2-15 > Bi_2WO_6/SnS_2-5 > pure Bi_2WO_6. Based on the results obtained, it was worth noting that 10 wt% was the optimum SnS_2 loading in the binary photocatalyst. This finding elucidated the excess SnS_2 loading reduced the number of active sites available on Bi_2WO_6, hampered the entering sunlight, and hence retarded the performance of binary photocatalysts. The aforesaid findings led to the conclusion that a proper loading amount of SnS_2 can significantly enhance the photoactivity of nanocomposite. This could be due to the following reasons (Xu, et al., 2022): (1) when the loading amount of SnS_2 was less than that of Bi_2WO_6/SnS_2-10, the synergistic effect between the Bi_2WO_6 and SnS_2 was insufficient, which weakened the migration of charge carriers; (2) when the loading amount of SnS_2 was greater than that of Bi_2WO_6/SnS_2-10, the active sites of Bi_2WO_6 were largely shielded by excessive SnS_2, therefore becoming the recombination centres for charge carriers and retarding the photocatalytic performance. All of these results were in good agreement with the charge carrier dynamics analyses of the nanocomposites.

More interestingly, similar findings were reported in the study by Zhu and co-workers (2019), who investigated the effect of CuS loading in Bi_2WO_6 on the photodegradation efficiency of RhB dye. They prepared CuS/Bi_2WO_6 composites via a facile hydrothermal method with different molar ratios (BWO-x, where x = 0, 1, 2, 3, 4), and they discovered that BWO-3 ($CuS:Bi_2WO_6$ = 1:5) demonstrated the best photocatalytic performance (96.19 % RhB removal) with an apparent rate constant 1.59 times higher than BWO-0 (pure Bi_2WO_6). They discovered that increasing the CuS loading in Bi_2WO_6 will improve the photocatalytic performance to some extent, as the presence of CuS could affect the morphology and greatly enhance the photogenerated charge carrier separation efficiency. Zhang, et al. (2016), on the other

hand, conducted a similar investigation on the impact of $SrTiO_3$ loading in Bi_2WO_6 on the photodegradation efficiency of RhB. The binary photocatalyst was hydrothermally synthesised in a variety of $SrTiO_3$ loading (1, 8, 10, and 15 wt%), and they discovered that Bi_2WO_6 loaded with 8 wt% $SrTiO_3$ was the most photocatalytically active material, exhibiting a 98.4 % degradation rate and a 0.0463 min^{-1} apparent reaction rate constant. They deduced that the enhanced photoactivity demonstrated by the composite was owing to the efficient development of the heterostructure between Bi_2WO_6 and $SrTiO_3$. However, they also found out that the photocatalytic performance of the composite rose up to 8 wt%, then reduced substantially with additional increases in CuS loading, implying that 8 wt% demonstrated the maximal photocatalytic performance due to its excellent separation efficiency. They went on to say that this scenario could be owing to the inadequate formation of the heterojunction originated by the immoderately low $SrTiO_3$ loading, or the formation of new recombination sites caused by its overloading.

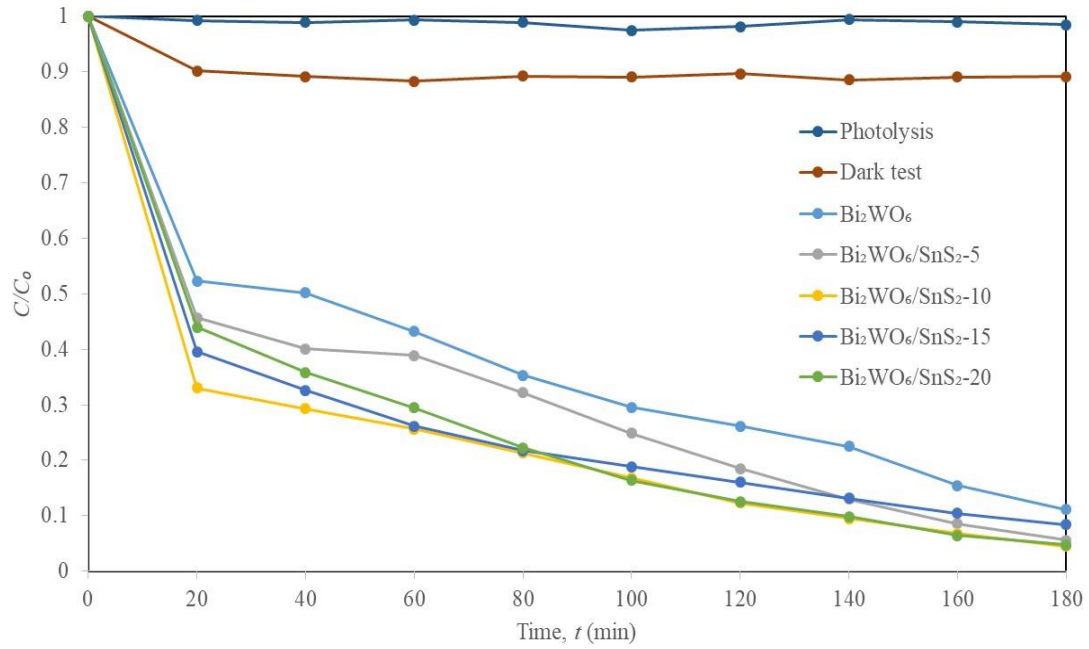

Figure 4.9: Degradation Profiles of Rhodamine B Over Various As-prepared Photocatalysts.

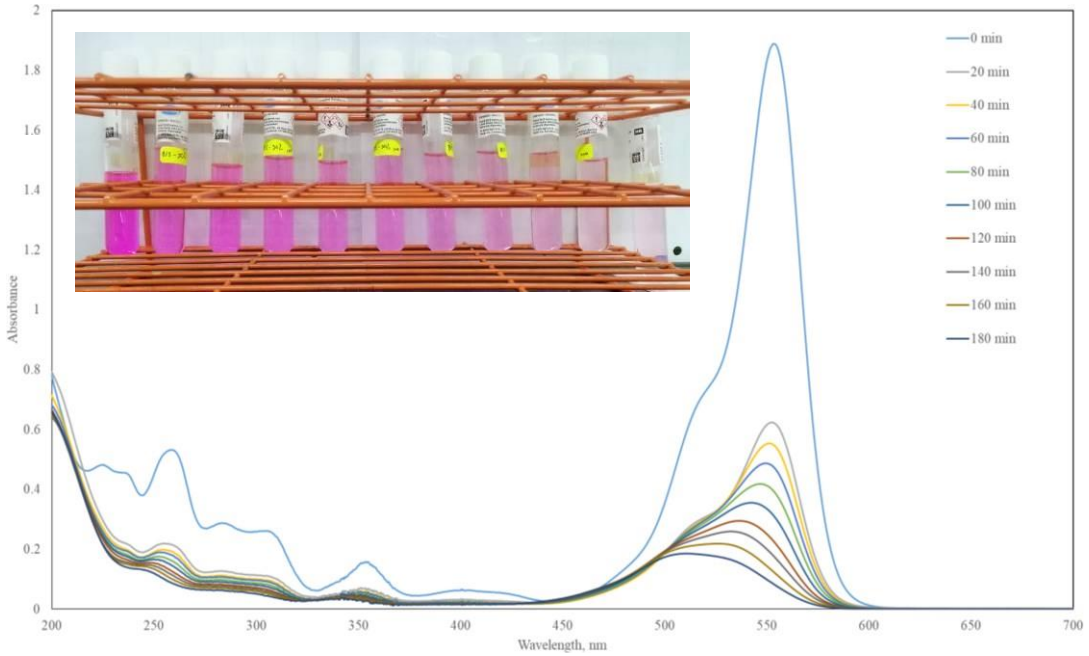

Figure 4.10: Absorption Spectra of Rhodamine B Over Bi_2WO_6/SnS_2-10 Binary Composite With the Decolourization Inset.

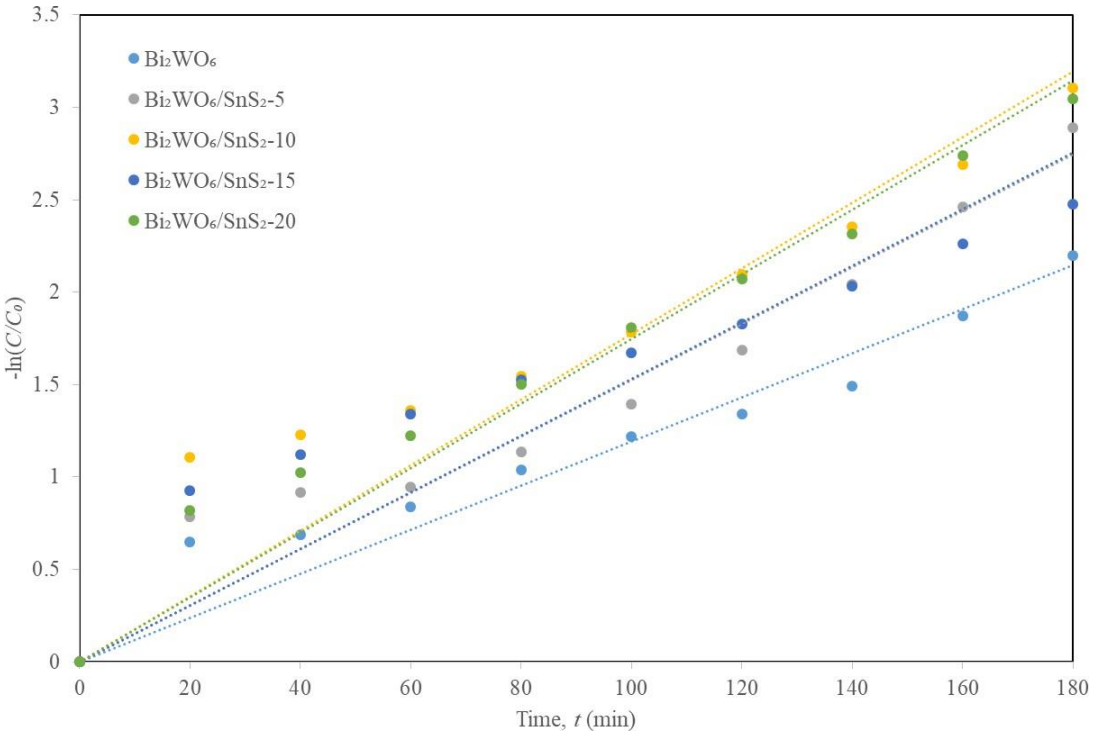

Figure 4.11: Kinetic Study for the Photodegradation of Rhodamine B.

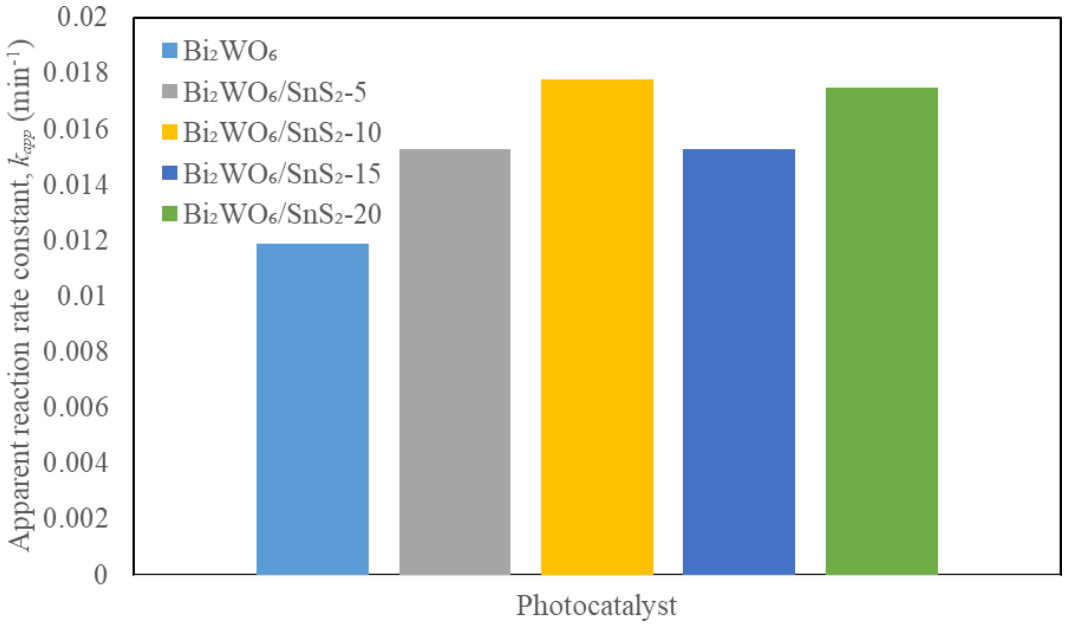

Figure 4.12: Apparent Reaction Rate Constant, k_{app} of Various Photocatalysts.

4.2.2 Photoreduction of Cr(VI)

Figure 4.13 illustrated the Cr(VI) reduction profiles over various as-prepared photocatalysts. Evidently, the photolysis result suggested that the self-reduction ability of Cr(VI) under sunlight irradiation could be neglected. There was also no significant reduction of Cr(VI) in the presence of photocatalyst under dark conditions, implying that the Cr(VI) reduction was primary induced by the photocatalytic activity of excited semiconductors. Notably, the Cr(VI) concentration gradually reduced as the reaction time increased for all the synthesized photocatalysts. Similar to RhB degradation, the Bi_2WO_6/SnS_2-10 binary photocatalyst had the best photocatalytic ability, whereby it reduced 100 % of Cr(VI) within 180 minutes of solar light irradiation. In comparison, the photocatalytic efficiency of pristine Bi_2WO_6 in Cr(VI) reduction was just 48.23 %.

Figure 4.14 revealed that the absorption peak of Cr(VI) gradually weakened over extended period of time in the presence of Bi_2WO_6/SnS_2-10 binary composite, with an absorption peak centred at 542.5 nm. In addition, the inset of Figure 4.14 showed a visual comparison of Cr(VI) reduction via a diphenylcarbazide method. In a mineral acid solution, diphenylcarbazide showed a sensitive and specific colour response with hexavalent chromium (Islam, et al., 2019). When diphenylcarbazide was oxidized by hexavalent chromium, a redox reaction formed 1,5-diphenylcarbazone, which was simultaneously combined with chromium. The purple chromophore was a chromium (III) and 1,5-diphenylcarbazone chelate. Based on the figure, the colour of Cr(VI) solution changed from purple to colourless, which could be seen with the naked eye.

The linear fitting of experimental data to the Langmuir Hinshelwood kinetic model, as shown in Figure 4.15, indicated that Cr(VI) photoreduction followed the pseudo-first-order kinetics. According to Figure 4.16, the apparent reaction rate constant, k_{app} of Bi_2WO_6/SnS_2-10 approached 0.0513 min^{-1}, which was almost 10 times more than that of pure Bi_2WO_6 (0.0051 min^{-1}). In particular, the k_{app} values of the as-prepared photocatalysts were obtained in the following order: Bi_2WO_6/SnS_2-10 > Bi_2WO_6/SnS_2-15 > Bi_2WO_6/SnS_2-20 > Bi_2WO_6/SnS_2-5 > pure Bi_2WO_6. As the SnS_2 loading in binary Bi_2WO_6/SnS_2 composite increased from 5 wt% to 10 wt%, it

was envisaged that more SnS_2 nanoparticles were attached on the surface of Bi_2WO_6, which encouraged the formation of heterojunction between SnS_2 and Bi_2WO_6, facilitating charge transfer and suppressing the recombination of photogenerated charge carriers. By a similar reasoning as discussed in Section 4.2.1, the presence of excessive SnS_2 content in the binary photocatalyst (over 10 wt%) will deteriorate the photocatalytic performance.

Indeed, Hu and Liu (2021) performed a study on the impact of $CuAlO_2$ loading in Bi_2WO_6 on the photoreduction efficiency of Cr(VI). The binary photocatalyst was synthesized using the ball milling method with varying $CuAlO_2$ loading (0.2, 0.5, 1.0, 3.0, 5.0, 10 and 20 wt%). They found that the optimal concentration of $CuAlO_2$ in the composite was 1.0 wt%, which could reduce Cr(VI) by 93.0% within 150 minutes with an optimum rate constant that was 4.7 times higher than that of pure Bi_2WO_6. They came to the conclusion that the improved photocatalytic reduction activity was due to the high conductivity, clearly defined composite interface, and favourable crystal morphology of the composite. In case of the effect of $CuAlO_2$ loading, the charge carrier trapping site increased along with the $CuAlO_2$ content up to 1.0 wt%, which extended charge carrier longevity and enhanced the photoreduction performance. However, when the concentration of $CuAlO_2$ exceeded 1.0 wt%, the highly concentrated dopant may act as the recombination centre for the electrons and holes, thereby gradually reducing the photoreduction performance. Hence, only an appropriate loading range can enhance the photocatalytic performance of a composite.

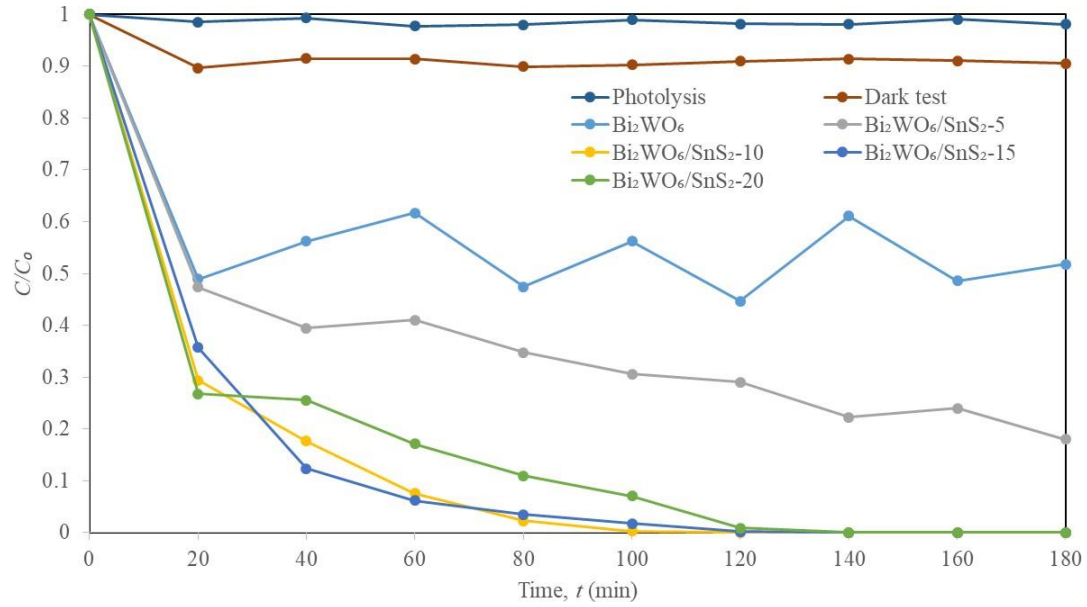

Figure 4.13: Degradation Profiles of Cr(VI) Over Various As-prepared Photocatalysts.

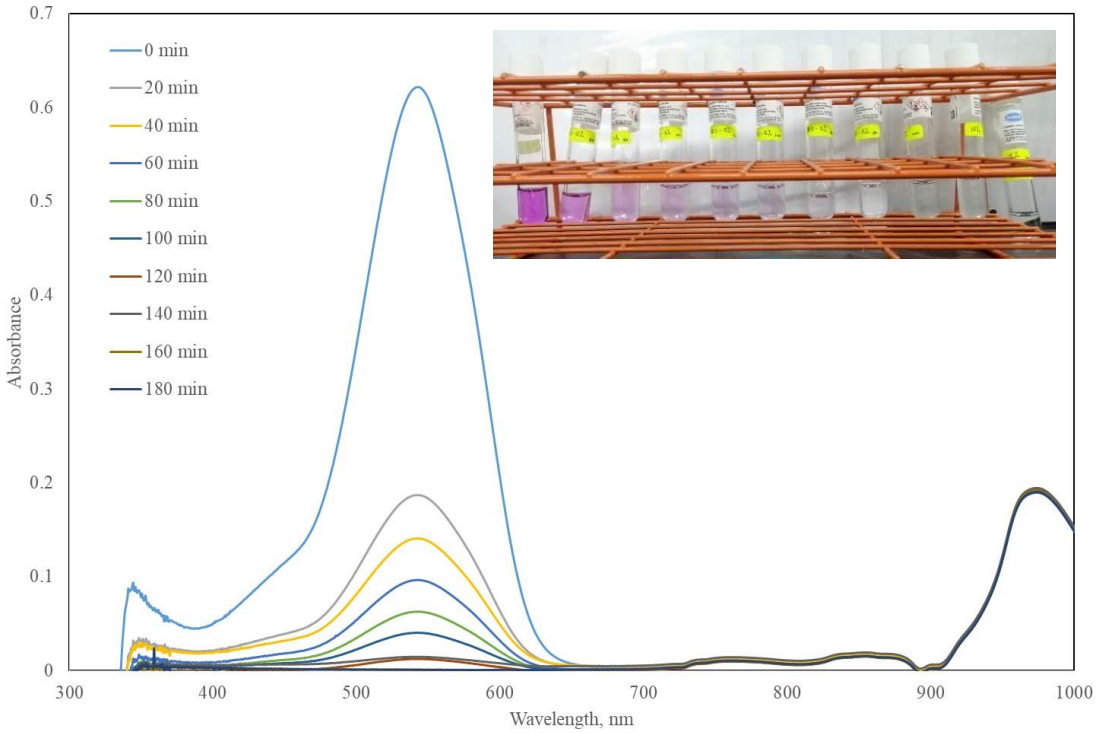

Figure 4.14: Absorption Spectra of Cr(VI) Over Bi_2WO_6/SnS_2-10 Binary Composite With the Decolourization Inset.

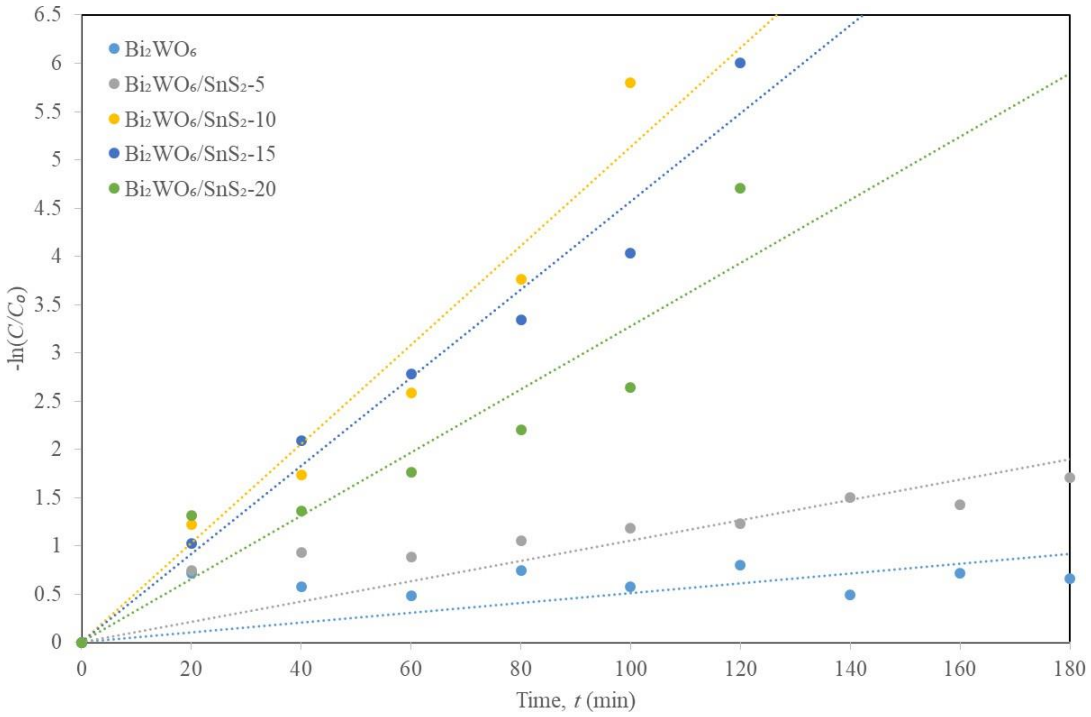

Figure 4.15: Kinetic Study for the Photoreduction of Cr(VI).

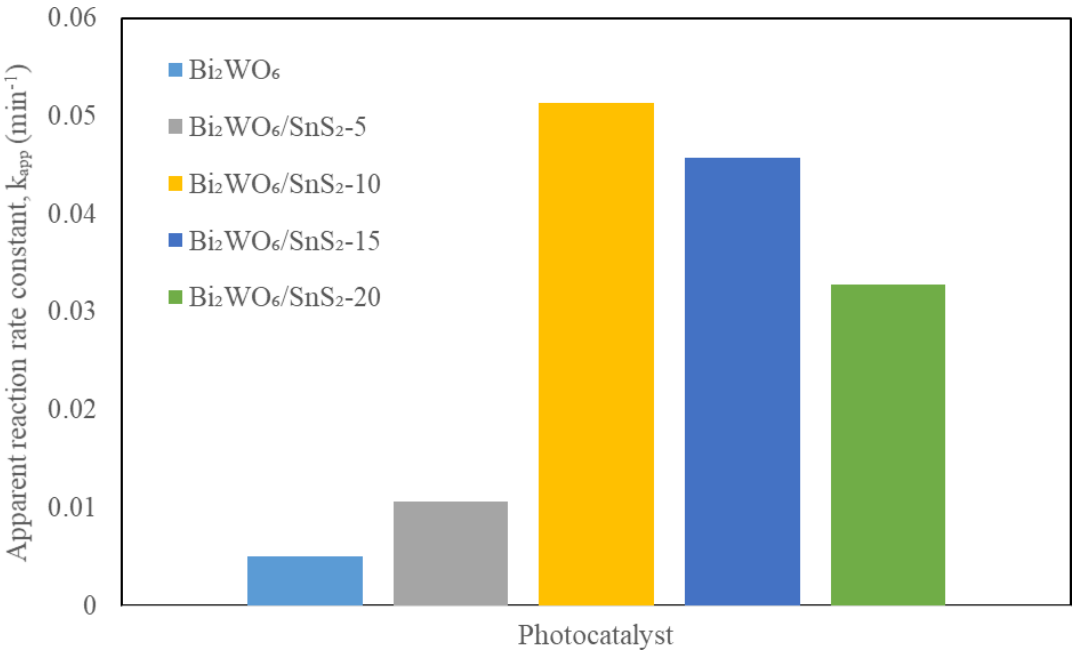

Figure 4.16: Apparent Reaction Rate Constant, k_{app} of Various Photocatalysts.

4.2.3 Simultaneously removing of RhB and Cr(VI)

Based on the previous findings, Bi_2WO_6/SnS_2-10 outperformed other composites with various SnS_2 loadings in terms of RhB photodegradation and Cr(VI) photoreduction. In order to further investigate the photoactivity over Bi_2WO_6/SnS_2-10, simultaneous decomposition of RhB and Cr(VI) in a mixed pollutant solution was performed.

As shown in Figure 4.17 (a) and Figure 4.18 (a), both RhB and Cr(VI) were hardly decomposed in the absence of any photocatalyst, indicating the negligibility of photolysis. Furthermore, the contribution of dark adsorption by Bi_2WO_6/SnS_2-10 composite towards RhB and Cr(VI) decomposition was insignificant. Clearly, the concentrations of both RhB and Cr(VI) fell progressively as the irradiation time increased for all the fabricated photocatalysts. The pristine Bi_2WO_6 exhibited poor photoactivities after 180 minutes of exposure due to the high charge carrier recombination rate. More excitingly, remarkably improved photoactivities were obtained with the decoration of SnS_2 onto Bi_2WO_6. The photocatalytic performance of Bi_2WO_6/SnS_2-10 was superior. After 180 minutes of irradiation, the RhB degradation and Cr(VI) reduction efficiency of Bi_2WO_6/SnS_2-10 were 83.19 % and 94.60 %, respectively. One can note that the decomposition of RhB and Cr(VI) in the mixed pollutant solution over Bi_2WO_6/SnS_2-10 were slightly lower than that in single pollutant system. These differences, however, had no effect on the fact that the as-fabricated sample was capable of driving synchronous photooxidation and photoreduction processes in a catalytic reaction. The photocatalytic improvement in the presence of two model pollutants was mostly due to the enhanced excitation number and effective utilization of photogenerated charge carriers, as RhB and Cr(VI) can act as sacrificial agents for photogenerated hole and electron, respectively (Mao, et al., 2020).

Figure 4.17 (b) and Figure 4.18 (b) revealed that the absorption peaks intensities of RhB and Cr(VI) gradually weakened over extended period of time in the presence of Bi_2WO_6/SnS_2-10 binary composite, with the absorption bands positioned at 553.5 and 542.5 nm, respectively. Similarly, the peak position of RhB blue-shifted, indicating the decomposition of RhB molecules. The insets showed the

decolourization of both pollutants within 180 minutes of reaction time, which was plainly visible to the naked eye. Following that, Figure 4.17 (c) and Figure 4.18 (c) demonstrated the reaction kinetics of RhB degradation and Cr(VI) reduction over different photocatalysts. The kinetic fitting of experimental data revealed that the photocatalysis followed a pseudo first-order kinetic model with satisfactory linearity. It could be evidently found that the Bi_2WO_6/SnS_2-10 had the higher decomposition rates of RhB (0.0082 min^{-1}) and Cr(VI) (0.0159 min^{-1}), which were about 1.7-fold and 5.1-fold higher than those of Bi_2WO_6 (0.0049 min^{-1} and 0.0031 min^{-1}, respectively).

In order to demonstrate the high photoactivity of as-fabricated Bi_2WO_6/SnS_2-10 composite, some of the studies on the simultaneous photocatalytic decomposition of RhB and Cr(VI) were summarized in Table 4.1. These findings were able to prove that the as-fabricated Bi_2WO_6/SnS_2-10 composite used in this work had excellent photoactivity.

Table 4.1: Comparison of Synchronous Photocatalytic RhB Degradation and Cr(VI) Reduction Over Other Photocatalysts.

Photocatalyst	Photocatalyst dosage (g/L)	[RhB]	[Cr(VI)]	Light source	Time (min)	RhB degradation (%) / *k* (min^{-1})	Cr(VI) reduction (%) / *k* (min^{-1})	Reference
UiO-66-NH_2/BiOBr	0.5	10 mg/L	50 mg/L	300 W visible light	120	80.32 %	85.48 %	(Yu, et al., 2022)
$FeVO_4$/$Bi_4O_5Br_2$/BiOBr	0.5	10 mg/L	30 mg/L	50 W visible light	360	39.6 % / 0.002 min^{-1}	54.8 % / 0.0056 min^{-1}	(Chachvalvutikul, Luangwanta and Kaowphong, 2021)
BiOBr/CCNF	0.5	10 mg/L	10 mg/L	200 W visible light	120	~100 %	~70 %	(Gan, et al., 2020)
Am-TiO_2	1.0	10 μmol/L	80 μmol/L	500 W visible light	100	97.8 %	53.5 %	(Wang, et al., 2013)
Bi_2WO_6/CuS	1.0	10 mg/L	15 mg/L	500 W visible light	100	98.78 %	95.08 %	(Mao, et al., 2020)
Bi_2WO_6/SnS_2-10	1.0	10 mg/L	10 mg/L	Solar light	180	83.19 % / 0.0082 min^{-1}	94.60 % / 0.0159 min^{-1}	Current study

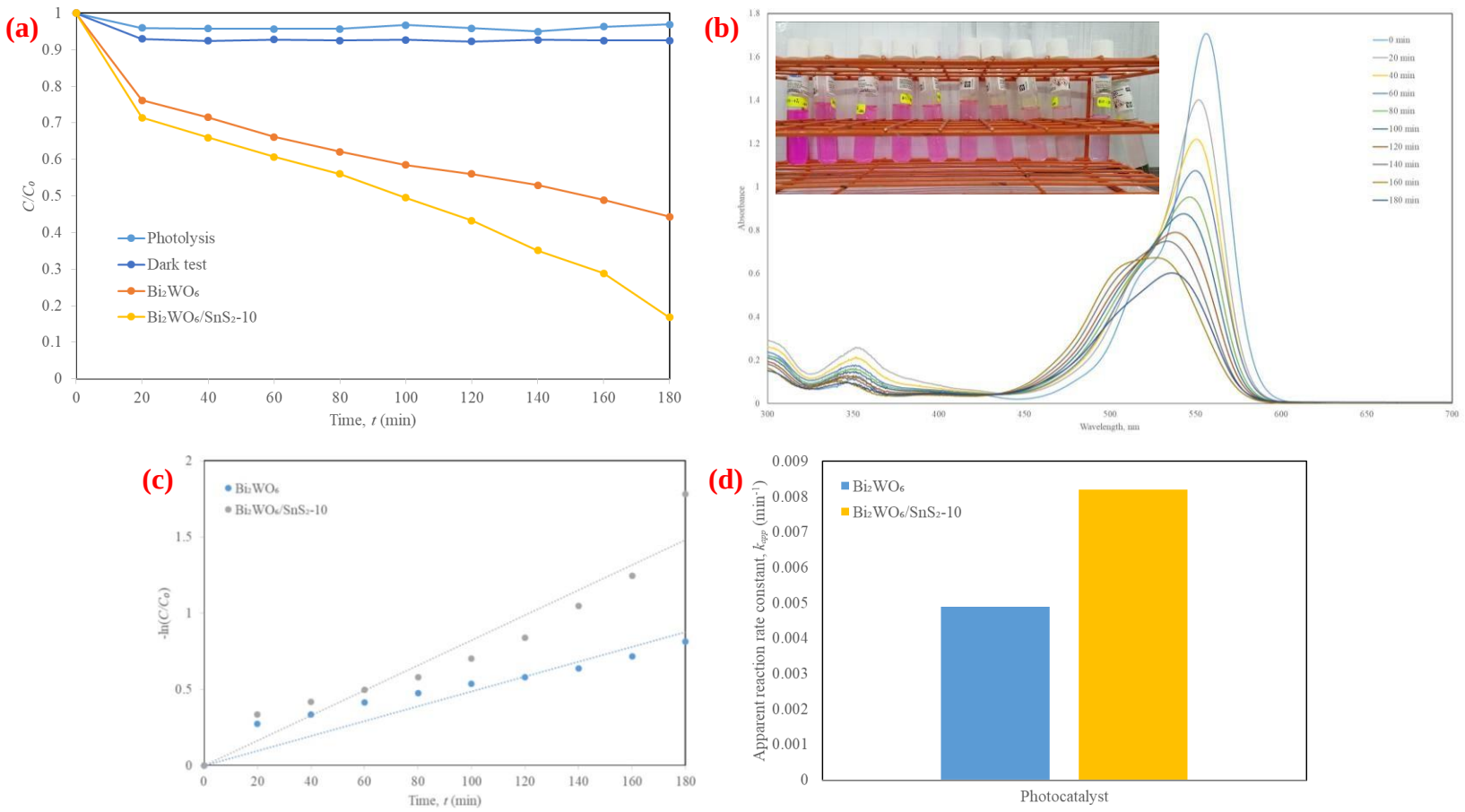

Figure 4.17: (a) Degradation Profiles of Rhodamine B in Binary Pollutant Mixture Over Bi_2WO_6 and Bi_2WO_6/SnS_2-10; (b) Absorption Spectra of Rhodamine B Over Bi_2WO_6/SnS_2-10 Binary Composite With the Decolourization Inset; (c) Kinetic Study for the Photodegradation of Rhodamine B; (d) Apparent Reaction Rate Constant, k_{app} of Bi_2WO_6 and Bi_2WO_6/SnS_2-10.

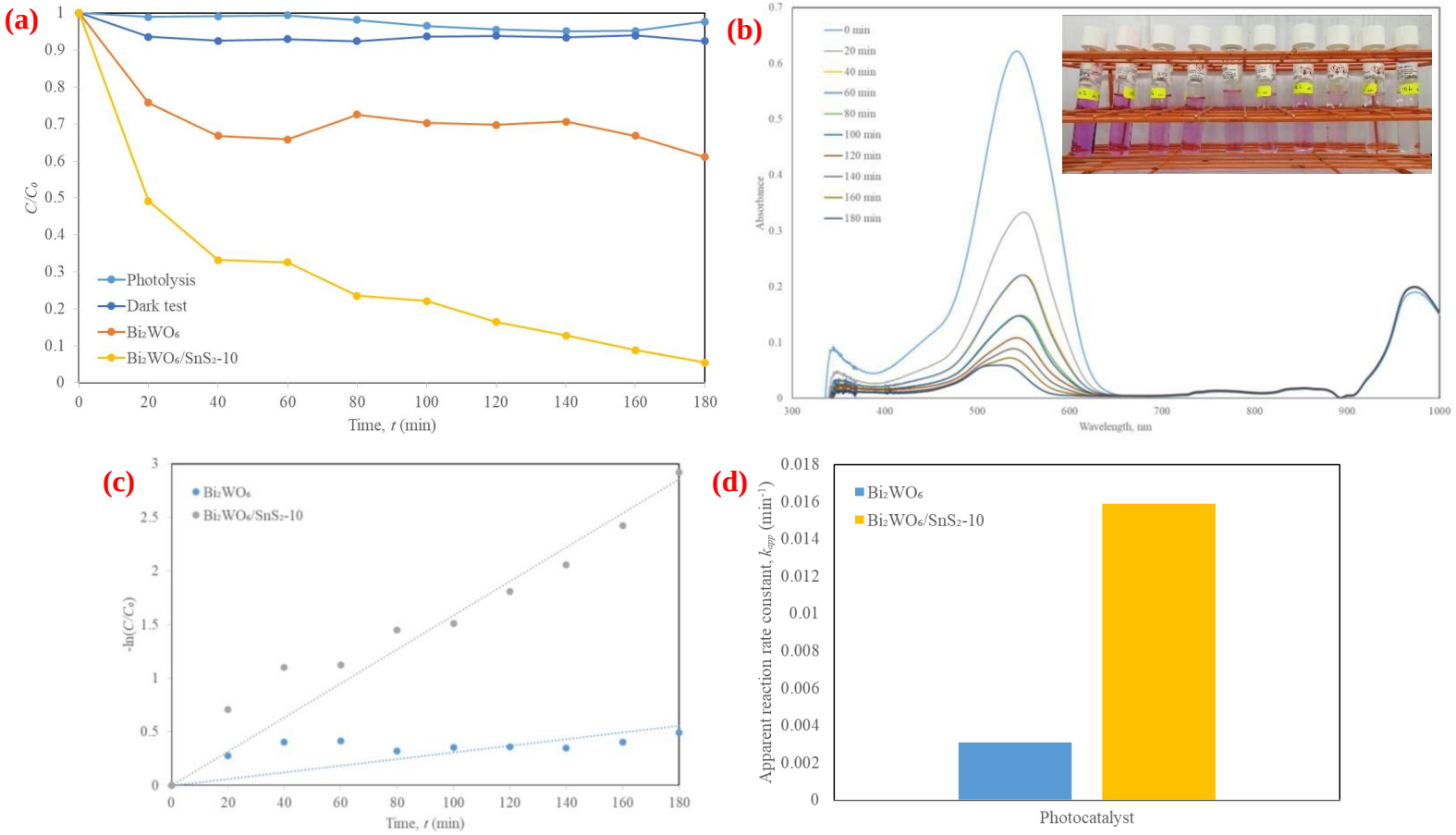

Figure 4.18: (a) Reduction Profiles of Cr(VI) in Binary Pollutant Mixture Over Bi_2WO_6 and Bi_2WO_6/SnS_2-10; (b) Absorption Spectra of Cr(VI) Over Bi_2WO_6/SnS_2-10 Binary Composite With the Decolourization Inset; (c) Kinetic Study for the Photoreduction of Cr(VI); (d) Apparent Reaction Rate Constant, k_{app} of Bi_2WO_6 and Bi_2WO_6/SnS_2-10.

4.3 Phytotoxicity Evaluation

A cultivation study of mung bean sprouts was conducted to assess the phytotoxicity of the RhB-Cr(VI) mixed pollutant solution before and after the photocatalytic treatment over Bi_2WO_6/SnS_2-10 composite, as shown in Figure 4.19 (a-e). Figure 4.19 (a) demonstrated that after being incubated for seven consecutive days, the mung beans grew the tallest and healthiest in the presence of deionized water, followed by the treated solution, and finally the untreated solution. The radicle length of mung beans watered with deionized water (control) was measured to be 16.06 cm. Meanwhile, the untreated RhB-Cr(VI) pollutant solution had a repressive effect on the growth of mung beans, resulting in a length of 5.28 cm. Impressively, the mung beans cultivated in photocatalytically treated solution had much higher radicle growth (12.23 cm) following degradation, with only a 23.85 % reduction in radicle length when compared to the control.

Radical growth reflected the reduction of phytotoxicity. As shown in Figure 4.19 (e), the phytotoxicity of the mixed RhB-Cr(VI) pollutant solution was the highest in the order of untreated solution > treated solution > control, with the percentages of 67.10 %, 23.85 % and 0 %, respectively. Such findings suggested that the Bi_2WO_6/SnS_2-10 composite was not only very active in photodecomposing the mixed pollutant, but it was also effective at reducing the toxicity of treated water in an impressive manner, providing new insights into the safety release of RhB dyes and Cr(VI) ions during the treatment process.

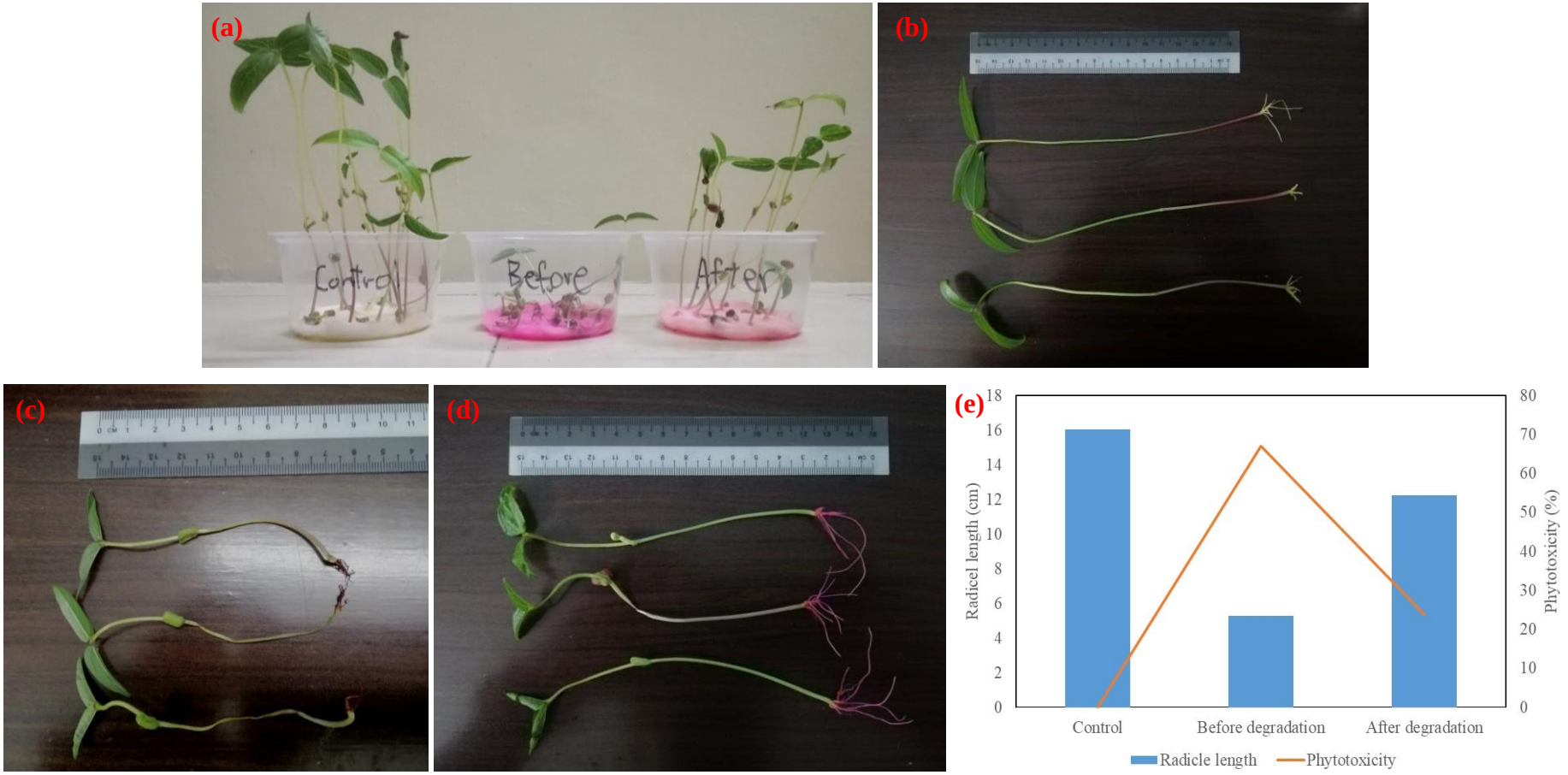

Figure 4.19: (a) Condition of Mung Beans in Each Sample After 7 days; (b-d) Radicle Length of Mung Beans in Distilled Water, Untreated Solution, and Treated Solution Respectively; (e) Phytotoxicity of RhB-Cr(VI) Mixed Pollutant Solution Before and After Degradation Using Bi_2WO_6/SnS_2-10 Composite.

4.4 Radical Scavenging Experiment

The decomposition of RhB and Cr(VI) occurred predominantly as a result of redox reactions mediated by the active species produced during the photocatalytic process. In order to ascertain the principal reactive species, scavengers such as EtOH, BQ, EDTA and Na_2SO_4 were used to quench the $\bullet OH$, $O_2\bullet^-$, h_{VB}^+ and e_{CB}^-, respectively. The photodegradation results in Figure 4.21 (a) showed that when EDTA and EtOH were added, the RhB degradation was significantly inhibited. Nevertheless, when Na_2SO_4 was added, the degradation was slightly restrained. The addition of BQ had no significant effect. These results revealed that the h_{VB}^+ and $\bullet OH$ were the main active species in the photocatalytic oxidation process, with h_{VB}^+ playing a dominant role for the RhB photodegradation over Bi_2WO_6/SnS_2-10 composite. According to Mao, et al. (2020), photosensitization resulted in the excitation of RhB to RhB* states, in which RhB* with a considerably lower redox potential reaching -1.42 eV vs NHE was much easier to be oxidised. As the CB of Bi_2WO_6/SnS_2-10 was more positive than the redox potential of RhB^*/RhB^+, electrons from RhB^* were transferred to the CB of composite, converting RhB molecules to RhB^+ and encouraging further oxidation of RhB by h_{VB}^+.

On the other hand, for the photodecomposition of Cr(VI) as illustrated in Figure 4.21 (b), the introduction of EtOH, BQ and EDTA made no significant effect. $\bullet OH$, as an oxidative radical, did not involve in the photoreduction process. Besides, it was clear that $O_2\bullet^-$ was produced by the reaction between the photo-excitated e_{CB}^- and dissolved O_2 molecules. Majority of the e_{CB}^- took part in the reduction of Cr(VI) before coming into contact with O_2. On the contrary, the Cr(VI) reduction efficiency showed remarkable deterioration with the addition of Na_2SO_4, indicating that the e_{CB}^- served as an essential active species in facilitating the photoreduction reaction.

According to the Mott-Schottky results in Section 4.1.6, the photocatalytic mechanism was proven to be Z-scheme heterojunction. The photocatalytic mechanism was as follows: both photocatalysts were photoexcited during the formation of the Z-scheme composite, resulting in the production of e_{CB}^--h_{VB}^+ pairs. The e_{CB}^- in the CB of Bi_2WO_6 recombined with the h_{VB}^+ in the VB of SnS_2. This charge carrier migration overcame the e_{CB}^--h_{VB}^+ recombination and provided

significant redox ability in the isolated systems. The greater reduction capability of e_{CB}^- in the CB of SnS_2 can photoreduce Cr(VI) to Cr(III), and a certain can interact with O_2 and H^+ to generate H_2O_2. It should also be noted that the CB of SnS_2 (0.085 eV) was more positive than that of E^o $(O_2/O_2\bullet^-)$ = -0.33 eV vs NHE, implying that the generation of $O_2\bullet^-$ was thermodynamically forbidden, which was well in accordance with its negligible effect on RhB photodegradation (Miao, et al., 2021; Sin, et al., 2022). Meanwhile, the accumulated h_{VB}^+ in the VB of Bi_2WO_6 oxidised OH^- and H_2O to form $\bullet OH$ due to the VB of Bi_2WO_6 (3.26 eV) was more positive than the standard oxidation potentials of E^o $(OH^-/\bullet OH)$ = 2.38 eV vs NHE and E^o $(H_2O/\bullet OH)$ = 2.72 eV vs NHE (Sin, et al., 2022; Cui, et al., 2021). In addition, it can directly engage in the photocatalytic removal of RhB, which has been shown the efficiency of h_{VB}^+ and $\bullet OH$ in RhB photodegradation. As a result, increasing the yield of h_{VB}^+, $\bullet OH$ and e_{CB}^- amounts in the photocatalytic reaction of Z-scheme Bi_2WO_6/SnS_2 heterojunction further boosted the synchronous decomposition of RhB and Cr(VI).

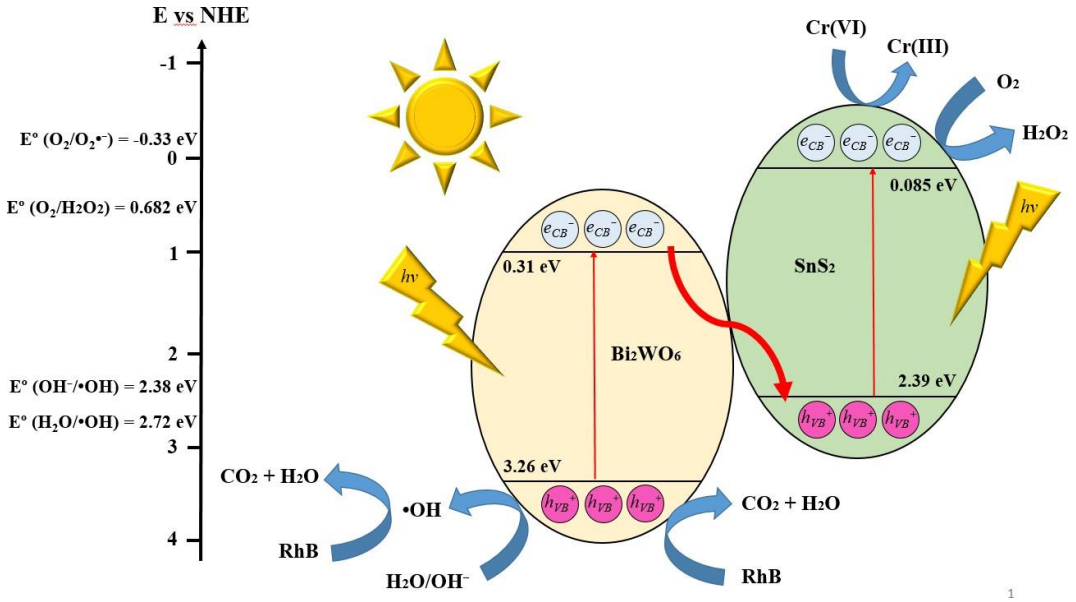

Figure 4.20: Schematic Illustration of Charge Separation Paths and Photocatalytic Mechanism of Z-Scheme Bi_2WO_6/SnS_2 Heterostructure Under Sunlight Irradiation.

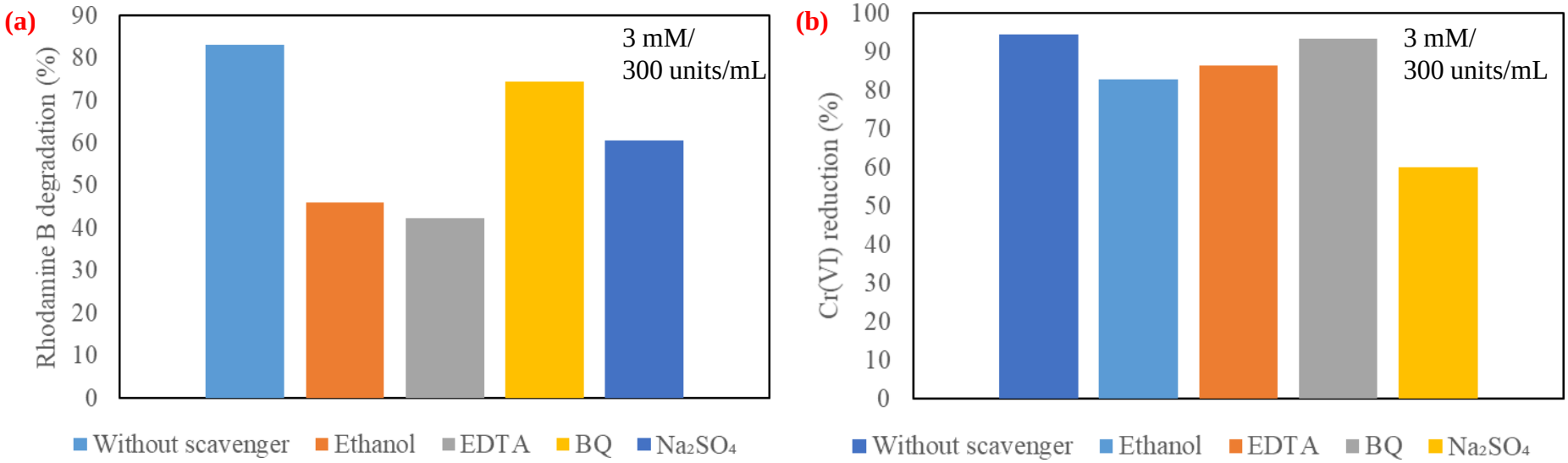

Figure 4.21: Radical Scavenging Experiments Over Bi_2WO_6/SnS_2-10 Composite for (a) Rhodamine B Degradation and (b) Cr(VI) Reduction in the Binary Pollutant Mixture.

CHAPTER 5

CONCLUSION AND RECOMMENDATIONS

5.1 Conclusion

In summary, a Z-scheme Bi_2WO_6/SnS_2 binary photocatalyst was successfully developed via a hydrothermal-deposition method for the simultaneous degradation of Rhodamine B (RhB) and reduction of Cr(VI) under sunlight irradiation. The as-synthesized samples were examined by various characterization techniques to investigate their physical, chemical, optical and electronic properties. The XRD revealed the coexistence of diffraction peaks of both Bi_2WO_6 and SnS_2 in all of the Bi_2WO_6/SnS_2 composites with high purity and crystallinity. Furthermore, ATR-FTIR validated the presence of the distinctive peaks of both Bi_2WO_6 and SnS_2 with their respective chemical bonds in the fabricated composite. In addition, UV-vis DRS results indicated that incorporating SnS_2 into Bi_2WO_6 narrowed the band gap and increased the visible light absorption as compared to pristine Bi_2WO_6. On the other hand, TPR and EIS studies validated that constructing Bi_2WO_6/SnS_2 heterojunction accelerated the charge carrier separation and migration, which can enhance the photocatalytic performance. Overall, Bi_2WO_6/SnS_2-10 composite outperformed other as-prepared photocatalysts, in which it successfully removed 95.5 % of RhB dye and 100 % of Cr(VI) in their respective single systems after 180 minutes of sunlight irradiation, with k_{app} values of 0.0178 min^{-1} and 0.0513 min^{-1}, respectively.

Interestingly, 83.19 % of RhB dye (k_{app} = 0.0082 min^{-1}) and 94.60 % of Cr(VI) (k_{app} = 0.0159 min^{-1}) were able to be removed simultaneously in a mixed pollutant system. Phytotoxicity studies demonstrated a reduction in the phytotoxicity to 23.85 % for the treated RhB-Cr(VI) mixed solution as compared to the untreated raw solution. Lastly, by integrating the results of M-S analysis and radical scavenging test, the photocatalytic mechanism of Bi_2WO_6/SnS_2 was determined to be Z-scheme heterojunction, with h_{VB}^+, $\bullet OH$ and e_{CB}^- serving as the primary active species in the synchronous decomposition of RhB and Cr(VI).

5.2 Recommendation

Several areas were not covered in this study, and further research is required for improved overall performance during application. Some recommendations for future photocatalytic studies are provided below.

a) The effect of other parameters that will affect the photocatalytic activity, such as photocatalyst loading, pH, light intensity and irradiation period, should be explored to gain a thorough understanding on the photocatalytic ability of Bi_2WO_6/SnS_2.
b) In order to increase persuasiveness, EDX or XPS should be conducted because they determine the elemental composition of the samples. XPS is more dependable since it permits the usage of binding energy.
c) An evaluation of the stability and efficiency of the used Bi_2WO_6/SnS_2 composite should be conducted through a reusability test.
d) To promote its practical applicability, Bi_2WO_6/SnS_2 should be used for the photodegradation of palm oil mill effluent (POME), which is a typical industrial effluent.
e) UV/VIS/NIR instruments, rather than UV/VIS spectrophotometry, should be employed as they are more commonly used to examine the solid samples for their optical properties.
f) High Performance Liquid Chromatography (HPLC) and Gas Chromatography (GC) are recommended for use in the studies of photodegradation of RhB dye and photoreduction of Cr(VI).

REFERENCES

Abuhasel, K., Kchaou, M., Alquraish, M., Munusamy, Y. and Jeng, Y., 2021. Oily Wastewater Treatment: Overview of Conventional and Modern Methods, Challenges, and Future Opportunities. *Water*, 13(7), p. 980.

Afroz, R. and Rahman, A., 2022. Health impact of river water pollution in Malaysia. *International Journal of ADVANCED AND APPLIED SCIENCES*, 4(5), pp. 78-85.

Ahmed, S. and Haider, W., 2018. Heterogeneous photocatalysis and its potential applications in water and wastewater treatment: a review. *Nanotechnology*, 29(34), p. 342001.

Al-Hamdani, A., 2017. Third Order Nonlinear Properties of Rhodamine B Dye Doped PVA Polymer Determined by Eclipsing Scan Technique. *International Journal of Nanoelectronics and Materials*, 11(2), pp. 135-142.

Al-Kadhemy, M., Alsharuee, I. and Al-Zuky, A., 2011. Analysis of the Effect of the Concentration of Rhodamine B in Ethanol on the Fluorescence Spectrum Using the “Gauss Mod” Function. *Journal of Physical Science*, 22(2), pp. 77-86.

Arya, M., Kaur, M., Kaur, A., Singh, S., Devi, P. and Kansal, S., 2020. Hydrothermal synthesis of rGO-Bi_2WO_6 heterostructure for the photocatalytic degradation of levofloxacin. *Optical Materials*, 107, p. 110126.

Asian Development Bank, 2020. *Asian Water Development Outlook 2020: Advancing Water Security across Asia and the Pacific*. [online] Available at: <https://www.adb.org/sites/default/files/publication/663931/awdo-2020.pdf> [Accessed 18 July 2022].

Badawi, A., Abd Elkodous, M. and Ali, G., 2021. Recent advances in dye and metal ion removal using efficient adsorbents and novel nano-based materials: an overview. *RSC Advances*, 11(58), pp. 36528-36553.

Baruah, A., Chaudhary, V., Malik, R. and Tomer, V., 2019. Nanotechnology Based Solutions for Wastewater Treatment. *Nanotechnology in Water and Wastewater Treatment*, pp. 337-368.

Bi, H., Liu, J., Wu, Z., Zhu, K., Suo, H., Lv, X., Fu, Y., Jian, R. and Sun, Z., 2021. Construction of $Bi_2WO_6/ZnIn_2S_4$ with Z-scheme structure for efficient photocatalytic performance. *Chemical Physics Letters*, 769, p. 138449.

Burton, L., Whittles, T., Hesp, D., Linhart, W., Skelton, J., Hou, B., Webster, R., O'Dowd, G., Reece, C., Cherns, D., Fermin, D., Veal, T., Dhanak, V. and Walsh, A., 2016. Electronic and optical properties of single crystal SnS_2: an earth-abundant disulfide photocatalyst. *Journal of Materials Chemistry A*, 4(4), pp. 1312-1318.

Chachvalvutikul, A., Luangwanta, T. and Kaowphong, S., 2021. Double Z-scheme $FeVO_4/Bi_4O_5Br_2/BiOBr$ ternary heterojunction photocatalyst for simultaneous photocatalytic removal of hexavalent chromium and rhodamine B. *Journal of Colloid and Interface Science*, 603, pp. 738–757.

Chen, F., Guo, J., Meng, D., Wu, Y., Sun, R. and Zhao, C., 2021. Strong Pyro-Electro-Chemical Coupling of Elbaite/H_2O_2 System for Pyrocatalysis Dye Wastewater. *Catalysts*, 11(11), p. 1370.

Chin, Y., Sin, J., Lam, S. and Mohamed, A., 2018. Preparation of Nb_2O_5-decorated hierarchical porous ZnO microspheres with enhanced photocatalytic degradation of palm oil mill effluent. *Journal of Materials Science: Materials in Electronics*, 30(2), pp. 1739-1750.

Chromium Toxicity, 2008. Agency for Toxic Substances and Disease Registry, pp. 29-37.

Coker, V., Garrity, A., Wennekes, W., Roesink, H., Cutting, R. and Lloyd, J., 2013. Cr(VI) and azo dye removal using a hollow-fibre membrane system functionalized with a biogenic Pd-magnetite catalyst. *Environmental Technology*, 35(8), pp. 1046-1054.

Cui, Z., Yang, H., Wang, B., Li, R. and Wang, X., 2016. Effect of Experimental Parameters on the Hydrothermal Synthesis of Bi_2WO_6 Nanostructures. *Nanoscale Research Letters*, 11(1).

Cui, C., Guo, R., Ren, E., Xiao, H., Lai, X., Qin, Q., Jiang, S., Shen, H., Zhou, M. and Qin, W., 2021. Facile hydrothermal synthesis of rod-like Nb_2O_5/Nb_2CT_x composites for visible-light driven photocatalytic degradation of organic pollutants. *Environmental Research*, 193, p. 110587.

Das, K., Majhi, D., Bariki, R. and Mishra, B., 2020. $SnS_2/Bi_4Ti_3O_{12}$ Heterostructure Material: A UV-Visible Light Active Direct Z-Scheme Photocatalyst for Aqueous Phase Degradation of Diazinon. *ChemistrySelect*, 5(4), pp. 1567-1577.

Deng, Y. and Zhao, R., 2015. Advanced Oxidation Processes (AOPs) in Wastewater Treatment. *Current Pollution Reports*, 1(3), pp. 167-176.

Department of Environment, 2009. *Environmental quality industrial effluents regulations 2009*. [online] Available at: <https://www.doe.gov.my/portalv1/wpcontent/uploads/2015/01/Environmental_Quality_Industrial_Effluent_Regulations_2009_-_P.U.A_434-2009.pdf> [Accessed 29 July 2022].

Du, H., Zhang, Y., Jiang, H. and Wang, H., 2022. Adsorption of rhodamine B on polyvinyl chloride, polystyrene, and polyethylene terephthalate microplastics in aqueous environments. *Environmental Technology & Innovation*, 27, p. 102495.

El Azzouzi, L., Qisse, N., Ennouhi, M., Bouziani, A., Ellouzi, I., Mountacer, H., Zrineh, A. and El Hajjaji, S., 2020. Photocatalytic degradation of Doxycycline in aqueous solution using Fe_2O_3 and Fe_2O_3-Bi_2WO_6 catalysts. *Mediterranean Journal of Chemistry*, 10(3), pp. 233–238.

Gan, L., Geng, A., Song, C., Xu, L., Wang, L., Fang, X., Han, S., Cui, J. and Mei, C., 2020. Simultaneous removal of rhodamine B and Cr(VI) from water using cellulose carbon nanofiber incorporated with bismuth oxybromide: The effect of cellulose pyrolysis temperature on photocatalytic performance. *Environmental Research*, 185, p. 109414.

Gao, X., Li, W., Fu, F., Wu, Y., Li, D. and Wang J., 2011. Preparation of Bi_2WO_6 Photocatalyst and Its Application in the Photocatalytic Oxidative Desulfurization. *China Petroleum Processing and Petrochemical Technology*, 13(2), pp. 19-23.

Gao, X., Huang, G., Gao, H., Pan, C., Wang, H., Yan, J., Liu, Y., Qiu, H., Ma, N. and Gao, J., 2016. Facile fabrication of Bi_2S_3/SnS_2 heterojunction photocatalysts with efficient photocatalytic activity under visible light. *Journal of Alloys and Compounds*, 674, pp. 98-108.

Garrido-Cardenas, J. A., Esteban-García, B., Agüera, A., Sánchez-Pérez, J. A. and Manzano-Agugliaro, F., 2019. Wastewater Treatment by Advanced Oxidation Process and Their Worldwide Research Trends. *International journal of environmental research and public health*, 17(1), p. 170.

Gholami, P., Dinpazhoh, L., Khataee, A. and Orooji, Y., 2019. Sonocatalytic activity of biochar-supported ZnO nanorods in degradation of gemifloxacin: Synergy study, effect of parameters and phytotoxicity evaluation. *Ultrasonics Sonochemistry*, 55, pp. 44-56.

Gordillo-Delgado, F., Zuluaga-Acosta, J. and Restrepo-Guerrero, G., 2020. Effect of the suspension of Ag-incorporated TiO_2 nanoparticles (Ag-TiO_2 NPs) on certain growth, physiology and phytotoxicity parameters in spinach seedlings. *PLOS ONE*, 15(12), p. e0244511.

Guo, Y., Zhang, G. and Gan, H., 2012. Synthesis, characterization and visible light photocatalytic properties of Bi_2WO_6/rectorite composites. *Journal of Colloid and Interface Science*, 369(1), pp. 323-329.

Guo, L., Huang, H., Mei, L., Li, M. and Zhang, Y., 2021. Bismuth-based Z-scheme photocatalytic systems for solar energy conversion. *Materials Chemistry Frontiers*, 5(6), pp. 2484-2505.

Helmenstine, A., 2019. *Get the Facts About the Element Chromium*. [online] ThoughtCo. Available at: <https://www.thoughtco.com/chromium-element-facts-606519> [Accessed 29 July 2022].

Honeychurch, K., 2022. Voltammetric Behaviour of Rhodamine B at a Screen-Printed Carbon Electrode and Its Trace Determination in Environmental Water Samples. *Sensors*, 22(12), p. 4631.

Hu, W. and Liu, W., 2021. $CuAlO_2/Bi_2WO_6$: A novel p–n type composite with significantly enhanced visible-light photocatalytic reduction of Cr(VI). *Materials Research Express*, 8(6), p. 065901.

Huang, C., Chen, L., Li, H., Mu, Y. and Yang, Z., 2019. Synthesis and application of Bi_2WO_6 for the photocatalytic degradation of two typical fluoroquinolones under visible light irradiation. *RSC Advances*, 9(48), pp. 27768-27779.

Islam, J.B., Furukawa, M., Tateishi, I., Katsumata, H. and Kaneco, S., 2019. Photocatalytic reduction of hexavalent chromium with nanosized TiO_2 in presence of formic acid. *ChemEngineering*, 3(2), p. 33.

Islam, R., 2020. *Water pollution due to textile industry*. [online] Textile News, Apparel News, RMG News, Fashion Trends. Available at: <https://www.textiletoday.com.bd/water-pollution-due-textile-industry/> [Accessed 16 July 2022].

Jain, R., Mathur, M., Sikarwar, S. and Mittal, A., 2007. Removal of the hazardous dye rhodamine B through photocatalytic and adsorption treatments. *Journal of Environmental Management*, 85(4), pp. 956-964.

Jakimińska, A., Pawlicki, M. and Macyk, W., 2022. Photocatalytic transformation of Rhodamine B to Rhodamine-110 – The mechanism revisited. *Journal of Photochemistry and Photobiology A: Chemistry*, 433, p. 114176.

Kee, W., Wong, Y., Ong, S., Lutpi, N., Sam, S., Chai, A. and Eng, K., 2021. Photocatalytic Degradation of Sugarcane Vinasse Using ZnO Photocatalyst: Operating Parameters, Kinetic Studies, Phytotoxicity Assessments, and Reusability. *International Journal of Environmental Research*, 16(1).

Khanam, S. and Rout, S. K., 2022. Enhanced photocatalytic oxidation of RhB and MB using plasmonic performance of AG deposited on Bi_2WO_6. *Chemistry*, 4(2), pp. 272–296.

Kumar, G. and Kumar Dutta, R., 2022. Fabrication of plate-on-plate SnS_2/Bi_2WO_6 nanocomposite as photocatalyst for sunlight mediated degradation of antibiotics in aqueous medium. *Journal of Physics and Chemical of Solids*, 164, p. 110639.

Kumar, G., Kumar, J., Bag, M. and Kumar Dutta, R., 2022. Solar light induced photocatalytic process for reduction of hexavalent chromium and degradation of tetracycline and methylene blue by heterostructures made of SnS_2 nanoplates surface modified by $ZnWO_4$ nanorods. *Separation and Purification Technology*, 292, p. 121040.

Lam, S., Sin, J., Abdullah, A. and Mohamed, A., 2012. Degradation of wastewaters containing organic dyes photocatalysed by zinc oxide: a review. *Desalination and Water Treatment*, 41(1-3), pp. 131-169.

Li, Y., Liu, J. and Huang, X., 2008. Synthesis and Visible-Light Photocatalytic Property of Bi_2WO_6 Hierarchical Octahedron-Like Structures. *Nanoscale Research Letters*, 3(10), pp. 365-371.

Li, H., Cui, Y. and Hong, W., 2013. High photocatalytic performance of $BiOI/Bi_2WO_6$ toward toluene and Reactive Brilliant Red. *Applied Surface Science*, 264, pp. 581–588.

Li, J., Shi, Q., Chen, Y. and Song, M., 2017. Hydrothermal synthesis of Bi_2WO_6 and photocatalytic reduction of aqueous Cr(VI) under visible light irradiation. *IOP Conference Series: Earth and Environmental Science*, 100, p. 012030.

Li, Z., Meng, X. and Zhang, Z., 2019. Hexagonal SnS nanoplates assembled onto hierarchical Bi_2WO_6 with enhanced photocatalytic activity in detoxification and disinfection. *Journal of Colloid and Interface Science*, 537, pp. 345-357.

Li, R., Li, T. and Zhou, Q., 2020. Impact of titanium dioxide (TiO_2) modification on its application to pollution treatment—a review. *Catalysts*, 10(7), p. 804.

Lu, X., Che, W., Hu, X., Wang, Y., Zhang, A., Deng, F., Luo, S. and Dionysiou, D., 2018. The facile fabrication of novel visible-light-driven Z-scheme $CuInS_2/Bi_2WO_6$ heterojunction with intimate interface contact by in situ hydrothermal growth strategy for extraordinary photocatalytic performance. *Chemical Engineering Journal*, 356, pp. 819-829.

Malay Mail, 2020. *Govt targets to reduce Malaysians' daily water consumption by 2025*. [online] Available at: <https://www.malaymail.com/news/malaysia/2020/08/03/govt-targets-to-reduce-malaysians-daily-water-consumption-by-2025/1890715> [Accessed 16 July 2022].

Mao, W., Zhang, L., Wang, T., Bai, Y. and Guan, Y., 2020. Fabrication of highly efficient Bi_2WO_6/CuS composite for visible-light photocatalytic removal of organic pollutants and Cr(VI) from wastewater. *Frontiers of Environmental Science & Engineering*, 15(4).

Mendes, P., Ribeiro, J., Martins, G., Lucia, T., Araujo, T., Fuentes-Guevara, M., Corrêa, L. and Corrêa, É., 2021. Phytotoxicity test in check: Proposition of methodology for comparison of different method adaptations usually used worldwide. *Journal of Environmental Management*, 291, p. 112698.

Miao, F., Wang, Q., Zhang, L. and Shen, B., 2021. Magnetically separable Z-scheme FeSiB metallic glass/g-C_3N_4 heterojunction photocatalyst with high degradation efficiency at universal pH conditions. *Applied Surface Science*, 540, p. 148401.

MIDA, 2019. *2019 MALAYSIA Investment Performance Report.* [online] Mida.gov.my. Available at: <https://www.mida.gov.my/wp-content/uploads/2020/12/20200421151258_MIDA20IPR20201920fullbook_FINAL.pdf> [Accessed 29 July 2022].

Moreau, D., Lefort, C., Burke, R., Leveque, P. and O'Connor, R., 2015. Rhodamine B as an optical thermometer in cells focally exposed to infrared laser light or nanosecond pulsed electric fields. *Biomedical Optics Express*, 6(10), p. 4105.

Nunes, D., Pimentel, A., Branquinho, R., Fortunato, E. and Martins, R., 2021. Metal Oxide-Based Photocatalytic Paper: A Green Alternative for Environmental Remediation. *Catalysts*, 11(4), p. 504.

Orimolade, B., Idris, A., Feleni, U. and Mamba, B., 2021. Recent advances in degradation of pharmaceuticals using Bi_2WO_6 mediated photocatalysis – A comprehensive review. *Environmental Pollution*, 289, p. 117891.

Pang, Y. and Abdullah, A., 2013. Current Status of Textile Industry Wastewater Management and Research Progress in Malaysia: A Review. *CLEAN - Soil, Air, Wate*r, 41(8), pp. 751-764.

Pérez-Portuondo, I., Serrat-Díaz, M., Pérez-Silva, R. and Ábalos-Rodríguez, A., 2021. Phytotoxic Effects of 4-Chlorophenol and 2,4-Dichlorophenol in the Germination of Seeds of *Phaseolus vulgaris* and *Zea mayz*. *American Journal of Plant Sciences*, 12(4), pp. 614-623.

Phuruangrat, A., Jonjana, S., Thongtem, S. and Thongtem, T., 2018. Precipitation–deposition synthesis, characterization, and visible light-driven photocatalytic properties of heterostructure AgI/Bi_2WO_6 nanocomposites. *Journal of the Australian Ceramic Society*, 55(1), pp. 57-63.

Qian, R., Zong, H., Schneider, J., Zhou, G., Zhao, T., Li, Y., Yang, J., Bahnemann, D. and Pan, J., 2018. Charge Carrier Trapping, Recombination and Transfer during TiO_2 Photocatalysis: An Overview. *Catalysis Today*.

Qiu, F., Li, W., Wang, F., Li, H., Liu, X. and Sun, J., 2017. In-situ synthesis of novel Z-scheme SnS_2/BiOBr photocatalysts with superior photocatalytic efficiency under visible light. *Journal of Colloid and Interface Science*, 493, pp. 1-9.

Raziq Rahimi Kooh, Khairud Dahri and Lim, L., 2016. The removal of Rhodamine B dye from aqueous solution using Casuarina equisetifolia needles as adsorbent. *Coagent Environmental Science*, 2(1).

Rohmawati, H., Fitriasnani, M., Purnani, W. and Dewi, R., 2021. Effect of Rhodamine B Against The Number of Primary Follicles in White Rats (Rattus norvegicus). *Journal of Physics: Conference Series*, 1899(1), p. 012070.

Rouibah, I., Hakimi, S., Khellaf, N., Mansour, H. and Assadi, A., 2021. Photoactivity Performance of TiO_2/cellulose and ZnO/polystyrene; Intensified Effect of Oxidants on Degradation Efficiency of Acetaminophen. *Phys. Chem. Res.*, 9(3), pp. 413-426.

Saeed, M., Adeel, S., Shahzad, M., Muneer, M. and Younas, M., 2015. Pt/Al_2O_3 Catalyzed Decolorization of Rhodamine B Dye in Aqueous Medium. *Chiang Mai J. Sci.*, 42(3), pp. 730-744.

Schneider, J., Firak, D., Ribeiro, R. and Peralta-Zamora, P., 2020. Use of scavenger agents in heterogeneous photocatalysis: Truths, half-truths, and misinterpretations. *Physical Chemistry Chemical Physics*, 22(27), pp. 15723–15733.

Shahbudin, N. and Kamal, N., 2021. Establishment of material flow analysis (MFA) for heavy metals in a wastewater system. *Ain Shams Engineering Journal*, 12(2), pp. 1407-1418.

Shen, K. and Gondal, M., 2017. Removal of hazardous Rhodamine dye from water by adsorption onto exhausted coffee ground. *Journal of Saudi Chemical Society*, 21, pp. 120-127.

Shim, J., Shea, P., Lim, J. and Oh, B., 2015. Simultaneous Cr(VI) reduction and methylene blue removal by Bacillussp. JH2-2 isolated from mining site soil. *Desalination and Water Treatment*, 57(15), pp. 7021-7028.

Sin, J., Lam, S., Zeng, H., Lin, H., Li, H., Tham, K., Mohamed, A., Lim, J. and Qin, Z., 2021. Magnetic $NiFe_2O_4$ nanoparticles decorated on N-doped BiOBr nanosheets for expeditious visible light photocatalytic phenol degradation and hexavalent chromium reduction via a Z-scheme heterojunction mechanism. *Applied Surface Science*, 559, p. 149966.

Sin, J., Lam, S., Zeng, H., Lin, H., Li, H., Huang, L., Tham, K., Mohamed, A. and Lim, J., 2022. Enhanced synchronous photocatalytic 4-chlorophenol degradation and Cr(VI) reduction by novel magnetic separable visible-light-driven Z-scheme $CoFe_2O_4$/P-doped BiOBr heterojunction nanocomposites. *Environmental Research*, 212, p. 113394.

Srivastava, R., Vishwakarma, P. K., Yadav, U., Rai, S., Umrao, S., Giri, R., Saxena, P. and Srivastava, A., 2021. 2d SnS_2 nanostructure-derived photocatalytic degradation of organic pollutants under visible light. *Frontiers in Nanotechnology*, 3, p. 711368.

Stambulska, U., Bayliak, M. and Lushchak, V., 2018. Chromium(VI) Toxicity in Legume Plants: Modulation Effects of Rhizobial Symbiosis. *BioMed Research International*, 2018, pp. 1-13.

Stephens, G., Slingo, J., Rignot, E., Reager, J., Hakuba, M., Durack, P., Worden, J. and Rocca, R., 2020. Earth's water reservoirs in a changing climate. *Proceedings of the Royal Society A: Mathematical, Physical and Engineering Sciences*, 476(2236), p. 20190458.

Sundarajoo, A. and Maniyam, M., 2019. Enhanced Decolourization of Congo Red Dye by Malaysian Rhodococcus UCC 0010 Immobilized in Calcium Alginate. *Journal of Advanced Research Design*, 62(1), pp. 1-9.

Susanti, Y., Afifah, N. and Saleh, R., 2017. Multifunctional photocatalytic degradation of methylene blue using $LaMnO_3/Fe_3O_4$ nanocomposite on different types of graphene. *Journal of Physics: Conference Series*, 820, p. 012021.

Swaroop, A., Bagchi, M., Preuss, H., Zafra-Stone, S., Ahmad, T. and Bagchi, D., 2019. Benefits of chromium(III) complexes in animal and human health. *The Nutritional Biochemistry of Chromium (III)*, pp. 251-278.

Tan, H., Abdi, F. and Ng, Y., 2019. Heterogeneous photocatalysts: an overview of classic and modern approaches for optical, electronic, and charge dynamics evaluation. *Chemical Society Reviews*, 48(5), pp. 1255-1271.

Tchounwou, P., Yedjou, C., Patlolla, A. and Sutton, D., 2012. Heavy Metals Toxicity and the Environment. *Experientia supplementum*, 101, pp. 133-164.

Thongam, D. and Chaturvedi, H., 2021. Advances in nanomaterials for heterogeneous photocatalysis. *Nano Express*, 2(1), p. 012005.

Verma, Y., 2008. Acute toxicity assessment of textile dyes and textile and dye industrial effluents using Daphnia magna bioassay. *Toxicology and Industrial Health*, 24(7), pp. 491-500.

Wang, Q., Chen, X., Yu, K., Zhang, Y. and Cong, Y., 2013. Synergistic photosensitized removal of Cr(VI) and Rhodamine B dye on amorphous TiO_2 under visible light irradiation. *Journal of Hazardous Materials*, 246-247, pp. 135–144.

Wang, M., Nie, X., Tian, L., Hu, J., Yin, D., Qiao, H., Li, T. and Li, Y., 2018. Rhodamine B in spices determined by a sensitive UPLC-MS/MS method. *Food Additives & Contaminants: Part B*, 12(1), pp. 59-64.

Wei, X., Wang, P., Fu, H., Zhao, C. and Wang, C., 2020. Boosted photocatalytic elimination toward Cr(VI) and organic pollutants over BUC-21/$Cd_{0.5}Zn_{0.5}S$ under LED visible Light. *Materials Research Bulletin*, 129, p. 110903.

Wierzbicka, E., Kuśmierek, K., Świątkowski, A. and Legocka, I., 2022. Efficient Rhodamine B Dye Removal from Water by Acid- and Organo-Modified Halloysites. *Minerals*, 12(3), p. 350.

Xu, F., Xu, C., Chen, H., Wu, D., Gao, Z., Ma, X., Zhang, Q. and Jiang, K., 2019. The synthesis of Bi_2S_3/2D-Bi_2WO_6 composite materials with enhanced photocatalytic activities. *Journal of Alloys and Compounds*, 780, pp. 634-642.

Xu, Y., Yu, J., Long, J., Tu, L., Dai, W. and Yang, L., 2022. Z-Scheme Heterojunction of SnS_2/Bi_2WO_6 for Photoreduction of CO_2 to 100% Alcohol Products by Promoting the Separation of Photogenerated Charges. *Nanomaterials*, 12(12), p. 2030.

Yang, W., Chen, Y., Gao, S., Sang, L., Tao, R., Sun, C., Shang, J. and Li, Q., 2021. Post-illumination activity of Bi_2WO_6 in the dark from the photocatalytic "memory" effect. *Journal of Advanced Ceramics*, 10(2), pp. 355-367.

Ye, L., Deng, Y., Wang, L., Xie, H. and Su, F., 2019. Bismuth-Based Photocatalysts for Solar Photocatalytic Carbon Dioxide Conversion. *ChemSusChem*, 12(16), pp. 3671-3701.

Yu, F., Jin, M., Zhang, Y., Lei, C., Zhou, L., Zhu, H. and Yu, B., 2022. Visible-light-driven Zr-MOF/BiOBr heterojunction for the efficient synchronous removal of hexavalent chromium and rhodamine B from wastewater. *ACS Omega*, 7(29), pp. 25066–25077.

Yunus, K., Zuraidah, M. and John, A., 2020. A review on the accumulation of heavy metals in coastal sediment of Peninsular Malaysia. *Ecofeminism and Climate Change*, 1(1), pp. 21-35.

Zhang, L., Tian, W., Chen, Y., Chen, J., Teng, H., Zhou, J., Shi, J. and Sun, Y., 2016. Light-driven removal of rhodamine B over $SrTiO_3$ modified Bi_2WO_6 composites. *RSC Advances*, 6(86), pp. 83471–83481.

Zhang, X., 2017. Synthesis and photocatalytic activity of Bi_2WO_6 microspheres with hierarchical structure. *Ferroelectrics*, 514(1), pp. 34-42.

Zhang, Q., Jiang, Z., Wang, M. and Ge, X., 2018. Gamma ray radiation effect on Bi_2WO_6 photocatalyst. *Chinese Journal of Chemical Physics*, 31(5), pp. 701-706.

Zhang, F., Wang, X., Liu, H., Liu, C., Wan, Y., Long, Y. and Cai, Z., 2019. Recent Advances and Applications of Semiconductor Photocatalytic Technology. *Applied Sciences*, 9(12), p. 2489.

Zhang, Q., Wang, M., Ao, M., Luo, Y., Zhang, A., Zhao, L., Yan, L., Deng, F. and Luo, X., 2019. Solvothermal synthesis of Z-scheme $AgIn_5S_8/Bi_2WO_6$ nano-heterojunction with excellent performance for photocatalytic degradation and Cr(VI) reduction. *Journal of Alloys and Compounds*, 805, pp. 41-49.

Zhang, R., Zeng, K. and Zhang, T., 2020. Enhanced visible-light-driven photocatalytic activity of Bi_2WO_6-BiSI Z-scheme heterojunction photocatalysts for tetracycline degradation. *International Journal of Environmental Analytical Chemistry*, pp. 1-16.

Zhang, Y., Ju, P., Hao, L., Zhai, X., Jiang, F. and Sun, C., 2021. Novel Z-scheme MoS_2/Bi_2WO_6 heterojunction with highly enhanced photocatalytic activity under visible light irradiation. *Journal of Alloys and Compounds*, 854, p. 157224.

Zhao, G., Liu, S., Lu, Q., Xu, F., Sun, H. and Yu, J., 2013. Synthesis of TiO_2/Bi_2WO_6 nanofibers with electrospinning technique for photocatalytic methyl blue degradation. *Journal of Sol-Gel Science and Technology*, 66(3), pp. 406-412.

Zhu, J., Zhou, Y., Wu, W., Deng, Y. and Xiang, Y., 2019. A Novel Rose-Like CuS/Bi_2WO_6 Composite for Rhodamine B Degradation. *ChemistrySelect*, 4(40), pp. 11853–11861.